



Space engineering

Thermal design handbook - Part 8: Heat Pipes

ECSS Secretariat
ESA-ESTEC
Requirements & Standards Division
Noordwijk, The Netherlands

Foreword

This Handbook is one document of the series of ECSS Documents intended to be used as supporting material for ECSS Standards in space projects and applications. ECSS is a cooperative effort of the European Space Agency, national space agencies and European industry associations for the purpose of developing and maintaining common standards.

The material in this Handbook is a collection of data gathered from many projects and technical journals which provides the reader with description and recommendation on subjects to be considered when performing the work of Thermal design.

The material for the subjects has been collated from research spanning many years; therefore a subject may have been revisited or updated by science and industry.

The material is provided as good background on the subjects of thermal design, the reader is recommended to research whether a subject has been updated further, since the publication of the material contained herein.

This handbook has been prepared by ESA TEC-MT/QR division, reviewed by the ECSS Executive Secretariat and approved by the ECSS Technical Authority.

Disclaimer

ECSS does not provide any warranty whatsoever, whether expressed, implied, or statutory, including, but not limited to, any warranty of merchantability or fitness for a particular purpose or any warranty that the contents of the item are error-free. In no respect shall ECSS incur any liability for any damages, including, but not limited to, direct, indirect, special, or consequential damages arising out of, resulting from, or in any way connected to the use of this document, whether or not based upon warranty, business agreement, tort, or otherwise; whether or not injury was sustained by persons or property or otherwise; and whether or not loss was sustained from, or arose out of, the results of, the item, or any services that may be provided by ECSS.

Published by: ESA Requirements and Standards Division
ESTEC, P.O. Box 299,
2200 AG Noordwijk
The Netherlands

Copyright: 2011 © by the European Space Agency for the members of ECSS

Table of contents

1 Scope.....	11
2 References	12
3 Terms, definitions and symbols.....	13
3.1 Terms and definitions	13
3.2 Symbols.....	13
4 General introduction	17
5 Heat pipe wicks.....	19
5.1 General.....	19
5.2 Basic properties.....	20
5.2.1 Equilibrium capillary height.....	20
5.2.2 Permeability.....	20
5.2.3 Effective thermal conductivity of the wick	20
5.3 Low resistance wicks.....	22
6 Heat pipe working fluids	28
6.1 General.....	28
6.2 Empirical correlations	29
6.3 Physical properties	31
6.4 Compatibility with wicks.....	47
7 Simple heat pipe	48
7.1 General.....	48
7.2 Operating limits	48
7.2.1 Capillary heat transfer limit.....	49
7.2.2 Sonic limit (choking)	54
7.2.3 Entrainment limit.....	56
7.2.4 Boiling limit	56
7.3 Performance.....	57
8 Variable conductance heat pipes.....	70

8.1	General.....	70
8.2	Design considerations	72
8.2.1	Diffusion of the working fluid.....	72
8.2.2	Working fluid selection.....	73
8.2.3	Reservoir sizing	74
9	Existing System.....	78
9.1	Eads Astrium	78
9.2	Euro Heat Pipes	91
9.2.1	Aluminium Heat Pipes	91
9.2.2	STAINLESS STEEL HEAT PIPES. This part deals with the products from Technical Data Sheet n° 1B: EHP Stainless Steel	101
9.3	Iberespacio	106
9.3.1	Axial Grooved Heat Pipes	106
9.3.2	Arterial Heat Pipes.....	109
9.4	Thales Alenia Space	111
9.4.1	Technical Description	111
9.4.2	External Geometries.....	113
10	Cryogenic heat pipes	116
10.1	General.....	116
10.2	Working fluids.....	116
10.3	Wicks	118
10.3.1	Lab wicks.....	120
10.3.2	Tunnel artery	120
10.3.3	Graded-porosity wicks	120
10.4	Operating limits	121
10.4.1	Capillary heat transfer limit.....	121
10.5	Transient operating characteristics	127
10.5.1	Mathematical modelling of static transient.....	127
10.5.2	Mathematical modelling of fluid dynamic transient	128
10.6	Reduced gravity testing of cryogenic heat pipes.....	129
10.7	Thermal diode cryogenic heat pipes	131
10.7.2	Reversal requirements	132
10.8	Superfluid heat pipes.....	134
10.9	Existing systems.....	138
Bibliography.....	146	

Figures

Figure 5-1: Measured values of the inverse permeability, K^{-1} , vs. mass flow rate per unit area, \dot{m} .> From Phillips & Hinderman (1969) [67].	27
Figure 5-2: Measured values of the inverse permeability, K^{-1} , vs. mass flow rate per unit area, \dot{m} .> From Phillips & Hinderman (1969) [67].	27
Figure 6-1: Relevant physical properties of Ammonia as a function of temperature, T , The labels correspond to experimental points. The expressions used to calculate the tabulated values are given below. Calculated by the compiler.....	32
Figure 6-2: Relevant physical properties of Ethanol as a function of temperature, T , The labels correspond to experimental points. The expressions used to calculate the tabulated values are given below. Calculated by the compiler.....	34
Figure 6-3: Relevant physical properties of Freon 11 as a function of temperature, T , The labels correspond to experimental points. The expressions used to calculate the tabulated values are given below. Calculated by the compiler.....	36
Figure 6-4: Formulae Used for Calculating the Values of the Physical Properties.....	38
Figure 6-5: Relevant physical properties of Nitrogen as a function of temperature, T , The labels correspond to experimental points. The expressions used to calculate the tabulated values are given below. Calculated by the compiler.....	40
Figure 6-6: Relevant physical properties of Propane as a function of temperature, T , The labels correspond to experimental points. The expressions used to calculate the tabulated values are given below. Calculated by the compiler.....	42
Figure 6-7: Relevant physical properties of Water as a function of temperature, T , The labels have been drawn to guide in the selection of the appropriate curve, and do not correspond to experimental values. After Schmidt (1969) [82].....	44
Figure 6-8: Figure of Merit, N , as a function of temperature, T , for several heat pipe working fluids. For each curve, the range of temperature variation is bounded between the largest and smallest operating pressures. Calculated by the compiler.	46
Figure 7-1: Sketch illustrating design variables in grooved heat pipes. From Frank et al. (1967) [27], quoted by Winter & Barsch (1971) [96].	51
Figure 7-2: Relation between the dimensionless parameter $16/\beta(\nu_w/\nu_l)F$ and the geometrical parameter, ψ . From Frank et al. (1967) [27], quoted by Winter & Barsch (1971) [96].	52
Figure 7-3: Optimum value of the dimensionless maximum heat transfer, $Q_{max}/\pi r_w^3$, vs. the geometrical parameter, ψ . From Frank et al. (1967) [27], quoted by Winter & Barsch (1971) [96].	53
Figure 7-4: Graph for determining F . From Frank et al. (1967) [27], quoted by Winter & Barsch (1971) [96].	53
Figure 7-5: Optimum value of the aspect ratio of the grooves, α , vs. the geometrical parameter, ψ . From Frank et al. (1967) [27], quoted by Winter & Barsch (1971) [96].	54
Figure 7-6: Maximum heat transfer, Q_{max} , based on sonic limit, vs. evaporator temperature, T_E , for several values of the shear stresses, τ , and of the convective heat transfer, Q_{conv} . Sodium heat pipe. A: $\tau = 0$ and $Q_{conv} = 0$; B: $\tau \neq 0$ and $Q_{conv} \neq 0$; C: $\tau \neq 0$ and $Q_{conv} = 0$; D: $\tau \neq 0$ and $Q_{conv} \neq 0$. In this case	

the heat pipe had an adiabatic length. In curves A, B, and C choking is reached at the evaporator, while in curve D choking is reached at the adiabatic length end. From Levy (1972) [49].	55
Figure 7-7: Heat Transfer, Q_{max} , and Integral Heat Transport Factor, $[Q \cdot I_{eff}]_{max}$, vs. wick thickness, δ , for several mesh sizes and two heat pipe diameters, D_o . Circumferential screen wick. Solid lines: vapour laminar flow; dotted lines: vapour turbulent flow. From Skrabek (1972) [88].	58
Figure 7-8: Heat Transfer, Q_{max} , and Integral Heat Transport Factor, $[Q \cdot I_{eff}]_{max}$, vs. wick thickness, δ , for several mesh sizes and two heat pipe diameters, D_o . Circumferential screen wick. Solid lines: vapour laminar flow; dotted lines: vapour turbulent flow. From Skrabek (1972) [88].	59
Figure 7-9: Heat Transfer, Q_{max} , and Integral Heat Transport Factor, $[Q \cdot I_{eff}]_{max}$, vs. wick thickness, δ , for several mesh sizes and two heat pipe diameters, D_o . Circumferential screen wick. Solid lines: vapour laminar flow; dotted lines: vapour turbulent flow. From Skrabek (1972) [88].	60
Figure 7-10: Heat Transfer, Q_{max} , and Integral Heat Transport Factor, $[Q \cdot I_{eff}]_{max}$, vs. wick thickness, δ , for several mesh sizes and two heat pipe diameters, D_o . Porous slab wick. Solid lines: vapour laminar flow; dotted lines: vapour turbulent flow. From Skrabek (1972) [88].	61
Figure 7-11: Heat Transfer, Q_{max} , and Integral Heat Transport Factor, $[Q \cdot I_{eff}]_{max}$, vs. wick thickness, δ , for several mesh sizes and two heat pipe diameters, D_o . Porous slab wick. Solid lines: vapour laminar flow; dotted lines: vapour turbulent flow. From Skrabek (1972) [88].	62
Figure 7-12: Heat Transfer, Q_{max} , and Integral Heat Transport Factor, $[Q \cdot I_{eff}]_{max}$, vs. wick thickness, δ , for several mesh sizes and two heat pipe diameters, D_o . Porous slab wick. Solid lines: vapour laminar flow; dotted lines: vapour turbulent flow. From Skrabek (1972) [88].	63
Figure 7-13: Heat pipe conductance, C , vs. wick thickness, δ , for several wick conductivities, k_{eff} , and two heat pipe diameters, D_o . Circumferential screen wick. From Skrabek (1972) [88].	64
Figure 7-14: Heat pipe conductance, C , vs. wick thickness, δ , for several wick conductivities, k_{eff} , and two heat pipe diameters, D_o . Circumferential screen wick. From Skrabek (1972) [88].	65
Figure 7-15: Heat pipe conductance, C , vs. wick thickness, δ , for several wick conductivities, k_{eff} , and two heat pipe diameters, D_o . Circumferential screen wick. From Skrabek (1972) [88].	66
Figure 7-16: Heat pipe conductance, C , vs. wick thickness, δ , for several values of the heat transfer coefficient of the wick, h , and heat pipe diameters, D_o . Porous slab wick. From Skrabek (1972) [88].	67
Figure 7-17: Heat pipe conductance, C , vs. wick thickness, δ , for several values of the heat transfer coefficient of the wick, h , and heat pipe diameters, D_o . Porous slab wick. From Skrabek (1972) [88].	68
Figure 7-18: Heat pipe conductance, C , vs. wick thickness, δ , for several values of the heat transfer coefficient of the wick, h , and heat pipe diameters, D_o . Porous slab wick. From Skrabek (1972) [88].	69
Figure 8-1: VCHP with cold reservoir.	71

Figure 8-2: VCHP with hot reservoir. (a) Internal hot reservoir. (b) External hot reservoir.....	72
Figure 8-3: Vapor concentration at the reservoir, $n(t)$, over its steady-state value, $n(\infty)$, and control temperature range, ΔT , as functions of time, t . From Hinderman, Waters & Kaser (1972) [35].....	73
Figure 8-4: Dimensionless pressure ratio, π_r , vs. control temperature range, $T_{E\max} - T_{E\min}$, for several working fluids. From Hinderman, Waters & Kaser (1972) [35].....	74
Figure 8-5: Sketch of a variable conductance heat pipe. 1: Evaporator. 2: Adiabatic Section. 3: Condenser. 4: Adiabatic Section. 5: Reservoir.	75
Figure 8-6: Dimensionless reservoir to condenser volume ratio, V_R/V_C , vs. evaporator temperature variation, $(T_{E\max} - T_{E\min})$, for two different working fluids, and a given reservoir temperature variation, $(T_{R\max} - T_{R\min}) = 28$ K. From Edelstein & Hembach (1972) [23].....	75
Figure 8-7: Dimensionless reservoir to condenser volume ratio, V_R/V_C , vs. reservoir temperature variation, $(T_{R\max} - T_{R\min})$, with fixed evaporator control temperature variation, $(T_{E\max} - T_{E\min}) = 6$ K. From Edelstein & Hembach (1972) [23].	76
Figure 8-8: Dimensionless reservoir to condenser volume ratio, V_R/V_C , vs. evaporator temperature variation, $(T_{E\max} - T_{E\min})$, for ammonia working fluid. From Edelstein & Hembach (1972) [23].....	76
Figure 8-9: Dimensionless reservoir to condenser volume ratio, V_R/V_C , vs. evaporator temperature variation, $(T_{E\max} - T_{E\min})$. Solid lines: cold reservoir. Dashed lines: hot reservoir. (A) and (M) correspond to ammonia and methanol respectively. T_s is the sink temperature; in one case the back of the radiator is painted black (222 K $< T_s < 254$ K), and in the other it is aluminized (196 K $< T_s < 245$ K). Evaporator temperature, $T_E = (287 + (T_{E\max} - T_{E\min})/2)$ K. From Kirkpatrick & Marcus (1972) [42].	77
Figure 9-1: WR7 Heat Pipe Profile (Cryogenic Application)	83
Figure 9-2: WR12 Heat Pipe Profile	84
Figure 9-3: WR18 Heat Pipe Profile	84
Figure 9-4: WR19 Heat Pipe Profile	85
Figure 9-5: WR20 Heat Pipe Profile	85
Figure 9-6: WR22 Heat Pipe Profile	86
Figure 9-7: WR24 Heat Pipe Profile	86
Figure 9-8: WR25 Heat Pipe Profile	87
Figure 9-9: WR26 Heat Pipe Profile	87
Figure 9-10: WR27 Heat Pipe Profile	88
Figure 9-11: WR28 Heat Pipe Profile	88
Figure 9-12: WR29 Heat Pipe Profile	89
Figure 9-13: WR7 Heat Pipe used for SCIAMACHY on ENVISAT	89
Figure 9-14: EADS ASTRUM HP experience	90
Figure 9-15: EHP: typical Aluminium extruded HP	91

Figure 9-16: Heat transport capability – NH3 (Note: AG110 = size 11 mm in tens of millimetres.)	94
Figure 9-17: HP Profile Tolerances	97
Figure 9-18: HP Profile Tolerances (cont.)	98
Figure 9-19: HP Profile Tolerances (cont.)	99
Figure 9-20: ESA SMART 1 with HP	100
Figure 9-21: ESA AEOLUS – ALADIN instrument with HP network	100
Figure 9-22: Constant Conductance Heat Pipe	101
Figure 9-23: Variable Conductance Heat Pipe	101
Figure 9-24: Heat Pipe Profiles examples Table 9.2-3. Stainless Steel Heat Pipes types.	102
Figure 9-25: <i>“Thank to 40 state-of-the art variable conductance heat pipes located in the avionics bay the ATV is able to carry away the heat and release the energy directly into space or, otherwise, to warm up other parts in a very economic fashion”</i> Astrium – ESA “Jules Verne goes hot and cold” – Successful achievement of the Qualification Thermal Test campaign – 14 Dec 2006.	104
Figure 9-26: Stainless Steel HP Performance curves	105
Figure 9-27: Stainless Steel HP Performance curves (cont.)	105
Figure 9-28: Axial Grooved HP profiles	106
Figure 9-29: Axial Grooved HP profiles drawings	107
Figure 9-30: Dependence of AGHP Heat Transfer Capacity on Working Fluid (Ammonia)	108
Figure 9-31: Influence of tilt angle on AGHP maximum Heat Transfer Capacity at 20°C ...	108
Figure 9-32: Thermal performance of Arterial HP with different working fluids	109
Figure 9-33: Experimental data for Arterial HP with ammonia	109
Figure 9-34: Arterial HP profile schematics	110
Figure 9-35: Arterial HP typical configurations	110
Figure 9-36: Arterial HP for rotator application. Length 2400 mm. Power 150 W.	111
Figure 9-37: 0g guaranteed heat transport capability for ThalesAlenia Space Heat Pipes	112
Figure 9-38: Mono-core heat pipe profile	113
Figure 9-39: Dual-core heat pipe profiles	114
Figure 9-40: Minimal dimensions of straight parts for Ø 12.2 bent heat pipe	115
Figure 10-1: Operating temperature range for cryogenic working fluids. Data from ECSS-E-HB-31-01 Part 14, Table 8-1, clause 8.1.1. For fluorine: melting point, $T = 53.5$ K, critical point, $T = 144$ K.....	117
Figure 10-2: Figure of Merit, N , as a function of temperature, T , for several cryogenic working fluids. Compare with Figure 6-8, clause 6.3. Replotted after Chi & Cygnarowicz (1970) [15].	118
Figure 10-3: Axial distribution of porosity, ϕ , and cross section of a graded-porosity slab wick. From Groll, Pittman & Eninger (1976) [30].	121

Figure 10-4: Maximum heat transport factor, ($Q \cdot I_{eff}$), for a homogeneous wick heat pipe as a function of inner diameter, D_i , for different gravity levels. a) Working fluid is Nitrogen at 77 K. b) Oxygen at 77 K. From Joy (1970) [38].	124
Figure 10-5: Maximum heat transport factor, ($Q \cdot I_{eff}$), for an axially grooved heat pipe and for a homogeneous wick heat pipe vs. inner diameter of the pipe, D_i , for different gravity levels. Working fluid is Oxygen at 77 K. From Joy (1970) [38].	125
Figure 10-6: Axial temperature drop, ΔT , for Oxygen heat pipes at 77 K vs. inner diameter of the pipe, D_i . Also shown are data for an axially grooved heat pipe and for aluminium rods of the same diameter. From Joy (1970) [38]. Calculation procedure is outlined in the text.	126
Figure 10-7: Nodal points in the static transient model of a heat pipe. From Smirnov, Barsookov & Mishchenko (1976) [89].	127
Figure 10-8: Schematic of the heat pipe considered by Chang & Colwell (1985) [13].	128
Figure 10-9: ERTS-C (Landsat III) cryogenic heat pipe experiment configuration. From Brennan & Kroliczek (1975) [45].	130
Figure 10-10: Schematic of a blocking orifice thermal diode heat pipe. From Kosson, Quadrini & Kirckpatrick (1974) [44].	131
Figure 10-11: a) Axial temperature profiles during reverse mode tests of a cryogenic heat pipe diode. No tilt. Tests performed in an insulated LN_2 cooled enclosure. At time 0 power (3 W) is removed from the evaporator, and the reservoir heater is on. T_o is the ambient temperature within the enclosure. b) Shut-down temperature response of evaporator and upstream end of blocked transport section. From Quadrini & McCreight (1977) [66].	133
Figure 10-12: Axial temperature profiles during reverse mode tests. Tests performed as in Figure 10-11a except 1 W heat load on the evaporator continuously fed during the run. T_o is the ambient temperature within the enclosure. From Quadrini & McCreight (1977) [66].	134
Figure 10-13: Cross section of Heat Pipe 2. From Murakami & Kaido (1980) [61]. All the dimensions are in mm.	135
Figure 10-14: Temperature, T , vs. heat transfer rate, Q , in Heat Pipe 3. T_1 is the evaporator temperature, T_2 and T_3 are in the adiabatic clause 88×10^{-3} m and 78×10^{-3} m from the evaporator end. The sink temperature is $T_s = 1,9$ K. From Murakami (1982) [60].	136
Figure 10-15: Critical heat transfer rate, Q_c , and l-transition heat transfer rate, Q_λ , for the three heat pipes as a function of sink temperature, T_s . From Murakami (1982) [60]. Key is given below.	137
Figure 10-16: Integral heat transport factor, $(Q \cdot I_{eff})_{max}$, vs. operating temperature, T , of the cryogenic heat pipes tabulated in Table 10-4.	145

Tables

Table 5-1: Empirical Correlations for the Determination of Wick Properties	21
Table 5-2: Properties of Wick Materials	23
Table 6-1: Chemical Compatibility between Typical Wick Materials and Working Fluids.	47
Table 7-1: Combinations of Temperatures, Working Fluids, Wick and Container Materials, and Heat Pipe Outer Diameters.	57

Table 9-1: Selected Aluminium Heat Pipe Profiles.....	79
Table 9-2: Aluminium Heat Pipe Profiles (cont.)	80
Table 9-3: Aluminium Heat Pipe Profiles (cont.)	81
Table 9-4: Aluminium Heat Pipe Profiles (cont.)	82
Table 9-5: Aluminium Heat Pipe Profiles (cont.)	83
Table 9-6: EHP Aluminium Heat Pipes Performance.....	92
Table 9-7: Available HP Profiles.....	95
Table 9-8: Stainless Steel Heat Pipes types	102
Table 9-9: Geometrical Parameters	107
Table 9-10: Thermal Performances of ThalesAlenia Space Heat Pipes (*): QL _{max} 6mm guaranteed.....	112
Table 9-11: Mass of ThalesAlenia Space Heat Pipes	113
Table 9-12: External geometries of ThalesAlenia Space Heat Pipes.....	114
Table 10-1: Main Features of Cryogenic Fluids in Heat Pipes, Consequences	116
Table 10-2: Wicking Structures. Current Technology.....	118
Table 10-3: Evolution of Vapor to Liquid Kinematic Viscosity Ratio over Working Temperature Range ^a	123
Table 10-4: Characteristics of Tested Cryogenic Heat Pipes.....	138
Table 10-5: Characteristics of Tested Cryogenic Heat Pipes, Materials	140
Table 10-6: Characteristics of Tested Cryogenic Heat Pipes, Operating Conditions	142

1**Scope**

Heat pipes are a solution to many thermal dissipation problems encountered in space systems.

The types of heat pipes that can be used in spacecrafts are described. Details on design and construction, usability, compatibility and the limitations of each type are given.

The Thermal design handbook is published in 16 Parts

ECSS-E-HB-31-01 Part 1	Thermal design handbook – Part 1: View factors
ECSS-E-HB-31-01 Part 2	Thermal design handbook – Part 2: Holes, Grooves and Cavities
ECSS-E-HB-31-01 Part 3	Thermal design handbook – Part 3: Spacecraft Surface Temperature
ECSS-E-HB-31-01 Part 4	Thermal design handbook – Part 4: Conductive Heat Transfer
ECSS-E-HB-31-01 Part 5	Thermal design handbook – Part 5: Structural Materials: Metallic and Composite
ECSS-E-HB-31-01 Part 6	Thermal design handbook – Part 6: Thermal Control Surfaces
ECSS-E-HB-31-01 Part 7	Thermal design handbook – Part 7: Insulations
ECSS-E-HB-31-01 Part 8	Thermal design handbook – Part 8: Heat Pipes
ECSS-E-HB-31-01 Part 9	Thermal design handbook – Part 9: Radiators
ECSS-E-HB-31-01 Part 10	Thermal design handbook – Part 10: Phase – Change Capacitors
ECSS-E-HB-31-01 Part 11	Thermal design handbook – Part 11: Electrical Heating
ECSS-E-HB-31-01 Part 12	Thermal design handbook – Part 12: Louvers
ECSS-E-HB-31-01 Part 13	Thermal design handbook – Part 13: Fluid Loops
ECSS-E-HB-31-01 Part 14	Thermal design handbook – Part 14: Cryogenic Cooling
ECSS-E-HB-31-01 Part 15	Thermal design handbook – Part 15: Existing Satellites
ECSS-E-HB-31-01 Part 16	Thermal design handbook – Part 16: Thermal Protection System

2

References

ECSS-S-ST-00-01	ECSS System - Glossary of terms
ECSS-E-HB-31-01 Part 10	Thermal design handbook – Part 10: Phase-Change Capacitors
ECSS-E-HB-31-01 Part 13	Thermal design handbook – Part 13: Fluid Loops
ECSS-E-HB-31-01 Part 14	Thermal design handbook – Part 14: Cryogenic Cooling

All other references made to publications in this Part are listed, alphabetically, in the **Bibliography**.

3**Terms, definitions and symbols****3.1 Terms and definitions**

For the purpose of this Standard, the terms and definitions given in ECSS-S-ST-00-01 apply.

3.2 Symbols

A_v	vapour core cross-sectional area, [m ²]
A_w	wick cross-sectional area, [m ²].
C	heat pipe thermal conductance, [W.K ⁻¹]
C_i	heat capacity associated to node i , [J.K ⁻¹]
D_i	inner wall diameter of the pipe, [m]
D_o	outer wall diameter of the pipe, [m]
D_p	diameter of particles, [m]
D_v	diameter of the vapour space, [m]
H	equilibrium capillary height, [m]
H_{ij}	heat transfer coefficient between nodes i and j , [W.K ⁻¹]
K	permeability, [m ²]
M	molar mass, [kg.mol ⁻¹]
N	figure of merit, [W.m ⁻²] $N = \rho h_g \sigma / \mu$
Q	heat transfer rate, [W]
$(Q.l_{eff})$	integral heat transport factor, [W.m]
R	universal gas constant, $R = 8,3143 \text{ J.K}^{-1}.\text{mol}^{-1}$
R_g	gas constant of a particular gas, [J.K ⁻¹ .kg ⁻¹] $R_g = R/M$
Re	Reynolds number, $Re = \rho V D_i / \mu$

T	temperature, [K]
T_s	sink temperature, [K]
ΔT	Clause 5: radial temperature drop between vapour-liquid interface and heat pipe wall, [K] Clause 8: control temperature range of a VCHP, [K] Clause 10: axial temperature drop, [K]
V	Clause 7: velocity, [m.s ⁻¹] Clause 8: volume, [m ³]
We	Weber number, $We = \rho_v(V_v)^2 l' / \sigma$
a	velocity of sound, [m.s ⁻¹]
b	dimensionless constant of a capillary structure, see clause 7.2.1.1
g	acceleration due to gravity, [m.s ⁻²]
h	heat transfer coefficient of the wick, [W.m ⁻² .K ⁻¹]
h_{fg}	latent heat of vaporization, [J.kg ⁻¹]
k	thermal conductivity, [W.m ⁻¹ .K ⁻¹]
k_{eff}	effective thermal conductivity of the wick, [W.m ⁻¹ .K ⁻¹]
k_w	thermal conductivity of the wick material, [W.m ⁻¹ .K ⁻¹]
l	length, [m]
l'	characteristic length associated with the wick surface, [m] it is used to define the Weber number
l_{eff}	effective heat pipe length, [m] $l_{eff} = l_A + (l_C + l_E)/2$
l_w	wick length, [m]
m	mass flow rate, [kg.s ⁻¹]
ṁ	mass flow rate per unit area, [kg.m ⁻² .s ⁻¹] it is also called mass flux
n	number of moles
p	pressure, [Pa]
p_a	standard atmospheric pressure, $p_a = 1,01325 \times 10^5$ Pa
Δp	pressure drop, [Pa]

Δp_c	capillary pumping pressure, [Pa]
q	radial heat flux, [W.m ⁻²]
r	radius, [m]
r_b	radius of bubble nucleus, [m]
r_c	effective pore radius of the capillary structure, [m]
t	Time, [h]
w	groove width, [m]
w'	fin thickness, [m]
x	coordinate along heat pipe, [m] it is measured from the evaporator
Π	wetted perimeter of a duct, [m]
Φ	wick porosity
γ	vapor specific heat ratio
δ	wick thickness or groove depth, [m]
θ	wetting angle, [angular degrees]
θ_E	wetting angle in the evaporator, [angular degrees]
μ	dynamic viscosity, [Pa.s]
ν	Clauses 5 and 7: liquid to wick material thermal conductivity ratio
	Clause 10: kinematic viscosity, [m ² .s ⁻¹]
π_r	dimensionless pressure ratio
ρ	density, [kg.m ⁻³]
σ	surface tension, [N.m ⁻¹]
τ	shear stress, [Pa]
ϕ	tilting angle, [angular degrees], positive when the evaporator is up
ψ	geometrical parameter, it is defined in clause 11.2.1.2

Subscripts

A	adiabatic
C	condenser
E	evaporator
R	reservoir
b	normal boiling conditions
c	Clause 6: thermodynamic critical conditions Clause 7: capillary
	Clause 10: superfluid dynamics critical conditions
eff	effective
f	freezing conditions
i	inner wall
l	liquid phase
max	maximum
min	minimum
o	Clause 6: reference temperature conditions Clauses 7, 8 and 10: outer wall
sat	saturation conditions
v	vapour phase
w	wick material
λ	helium-4 conditions at the Lambda point

Other symbols, mainly used to define the geometry of the configuration, are introduced when required.

4

General introduction

The heat pipe is a thermal device which affords an efficient transport of thermal energy. It is constituted by a closed structure containing a working fluid which transfers the thermal energy from one part (evaporator) to another (condenser). The phenomena involved in the transfer process are the following:

1. Vaporization in the evaporator;
2. vapor flow in the core region of the container;
3. condensation in the condenser, and
4. liquid return to the evaporator by capillary action in the wick.

The capillary pumping permits to the heat pipe to be operated in any orientation, in contrast to evaporation cooling devices which can only work when the evaporator is placed at the lowest point of the system.

The pressure variations in the vapor core are normally small and, therefore, the heat pipe temperature is nearly uniform and close to the saturated vapor temperature corresponding to the vapor pressure. The capability of transporting large amounts of thermal energy between two terminals (evaporator and condenser) with a small temperature difference is the main characteristic of the heat pipe which can be considered an extra-high thermal conductivity device in the Fourier's law sense.

In addition to its superior heat transfer characteristics, the heat pipe is structurally simple, relatively inexpensive, insensitive to the gravitational field, and silent and reliable in its operation. It can be made into different shapes and, by using the working fluid best suited to the desired temperature range, can operate at temperature ranging from the cryogenic regions up to high temperature levels which are only limited by structural reasons.

Because the immense potential of heat pipes, they have been employed in many engineering applications, spacecraft thermal control not being an exception.

Classical papers concerning heat pipes are those by Grover et al. (1964) [32] and Cotter (1965) [18]. A presentation of the background required by those wishing to use or to design heat pipes has been made by Dunn & Reay (1976) [21].

Several examples of application of heat pipes to spacecraft are given in the following:

1. It is well known that large temperature variations may occur in the surface of a spacecraft because non-uniform heating. These temperature variations can cause a host of problems including undesirable thermal stresses. Katzoff (1967) [39] has recommended the use of long heat pipes wrapped around the outer surface of a spacecraft to accomplish the necessary equalization of the temperature distribution.
2. Another application which has received considerable attention is the cooling of electronic components of spacecraft systems. These components are often located in the interior of

the satellite, and the aim of the heat pipe is to transfer the waste heat over some distance for ultimate rejection to outer space.

3. The use of radiators formed by heat pipes has been suggested several times. The heat pipes produce nearly uniform temperatures on the radiator surface, and the redundancy achieved when used in parallel arrangement provides some degree of increased meteor protection to the radiator.

Intensive heat pipe research and development have resulted in rapid advancement in a variety of directions: from the simple cylindrical shape to complex geometries; from a screen mesh to multicomponent capillary-wick structures; from a passive variable-temperature conduction link to self-controlled, variable-conductance, constant-temperature devices, and from the high conductance function to a multitude of thermal control functions (such as switching, transformer, diode, and damping, among others). Considerable progress has been made in material compatibility, fabrication technology, and operational handling.

Since the heat pipe is both lightweight and nearly isothermal it appears to provide ideal solutions to many thermal dissipation problems encountered in spacecraft.

5

Heat pipe wicks

5.1 General

The heat pipe utilized for its operation capillary induced fluid flow, instead of gravitational or mechanical work. This particular feature has led to considerable research efforts aimed at developing wick materials suitable for use as capillary pumping devices in heat pipes.

The primary requisite for a heat pipe wick is that it should act as an effective capillary pump. That is, the surface tension forces developed between the fluid and the wick structure should be sufficient to overcome all viscous and other pressure drops in the pipe, still maintaining the required fluid circulation.

In addition to the operating characteristics, several mechanical features should be considered when evaluating candidate heat pipe wicks. The wick should be mechanically stable and rigid enough to avoid changing of flow properties in response to wick sagging or stretching. On the other hand, the suitable wick material should be compatible with the working fluid used. Many of the problems associated with long term heat pipe operation are a direct consequence of material incompatibility which usually manifests itself in chemical reactions.

A wide variety of wicks has been successfully employed in heat pipes. The first, and still the most widely used, consists of several layers of fine mesh screen. Different methods have been used to assure mechanical contact between the screen and the container. The reader is referred for further details to: Neal (1967) [63], Katzoff (1967) [39], Kemme (1968) [41], and McKinney (1969) [58], among others.

Screens have been also used merely as a retaining structure for wicks consisting in various types of beads packed in an annulus between the retaining screen and the pipe wall. Beads of Monel, glass, and stainless steel of different diameters have been used to produce these wicks.

Textile fabrics have also been employed as wicks. Rayon cloth has been used for a nitrogen heat pipe (Haskin (1967) [33]). The cloth was held firmly against the heat pipe wall by sliding together two valves of a slotted, diagonally cut retaining tube. Commercially available quartz fiber cloth has been used as wick for flexible heat pipes (Shlosinger et al. (1966) [87]). In these devices the cloth was pressed against the wall with springs. Attempts to bond the cloth to the wall met only with limited success. A good bonding was achieved by applying heat sealable film materials, such as thermosetting and thermoplastic sheets of the polyester resins.

Other investigators have experimented with commercially available porous metals, using sintered fiber wicks (Neal (1967) [63]).

In addition, wicks have been successfully fabricated from powders of Al_2O_3 , SiC , Al , Cu , and Ni .

5.2 Basic properties

The properties which characterize the behavior of heat pipe wicks are: equilibrium capillary height, permeability, and effective thermal conductivity.

5.2.1 Equilibrium capillary height

Equilibrium capillary height, H , is the maximum height to which a wick lifts a given fluid. Two considerations underline the importance of this variable for heat pipe design. First, the value of H limits the length of a heat pipe operating in a gravity field with the evaporator above the condenser. Second, H is used for evaluating the capillary pumping capability of a candidate wick. Once H has been determined, both the effective pore radius of the capillary structure, r_c , and the capillary pumping pressure, Δp_c , can be calculated (see Winter and Barsch (1971) [96])

$$r_c = (2\sigma \cos \theta) / (\rho_l g H),$$

$$\Delta p_c = 2\sigma / r_c.$$

Two different values of the capillary height can be measured in a porous structure: the rising value (wick initially dry) and the falling value (wick initially saturated). In general, the height to which a liquid will rise in a wick (rising height) is less, by approximately 25% (Katzoff (1967) [39]), than the height to which the liquid will fall in the same wick after it has been completely soaked (falling height).

5.2.2 Permeability

The permeability, K , of a porous body is the proportionality constant between mass flow rate and pressure drop (see Eq. (7.33), [ECSS-E-HB-31-01 Part 14, clause 7.4.2.4](#)). K has the dimension of an area and can be expressed by the following relationship (Ferrel & Johnson (1970) [26])

$$K = \frac{\mu_l Q}{h_{fg} \rho_l A_w} \frac{1}{\Delta p_l / l_w} \quad [5-1]$$

Note: non-si units are used in this figure

The permeability depends on the dimensions and geometry of the passages in the wick, and can be experimentally determined by measuring the pressure drop which experiences a given mass flow rate of a liquid flowing through the wick.

5.2.3 Effective thermal conductivity of the wick

The thermal energy required for vaporization (or condensation) is transferred by conduction, through the saturated wick, from the solid boundary surfaces to the liquid-vapor interface. Thence the effective thermal conductivity, k_{eff} , of the liquid saturated wick should be as large as possible.

The radial temperature drop between the liquid-vapor interface and the wall of the pipe can be calculated from the following expression (Grant (1973) [28]):

$$\Delta T = qD_i \left[\frac{\ln \frac{D_o}{D_i}}{2k_w} + \frac{\ln \frac{D_i}{D_v}}{2k_{eff}} \right] \quad [5-2]$$

Note: non-si units are used in this figure

Table 5-1 gives formulae for calculating the three wick properties which have been mentioned.

Table 5-1: Empirical Correlations for the Determination of Wick Properties

WICK PROPERTY	FORMULA	COMMENTS	Reference
Equilibrium Capillary Height, H.	$H = \frac{4\sigma}{0.41D_p\rho_l g}$ Note: non-si units are used in this figure	The pore diameter, $0.41 D_p$, corresponds to the largest minimum pore diameter existing in a cubic array of a randomly packed bed of spheres.	Ferrel & Alleavitch (1970) [25]
Permeability, K.	$K = \frac{D_p^2 \Phi^3}{150(1-\Phi)^2}$ Note: non-si units are used in this figure	Correlation between K and D_p is not very appropriate. Unfortunately no correlation exists, up to the moment, between K and more easily measurable wick characteristics.	Bird, Stewart & Lightfoot (1960) [10]
Dimensionless Effective Thermal Conductivity, k_{eff}/k_w .	$\frac{k_{eff}}{k_w} = (1-\Phi) + \nu\Phi$ Note: non-si units are used in this figure	It is assumed that the thermal conduction paths through liquid and through screen wick are parallel.	Neal (1967) [63], Kunz et al. (1968) [46]
	$\frac{k_{eff}}{k_w} = \frac{\nu}{\nu + \Phi(1-\nu)}$ Note: non-si units are used in this figure	It is assumed that the thermal conduction paths through liquid and through screen wick are in series.	Joy (1970) [38]
	$\frac{k_{eff}}{k_w} = \left(\frac{k_{eff}}{k_w} \right)_{drv} + \nu\Phi$ Note: non-si units are used in this figure	It is assumed that the thermal conduction paths through liquid and through screen wick are parallel.	Woo (1968) [97]

WICK PROPERTY	FORMULA	COMMENTS	Reference
	$\frac{k_{eff}}{k_w} = 0,046(1-\nu)(1-\Phi) + \nu \left[1 + \frac{0,954(1-\nu)(1-\Phi)}{1-(1-\nu)(1-\Phi)^{0,012}} \right]$ $0,65 \leq \Phi \leq 1$ <p>Note: non-si units are used in this figure</p>	Obtained from data concerning water-saturated nickel fiber wicks.	Soliman, Graumann & Berenson (1970) [91]
	$\frac{k_{eff}}{k_w} = 0,13(1-\nu)(1-\Phi) + \nu \left[1 + \frac{0,87(1-\nu)(1-\Phi)}{1-(1-\nu)(1-\Phi)^{0,006}} \right]$ $0,65 \leq \Phi \leq 1$	Obtained from data concerning water-saturated copper fiber wicks.	

5.3 Low resistance wicks

In addition to simple screen wicks, which have been already described, considerable attention has been paid to low resistance configurations.

There are three main different types of low resistance wicks.

1. Grooved heat pipes, with channels running axially along the inner surface of the tube. These configurations are structurally stable, have a large pipe wall to wick thermal conductance, and allow an ease control of pore size during manufacturing.
2. Composite wicks have been advocated by Kemme (1968) [41]. These wicks combine a material with fine pore size at the liquid vapor interface, with a larger pore size material underneath. The aim of the fine pores is to enhance the capillary effect, while the larger pores are introduced to expedite the return of the liquid.

Composite wicks may be manufactured either by combining screens of different mesh sizes, or by covering grooves which have been cut along the walls with a fine mesh size screen.

3. The condensed liquid can be delivered to the evaporator through one or more nearly cylindrical arteries, which are placed in the vicinity of the pipe center-line, and are extensions of the wick covering the inner wall of the pipe. This idea was set forth by Katzoff (1967) [39].

Table 5-2 in the following pages gives relevant properties for several combinations of wicking materials and working fluids.

Table 5-2: Properties of Wick Materials

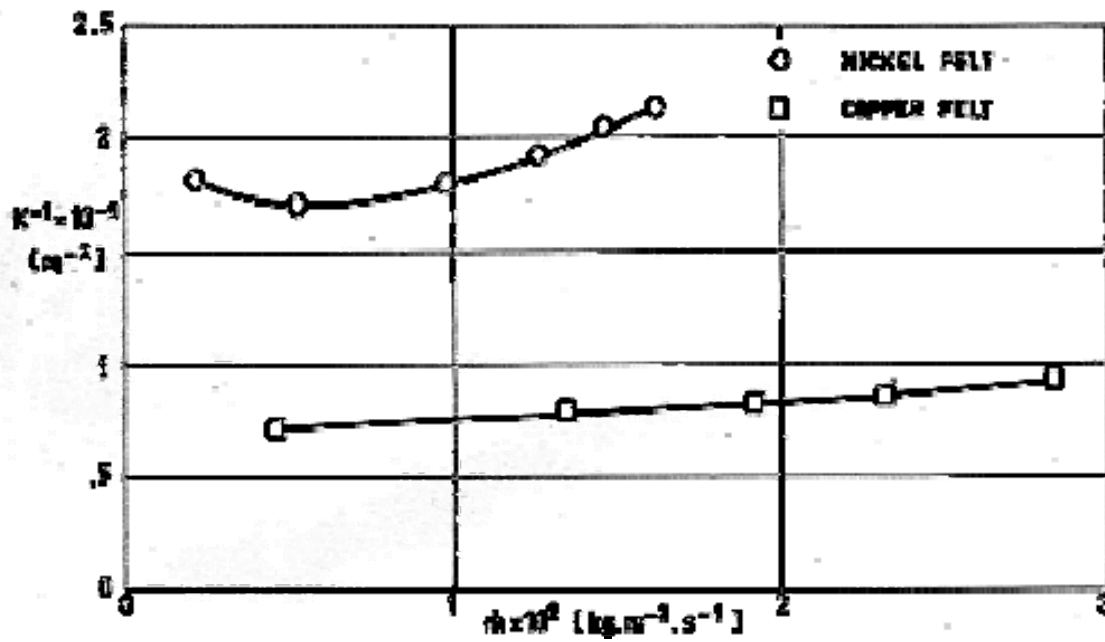
Wick Material (Supplier)	Fluid	Geometrical Characteristics	Φ	H [m]	$r_c \times 10^4$ [m]	$K \times 10^{10}$ [m ²]	k_{eff} [W.m ⁻¹ .K ⁻¹]		Ref.
							Dry	Saturated	
Bronze Mesh Screen	Methanol	Mesh Size = 74×10^{-6} m			0,535				f
	Water	Mesh Size = 74×10^{-6} m			0,61				g
Copper Sintered Powder $0,51 \times 10^{-3}$ m.Copper Backing. ^a	Water	$\delta = 0,79 \times 10^{-3}$ m	0,62	0,872		0,05			h
	Water	$\delta = 0,79 \times 10^{-3}$ m	0,70	0,816		0,06			
Copper Sintered Powder ^a	Water	$\delta = 1,3 \times 10^{-3}$ m	0,57	0,853		0,056	21,8	41,2	
Copper Felted Metal ^b	Benzene	$\delta = 2,5 \times 10^{-3}$ m	0,89		2,3	Figure 5-1			f
	Methanol	$\delta = 2,5 \times 10^{-3}$ m	0,89		2,15				
	Water	$\delta = 2,5 \times 10^{-3}$ m	0,89		2,8				
Copper Felted Metal ^c	Water	$\delta = 1,6 \times 10^{-3}$ m	0,59	0,311		0,43	22,3	78,3	
Copper Foam Amporcop 210-5 ^b	Benzene	$\delta = 0,46 \times 10^{-3}$ m	0,94		4,6	Figure 5-2			
	Methanol								
	Water	$\delta = 0,46 \times 10^{-3}$ m	0,94		4,3				
Copper Foam Amporcop 220-5 ^b	Water	$\delta = 2,6 \times 10^{-3}$ m	0,91		4,8				
Nickel Mesh Screen	Water	Mesh Size = 297×10^{-6} m	0,625	0,049		6,64			i
		Mesh Size = 74×10^{-6} m	0,679	0,112		1,52			
		Mesh Size = 74×10^{-6} m	0,676	0,234		0,77			

Wick Material (Supplier)	Fluid	Geometrical Characteristics	Φ	H [m]	$r_c \times 10^4$ [m]	$K \times 10^{10}$ [m ²]	k_{eff} [W.m ⁻¹ .K ⁻¹]		Ref.
							Dry	Saturated	
Nickel Powder	Freon 113	Powder Size Range = 297×10^{-6} – 841×10^{-6} m.	0,54	0,178		0,81			
	Freon 113	Powder Size Range = 297×10^{-6} – 841×10^{-6} m.	0,696	0,051		3			
	Water	Powder Size Range = 150×10^{-6} – 297×10^{-6} m.	0,658	0,247		2,73			
	Water	Powder Size Range = 297×10^{-6} – 841×10^{-6} m.	0,54	0,406		0,81			
	Water	Powder Size Range = 297×10^{-6} – 841×10^{-6} m.	0,696	0,175		3			
Nickel Fiber	Freon 113	Fiber Diameter = 10^{-5} m.	0,868	0,107		0,44			
	Freon 113	Fiber Diameter = 10^{-5} m.	0,825	0,125		0,34			
	Freon 113	Fiber Diameter = 10^{-5} m.	0,689	0,209		0,15			
	Freon 113	Fiber Diameter = $1,5 \times 10^{-5}$ m.	0,88	0,09		0,31			
	Water	Fiber Diameter = 10^{-5} m.	0,868	0,404		0,44			
	Water	Fiber Diameter = 10^{-5} m.	0,825	0,406		0,34			
	Water	Fiber Diameter = 10^{-5} m.	0,689	0,406		0,15			
	Water	Fiber Diameter = $1,5 \times 10^{-5}$ m.	0,88	0,399		0,31			

Wick Material (Supplier)	Fluid	Geometrical Characteristics	Φ	H [m]	$r_c \times 10^4$ [m]	$K \times 10^{10}$ [m ²]	k_{eff} [W.m ⁻¹ .K ⁻¹]		Ref.
							Dry	Saturated	
Nickel Felted Metals ^c	Water	$\delta = 1,9 \times 10^{-3}$ m	0,82	0,292		0,6	2,97	5,5	^h
	Water	$\delta = 2,1 \times 10^{-3}$ m	0,61	0,582		0,08	16,6	26,3	
Nickel Felted Metals ^b	Water	$\delta = 2,5 \times 10^{-3}$ m	0,89		1,65	Figure 5-1			^f
Nickel Foam Ampornick 220-5 ^b	Benzene	$\delta = 2,5 \times 10^{-3}$ m	0,96		2,1	Figure 5-2			
	Methanol	$\delta = 2,5 \times 10^{-3}$ m	0,96		2,6				
	Water	$\delta = 2,6 \times 10^{-3}$ m	0,96		2,3				
Nickel Foam Ampornick 210-5 ^b	Water	$\delta = 2,6 \times 10^{-3}$ m	0,94		2,3				
Stainless Steel Mesh Screen ^d	Benzene	Mesh Size = 74×10^{-6} m $\delta = 0,89 \times 10^{-4}$ m	0,73		0,57				
	Methanol	Mesh Size = 74×10^{-6} m $\delta = 0,89 \times 10^{-4}$ m	0,73		0,54				
	Water	Mesh Size = 74×10^{-6} m $\delta = 0,89 \times 10^{-4}$ m	0,73		0,58				
Stainless Steel Mesh Screen ^e	Water	Mesh Size = 420×10^{-6} m 6 layers	0,69	0,054		3,7	0,692	3,86	^h
	Water	Mesh Size = 149×10^{-6} m 10 layers	0,63	0,109		2,1	0,692	4,5	
	Water	Mesh Size = 111×10^{-6} m 22 layers	0,68	0,143		0,8	0,657	3,51	
	Water	Mesh Size = 74×10^{-6} m 32 layers	0,69	0,199		0,54			
Stainless	Water	$\delta = 2,8 \times 10^{-3}$ m	0,32	1,02		0,049	3,04	11,4	

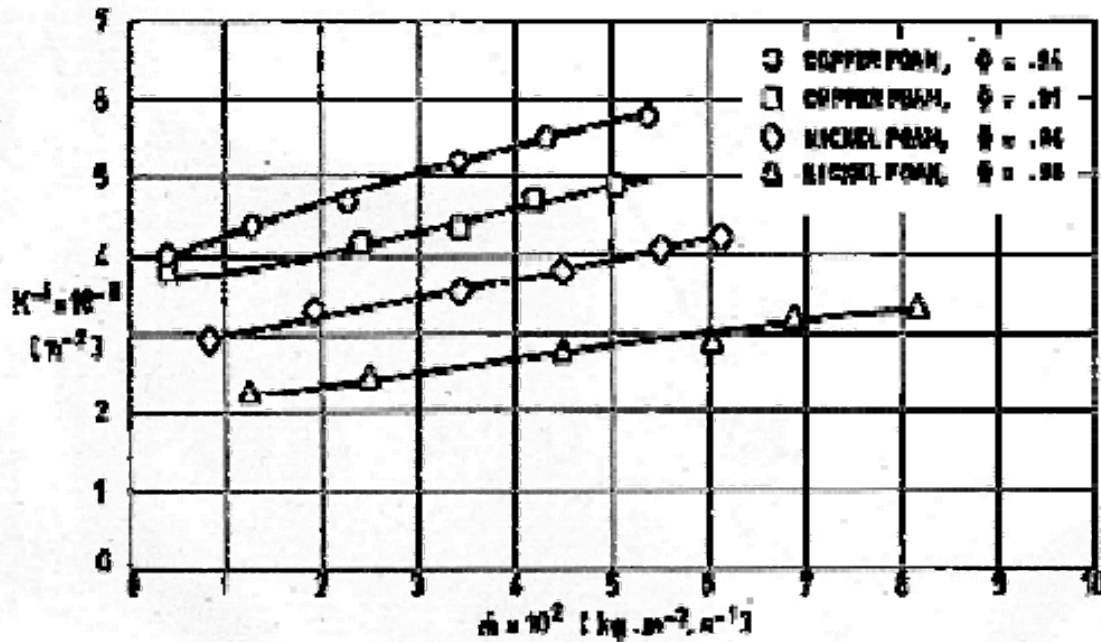
Wick Material (Supplier)	Fluid	Geometrical Characteristics	Φ	H [m]	$r_c \times 10^4$ [m]	$K \times 10^{10}$ [m ²]	k_{eff} [W.m ⁻¹ .K ⁻¹]		Ref.
							Dry	Saturated	
Steel Sintered Powder ^e	Water	$\delta = 2,8 \times 10^{-3}$ m	0,47	0,539		0,16	2,06	6,88	
	Water	$\delta = 2,8 \times 10^{-3}$ m	0,57	0,304		0,42	2,21	6,04	
Stainless Steel Fiber Materials (SS-430)	Water	Fiber Diameter = $3,3 \times 10^{-5}$ m	0,916	0,155		5,46			i
	Water	Fiber Diameter = $3,3 \times 10^{-5}$ m	0,808	0,227		1,96			
	Water	Fiber Diameter = $7,6 \times 10^{-5}$ m	0,822	0,135		11,61			
Stainless Steel Felted Metals ^c	Water	$\delta = 3 \times 10^{-3}$ m	0,89	0,067		5,96	0,74	2,45	h
	Water	$\delta = 3,2 \times 10^{-3}$ m	0,80	0,119		2,69	1,18	3,27	
	Water	$\delta = 3,2 \times 10^{-3}$ m	0,58	0,256		0,54	4,2	9,6	

^a Gold Inc.^b Astro Met Associates Inc.^c Huyck Metals Co.^d Michigan Wire Cloth Co.^e Gerard Daniel & Co.^f Phillips & Hinderman (1969) [67]^g Katzoff (1967) [39]^h Ferrel, Alexander & Piver (1973) [24]ⁱ Langston & Kunz (1969) [48]



Note: non-si units are used in this figure

Figure 5-1: Measured values of the inverse permeability, K^{-1} , vs. mass flow rate per unit area, \dot{m} .> From Phillips & Hinderman (1969) [67].



Note: non-si units are used in this figure

Figure 5-2: Measured values of the inverse permeability, K^{-1} , vs. mass flow rate per unit area, \dot{m} .> From Phillips & Hinderman (1969) [67].

6

Heat pipe working fluids

6.1 General

A wide variety of fluids ranging from cryogens to liquid metals have been used as heat pipe working fluids.

The choice of a working fluid for a heat pipe application is dictated to a large extent by several physical properties of the fluid and by chemical compatibility of the fluid with the container and the wick. The requirements which should be taken into account when selecting a heat pipe working fluid are the following:

1. High latent heat of vaporization.
2. High thermal conductivity.
3. Low viscosity.
4. High surface tension.
5. High wetting ability.
6. Boiling point suited to the required operating temperature.

In order to minimize the temperature change associated to a given pressure drop, the fluids should be used in a steeply sloped region of its vapor pressure-temperature curve.

The ranking of the working fluids within a particular temperature range is usually established by means of a dimensional fluid property group, named figure or merit, which has dimensions of heat flux [$\text{W} \cdot \text{m}^{-2}$], and is defined as:

$$N = \rho h_{fg} \sigma / \mu$$

Relevant physical properties of suitable heat pipe working fluids are presented in this clause. These properties are:

1. Vapour Pressure, p_{sat} . [Pa].
2. Latent Heat of Vaporization, h_{fg} . [$\text{J} \cdot \text{kg}^{-1}$].
3. Density of Liquid Phase, ρ_l . [$\text{kg} \cdot \text{m}^{-3}$].
4. Density of Vapor Phase, ρ_v . [$\text{kg} \cdot \text{m}^{-3}$].
5. Dynamic Viscosity of Liquid Phase, μ_l . [Pa.s].
6. Dynamic Viscosity of Vapor Phase, μ_v . [Pa.s].
7. Thermal Conductivity of Liquid Phase, k_l . [$\text{W} \cdot \text{m}^{-1} \cdot \text{K}^{-1}$].
8. Thermal Conductivity of Vapor Phase, k_v . [$\text{W} \cdot \text{m}^{-1} \cdot \text{K}^{-1}$].
9. Surface Tension, σ . [$\text{N} \cdot \text{m}^{-1}$].

10. Figure of Merit, N . [W.m⁻²].

The mathematical expressions used for the evaluation of these properties have been summarized in Clause 6.2. The resulting values of the mentioned properties have been presented in graphical form in Clause 6.3.

6.2 Empirical correlations

The following expressions have been used for the numerical calculation of the relevant physical properties of heat pipe working fluids. Additional details can be found in books like Reid & Sherwood (1966) [70]. Sources of experimental data are indicated in the sheets concerning the different fluids.

- Vapour Pressure, p_{sat} . [Pa], Riedel-Plank-Miller formula:

$$\log \frac{p_{sat}}{p_c} = -\frac{G}{T/T_c} \left[1 - \left(\frac{T}{T_c} \right)^2 + g \left(1 - \frac{T}{T_c} \right)^3 \left(3 + \frac{T}{T_c} \right) \right] \quad [6-1]$$

Note: non-si units are used in this figure

where

$$G = 0,21 + 0,4605 \frac{T_b}{T_c - T_b} \log \frac{p_c}{p_a} \quad [6-2]$$

Note: non-si units are used in this figure

$$g = \frac{\frac{T_b}{G(T_c - T_b)} \log \frac{p_c}{p_a} - \left(1 + \frac{T_b}{T_c} \right)}{\left(1 - \frac{T_b}{T_c} \right)^2 \left(3 + \frac{T_b}{T_c} \right)} \quad [6-3]$$

Note: non-si units are used in this figure

- Latent Heat of Vaporization, h_{fg} . [J.kg⁻¹], Theisen formula:

$$h_{fg} = H \left(1 - \frac{T}{T_c} \right)^{n_h} \quad [6-4]$$

Note: non-si units are used in this figure

H and n_h are deduced from the experimental data by using the least squares technique.

- Density of Liquid Phase, ρ_l . [kg.m⁻³], Benson formula:

$$\rho_l = 2\rho_c - \rho_v + \frac{T_c - T}{T_c - T_b} (\rho_{lb} - 2\rho_c) \quad [6-5]$$

Note: non-si units are used in this figure

- Density of Vapor Phase, ρ_v . [kg.m⁻³], Redlich-Kwong state equation:

$$\left[p + \frac{1,2826R_g T_c \rho_v^2}{\left(\frac{T}{T_c}\right)^{0.5} (\rho_c + 0,2599 \rho_v)} \right] (\rho_c - 0,2599 \rho_v) = R_g T \rho_v \rho_c \quad [6-6]$$

Note: non-si units are used in this figure

- Dynamic Viscosity of Liquid Phase, μ_l . [Pa.s], Girifalco formula:

$$\mu_l = \exp \left[\sum_0^n A_n T^{-n} \right] \quad [6-7]$$

Note: non-si units are used in this figure

The coefficients A_n are deduced from the experimental data by using the least squares technique.

- Dynamic Viscosity of Vapor Phase, μ_v . [Pa.s], Sutherland formula:

$$\mu_v = \frac{b T^{3/2}}{s + T} \quad [6-8]$$

b and s are deduced from the experimental data by using the least squares technique.

- Thermal Conductivity of Liquid Phase, k_l . [W.m^{-1.K⁻¹]:}

$$k_l = k_{lo} \left[1 + \sum_1^n B_n (T - T_o)^n \right] \quad [6-9]$$

The coefficients B_n are deduced from the experimental data by using the least squares technique.

- Thermal Conductivity of Vapor Phase, k_v . [W.m^{-1.K⁻¹], Owens-Thodos formula:}

$$k_v = K \left(\frac{T}{T_c} \right)^{n_k} \quad [6-10]$$

K and n_k are deduced from the experimental data by using the least squares technique.

- Surface Tension, σ . [N.m⁻¹].

$$\sigma = D \left(1 - \frac{T}{T_c} \right)^{n_\sigma} \quad [6-11]$$

D and n_σ are deduced from the experimental data by using the least squares technique.

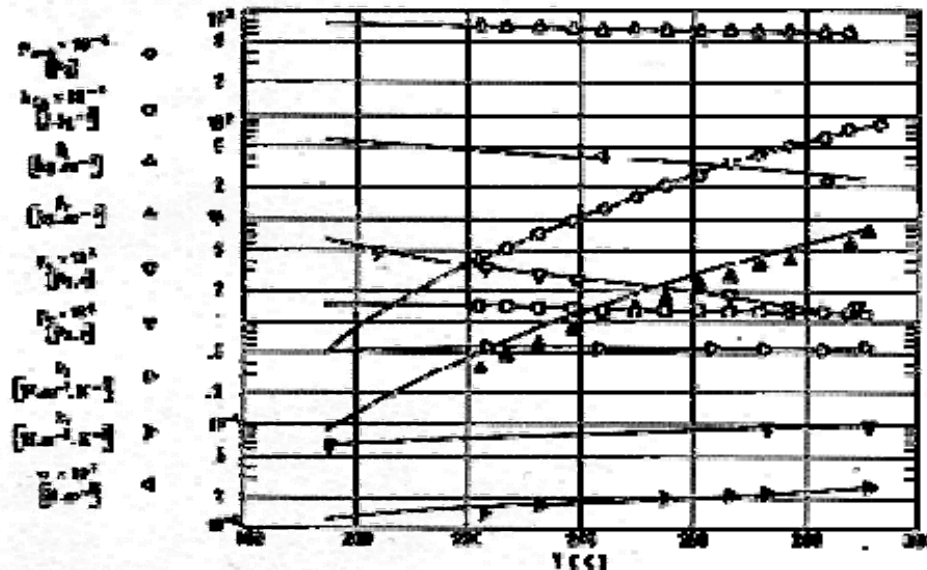
6.3 Physical properties

The working fluid properties given in this clause are those listed in Clause 6.2. The fluids are, in order of appearance,

Ammonia
Ethanol
Freon 11
Methanol
Nitrogen
Propane
Water

A sheet dealing with a given fluid is arranged as follows: The available data are summarized in a figure and the particular expressions used to correlate them are presented in the following. The sources of the experimental data presented are given in the table below.

FLUID: AMMONIA	$T_b = 239,8$ K	$p_c = 1,1297 \times 10^7$ Pa
CHEMICAL SYMBOL: NH ₃	$T_c = 405,6$ K	$\rho_c = 235$ kg.m ⁻³
MOLAR MASS: 17,032	$T_f = 195,3$ K	$\rho_{lb} = 681,8$ kg.m ⁻³



Note: non-si units are used in this figure

Figure 6-1: Relevant physical properties of Ammonia as a function of temperature, T , The labels correspond to experimental points. The expressions used to calculate the tabulated values are given below. Calculated by the compiler.

Formulae Used for Calculating the Values of the Physical Properties.

$$\log \frac{p_{sat}}{p_c} = -\frac{2,9619}{T/T_c} \left[1 - \left(\frac{T}{T_c} \right)^2 + 0,4843 \left(1 - \frac{T}{T_c} \right)^3 \left(3 + \frac{T}{T_c} \right) \right] \quad [6-12]$$

Note: non-si units are used in this figure

$$h_{fg} = 1,9152 \times 10^6 \left(1 - \frac{T}{T_c} \right)^{0,3737}, \quad 198 < T < 405 \quad [6-13]$$

Note: non-si units are used in this figure

$$\rho_l = 470 - \rho_v + 493,76 \left(1 - \frac{T}{T_c} \right) \quad [6-14]$$

Note: non-si units are used in this figure

$$\left[p + \frac{21760 \rho_v^2}{T^{0,5} (1 + 0,00111 \rho_v)} \right] (1 - 0,00111 \rho_v) = 488,16 T \rho_v \quad [6-15]$$

Note: non-si units are used in this figure

$$\mu_l = 10^{-4} \exp \left[\frac{-19,163 + \frac{12461}{T}}{\frac{2,6412 \times 10^6}{T^2} + \frac{2,0062 \times 10^8}{T^3}} \right] , \quad 204 < T < 405 \quad [6-16]$$

Note: non-si units are used in this figure

$$\mu_v = \frac{1,1989 \times 10^{-6} T^{3/2}}{306 + T} , \quad 195 < T < 405 \quad [6-17]$$

Note: non-si units are used in this figure

$$k_l = 0,547 \begin{bmatrix} 1 + 1,1296 \times 10^{-3} (T - 223,2) \\ - 2,6317 \times 10^{-5} (T - 223,2)^2 \end{bmatrix} , \quad 223 < T < 373 \quad [6-18]$$

Note: non-si units are used in this figure

$$k_v = 3,6856 \times 10^{-2} \left(\frac{T}{T_c} \right)^{1,3356} , \quad 223 < T < 400 \quad [6-19]$$

Note: non-si units are used in this figure

$$\sigma = 0,1449 \left(1 - \frac{T}{T_c} \right)^{1,4414} , \quad 244 < T < 405 \quad [6-20]$$

Note: non-si units are used in this figure

Sources of Data.

VARIABLE	REFERENCES
p _{sat}	Weast (1976) [95].
h _{fg}	Raznjevic (1970) [69].
ρ _l	Scallon & Carpitella (1970) [83].
ρ _v	
μ _l	
μ _v	
k _l	
k _v	
σ	Scallon & Carpitella (1970) [83], Weast (1976) [95].

FLUID: ETHANOL

$$T_b = 351,5 \text{ K}$$

$$p_c = 6,178 \times 10^6 \text{ Pa}$$

CHEMICAL SYMBOL: C₂H₆O

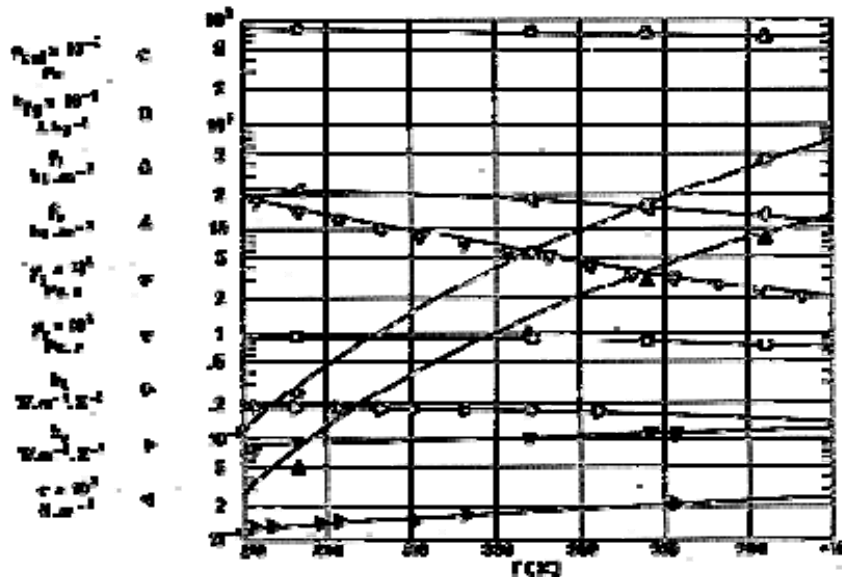
$$T_c = 516,2 \text{ K}$$

$$\rho_c = 280 \text{ kg.m}^{-3}$$

MOLAR MASS: 46,07

$$T_f = 158,7 \text{ K}$$

$$\rho_b = 735 \text{ kg.m}^{-3}$$



Note: non-si units are used in this figure

Figure 6-2: Relevant physical properties of Ethanol as a function of temperature, T , The labels correspond to experimental points. The expressions used to calculate the tabulated values are given below. Calculated by the compiler.

Formulae Used for Calculating the Values of the Physical Properties.

$$\log \frac{p_{sat}}{p_c} = -\frac{1,9642}{T/T_c} \left[1 - \left(\frac{T}{T_c} \right)^2 + 0,6896 \left(1 - \frac{T}{T_c} \right)^3 \left(3 + \frac{T}{T_c} \right) \right] \quad [6-21]$$

Note: non-si units are used in this figure

$$h_{fg} = 1,1987 \times 10^6 \left(1 - \frac{T}{T_c} \right)^{0,3218}$$

$$\rho_l = 560 - \rho_v + 548,43 \left(1 - \frac{T}{T_c} \right), \quad 283 < T < 516 \quad [6-22]$$

Note: non-si units are used in this figure

$$\left[p + \frac{9694\rho_v^2}{T^{0.5}(1+0,000928\rho_v)} \right] (1 - 0,000928\rho_v) = 180,47T\rho_v \quad [6-23]$$

Note: non-si units are used in this figure

$$\mu_l = 10^{-4} \exp \left[\begin{array}{l} -6,7461 + \frac{4276,4}{T} - \\ -\frac{6,0983 \times 10^5}{T^2} + \frac{4,4784 \times 10^7}{T^3} \end{array} \right], \quad 173 < T < 423$$

$$\mu_v = \frac{8,6287 \times 10^{-7} T^{3/2}}{188 + T}, \quad 263 < T < 473 \quad [6-24]$$

$$k_l = 0,185 \left[\begin{array}{l} 1 + 2,5253 \times 10^{-4} (T - 272) - \\ -1,4539 \times 10^{-6} (T - 272)^2 \end{array} \right], \quad 273 < T < 355$$

Note: non-si units are used in this figure

$$k_v = 3,5592 \times 10^{-2} \left(\frac{T}{T_c} \right)^{1,5837}, \quad 266 < T < 348$$

$$\sigma = 0,0468 \left(1 - \frac{T}{T_c} \right)^{0,8612}, \quad 283 < T < 516 \quad [6-25]$$

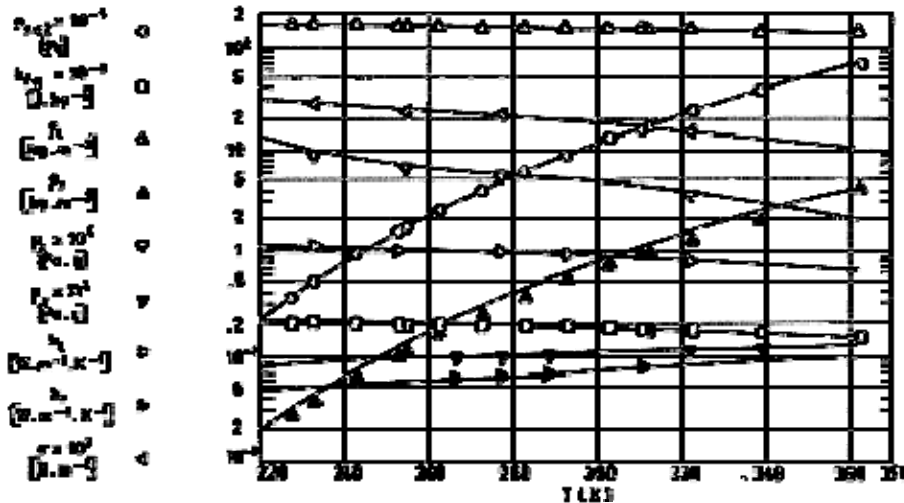
Sources of Data.

VARIABLE	REFERENCES
p_{sat}	Scallon & Carpitella (1970) [83].
h_{fg}	
ρ_l	
ρ_v	
μ_l	Raznjevic (1970) [69].
μ_v	Scallon & Carpitella (1970) [83].
k_l	
k_v	
σ	Scallon & Carpitella (1970) [83]; Weast (1976) [95].

FLUID: FREON 11

 $T_b = 296 \text{ K}$ $p_c = 4,374 \times 10^6 \text{ Pa}$ CHEMICAL SYMBOL: CF Cl₃ $T_c = 471,2 \text{ K}$ $\rho_e = 555 \text{ kg.m}^{-3}$

MOLAR MASS: 137,38

 $T_f = 162,1 \text{ K}$ $\rho_b = 1479 \text{ kg.m}^{-3}$ 

Note: non-si units are used in this figure

Figure 6-3: Relevant physical properties of Freon 11 as a function of temperature, T . The labels correspond to experimental points. The expressions used to calculate the tabulated values are given below. Calculated by the compiler.

Formulae Used for Calculating the Values of the Physical Properties.

$$\log \frac{p_{sat}}{p_c} = -\frac{1,4825}{T/T_c} \left[1 - \left(\frac{T}{T_c} \right)^2 + 0,4701 \left(1 - \frac{T}{T_c} \right)^3 \left(3 + \frac{T}{T_c} \right) \right]$$

$$h_{fg} = 2,6414 \times 10^5 \left(1 - \frac{T}{T_c} \right)^{0,3744}, \quad 162 < T < 471$$

$$\rho_l = 1110 - \rho_v + 992,60 \left(1 - \frac{T}{T_c} \right)$$

$$\left[p + \frac{1430 \rho_v^2}{T^{0,5} (1 + 0,000468 \rho_v)} \right] \left(1 - 0,000468 \rho_v \right) = 60,52 T \rho_v$$

$$\mu_l = 10^{-4} \exp \left[-33,078 + \frac{26598}{T} - \frac{6,8953 \times 10^6}{T^2} + \frac{6,0975 \times 10^8}{T^3} \right], \quad 233 < T < 322$$

$$\mu_v = \frac{8,1254 \times 10^{-7} T^{3/2}}{92 + T}, \quad 266 < T < 338$$
[6-26]

$$k_l = 0,110 \left[1 - 2,6719 \times 10^{-3} (T - 233,2) - 4,1589 \times 10^{-6} (T - 233,2)^2 \right] , \quad 233 < T < 322$$

$$k_v = 1,4346 \times 10^{-2} \left(\frac{T}{T_c} \right)^{1,47522} , \quad 266 < T < 310$$

Note: non-si units are used in this figure

$$\sigma = 0,0628 \left(1 - \frac{T}{T_c} \right)^{1,2299} , \quad 233 < T < 471$$

[6-27]

Note: non-si units are used in this figure

Sources of Data.

VARIABLE	REFERENCES
p _{sat}	Raznjevic (1970) [69].
h _{fg}	Scallon & Carpitella (1970) [83].
ρ _l	
ρ _v	
μ _l	Scallon & Carpitella (1970) [83].
μ _v	
k _l	Norris et al (1970) [64]; Scallon & Carpitella (1970) [83].
k _v	Scallon & Carpitella (1970) [83].
σ	

FLUID: METHANOL

T_b = 337,5 K

p_c = 9,709x10⁶ Pa

CHEMICAL SYMBOL: CH₃O

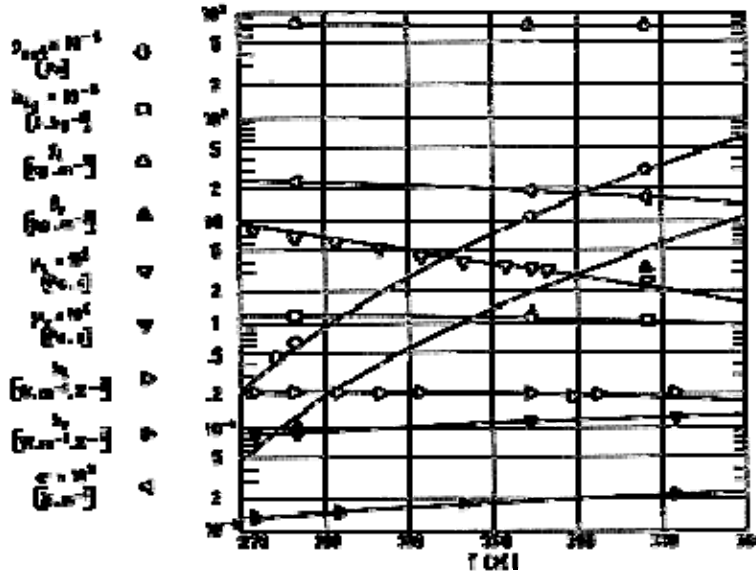
T_c = 513,2 K

ρ_c = 358 kg.m⁻³

MOLAR MASS: 32,04

T_f = 175,2 K

ρ_{lb} = 753,9 kg.m⁻³



Note: non-si units are used in this figure

Figure 6-4: Formulae Used for Calculating the Values of the Physical Properties.

$$\log \frac{p_{sat}}{p_c} = -\frac{1,8132}{T/T_c} \left[1 - \left(\frac{T}{T_c} \right)^2 + 1,6960 \left(1 - \frac{T}{T_c} \right)^3 \left(3 + \frac{T}{T_c} \right) \right] \quad [6-28]$$

Note: non-si units are used in this figure

$$h_{fg} = 1,6028 \times 10^6 \left(1 - \frac{T}{T_c} \right)^{0,3623}, \quad 283 < T < 513 \quad [6-29]$$

Note: non-si units are used in this figure

$$\rho_l = 716 - \rho_v + 110,82 \left(1 - \frac{T}{T_c} \right) \quad [6-30]$$

Note: non-si units are used in this figure

$$\left[p + \frac{10807 \rho_v^2}{T^{0,5} (1 + 0,000726 \rho_v)} \right] (1 - 0,000726 \rho_v) = 259,50 T \rho_v \quad [6-31]$$

Note: non-si units are used in this figure

$$\mu_l = 10^{-4} \exp \left[-14,917 + \frac{10840}{T} - \frac{2,3992 \times 10^6}{T^2} + \frac{1,9493 \times 10^8}{T^3} \right], \quad 173 < T < 422 \quad [6-32]$$

$$\mu_v = \frac{1,1961 \times 10^{-6} T^{3/2}}{329 + T}, \quad 273 < T < 473$$

$$k_l = 0,213 \left[1 - 5,2339 \times 10^{-4} (T - 272) - 1,6473 \times 10^{-5} (T - 272)^2 \right], \quad 272 < T < 373$$

Note: non-si units are used in this figure

$$k_v = 3,4511 \times 10^{-2} \left(\frac{T}{T_c} \right)^{1,4068}, \quad 273 < T < 373 \quad [6-33]$$

Note: non-si units are used in this figure

$$\sigma = 0,0453 \left(1 - \frac{T}{T_c} \right)^{0,8137}, \quad 283 < T < 513 \quad [6-34]$$

Note: non-si units are used in this figure

Sources of Data.

VARIABLE	REFERENCES
p _{sat}	Scallon & Carpitella (1970) [83].
h _{fg}	
ρ _l	
ρ _v	
μ _l	Raznjevic (1970) [69]; Scallon & Carpitella (1970) [83].
μ _v	
k _l	
k _v	
σ	Scallon & Carpitella (1970) [83].

FLUID: NITROGEN

T_b = 77,35 K

p_c = 3,393x10⁶ Pa

CHEMICAL SYMBOL: N₂

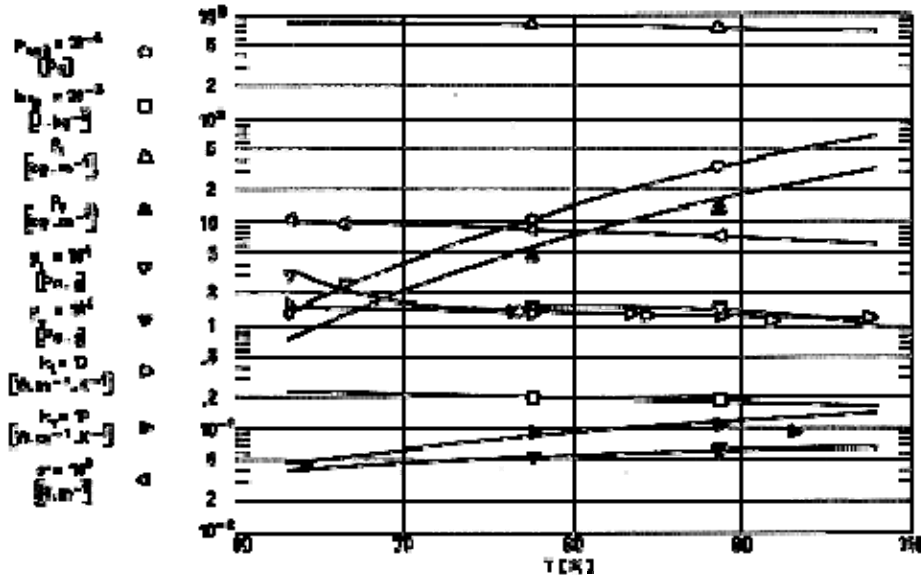
T_c = 126,05 K

ρ_c = 311 kg.m⁻³

MOLAR MASS: 28,016

T_f = 63,15 K

ρ_b = 810 kg.m⁻³



Note: non-si units are used in this figure

Figure 6-5: Relevant physical properties of Nitrogen as a function of temperature, T , The labels correspond to experimental points. The expressions used to calculate the tabulated values are given below. Calculated by the compiler.

Formulae Used for Calculating the Values of the Physical Properties.

$$\log \frac{p_{sat}}{p_c} = -\frac{1,3253}{T/T_c} \left[1 - \left(\frac{T}{T_c} \right)^2 + 0,3964 \left(1 - \frac{T}{T_c} \right)^3 \left(3 + \frac{T}{T_c} \right) \right] \quad [6-35]$$

Note: non-si units are used in this figure

$$h_{fg} = 0,2880 \times 10^6 \left(1 - \frac{T}{T_c} \right)^{0,3770}, \quad 63 < T < 126 \quad [6-36]$$

Note: non-si units are used in this figure

$$\rho_l = 622 - \rho_v + 466,60 \left(1 - \frac{T}{T_c} \right) \quad [6-37]$$

Note: non-si units are used in this figure

$$\left[p + \frac{1732 \rho_v^2}{T^{0,5} (1 + 0,00206 \rho_v)} \right] (1 - 0,00206 \rho_v) = 296,77 T \rho_v \quad [6-38]$$

$$\mu_l = 10^{-4} \exp \left[-50,109 + \frac{11988}{T} - \frac{9,4863 \times 10^5}{T^2} + \frac{2,5033 \times 10^7}{T^3} \right], \quad 63 < T < 110$$

$$\mu_v = \frac{1,5540 \times 10^{-6} T^{3/2}}{130 + T} , \quad 66 < T < 126$$

$$k_l = 0,158 \left[\begin{array}{l} 1 - 1,2470 \times 10^{-2} (T - 63,3) - 2,7138 \times 10^{-4} (T - 63,3)^2 \\ - 4,2004 \times 10^{-6} (T - 63,3)^3 \end{array} \right] , \quad 63 < T < 110$$

Note: non-si units are used in this figure

$$k_v = 2,8865 \times 10^{-2} \left(\frac{T}{T_c} \right)^{2,5793} , \quad 77 < T < 122 \quad [6-39]$$

Note: non-si units are used in this figure

$$\sigma = 0,0154 \left(1 - \frac{T}{T_c} \right)^{0,6124} , \quad 63 < T < 126 \quad [6-40]$$

Note: non-si units are used in this figure

Sources of Data.

VARIABLE	REFERENCES
p _{sat}	Scallon & Carpitella (1970) [83].
h _{fg}	
ρ _l	
ρ _v	
μ _l	
μ _v	Raznjevic (1970) [69]; Scallon & Carpitella (1970) [83].
k _l	Scallon & Carpitella (1970) [83].
k _v	Raznjevic (1970) [69]; Scallon & Carpitella (1970) [83].
σ	Scallon & Carpitella (1970) [83].

FLUID: PROPANE

$$T_b = 230,7 \text{ K}$$

$$p_c = 4,256 \times 10^6 \text{ Pa}$$

CHEMICAL SYMBOL: C₃H₈

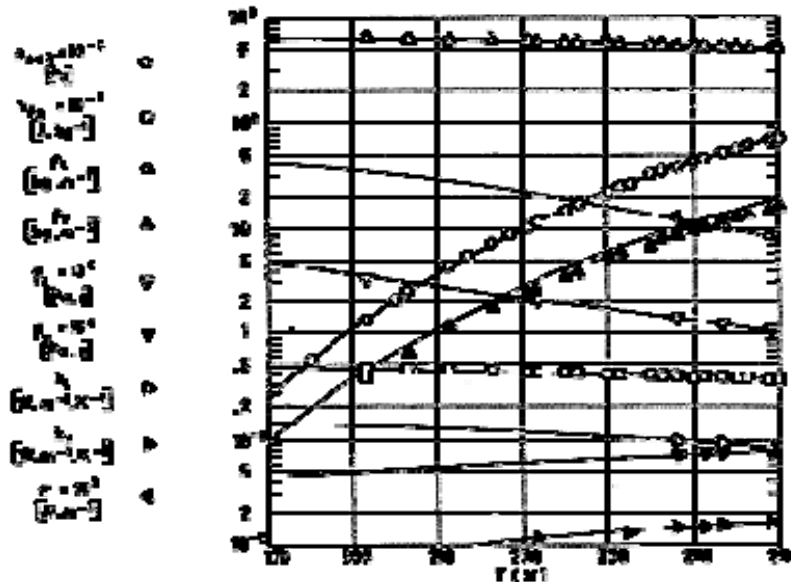
$$T_c = 370 \text{ K}$$

$$\rho_c = 226 \text{ kg.m}^{-3}$$

MOLAR MASS: 44,09

$$T_f = 83,3 \text{ K}$$

$$\rho_{lb} = 581,8 \text{ kg.m}^{-3}$$



Note: non-si units are used in this figure

**Figure 6-6: Relevant physical properties of Propane as a function of temperature, T ,
The labels correspond to experimental points. The expressions used to calculate
the tabulated values are given below. Calculated by the compiler.**

Formulae Used for Calculating the Values of the Physical Properties.

$$\log \frac{p_{sat}}{p_c} = -\frac{1,4473}{T/T_c} \left[1 - \left(\frac{T}{T_c} \right)^2 + 0,4535 \left(1 - \frac{T}{T_c} \right)^3 \left(3 + \frac{T}{T_c} \right) \right]$$

$$h_{fg} = 0,6422 \times 10^6 \left(1 - \frac{T}{T_c} \right)^{0,4023}, \quad 144 < T < 370$$

$$\rho_l = 452 - \rho_v + 344,64 \left(1 - \frac{T}{T_c} \right) \quad [6-41]$$

$$\left[p + \frac{7617 \rho_v^2}{T^{0,5} (1 + 0,00115 \rho_v)} \right] (1 - 0,00115 \rho_v) = 188,58 T \rho_v$$

Note: non-si units are used in this figure

$$\mu_l = 10^{-4} \exp \left[-4,9633 + \frac{2127,5}{T} - \frac{2,3239 \times 10^5}{T^2} + \right. \\ \left. + \frac{1,0312 \times 10^7}{T^3} \right], \quad 83 < T < 333 \quad [6-42]$$

Note: non-si units are used in this figure

$$\mu_v = \frac{9,5069 \times 10^{-7} T^{3/2}}{301 + T} , \quad 266 < T < 373 \quad [6-43]$$

Note: non-si units are used in this figure

$$k_l = 0,091 \left[1 - 4,9490 \times 10^{-3} (T - 266,5) \right] , \quad 266 < T < 333 \quad [6-44]$$

Note: non-si units are used in this figure

$$k_v = 2,5703 \times 10^{-2} \left(\frac{T}{T_c} \right)^{1,7045} , \quad 233 < T < 373 \quad [6-45]$$

Note: non-si units are used in this figure

$$\sigma = 0,1265 \left(1 - \frac{T}{T_c} \right)^{1,7733} , \quad 266 < T < 370 \quad [6-46]$$

Note: non-si units are used in this figure

Sources of Data.

VARIABLE	REFERENCES
p _{sat}	Raznjevic (1970) [69]; Weast (1976) [95]; Scallon & Carpitella (1970) [83]; Das & Eubank (1973) [19].
h _{fg}	Raznjevic (1970) [69]; Scallon & Carpitella (1970) [83]; Das & Eubank (1973) [19].
ρ _l	
ρ _v	
μ _l	Reid & Serwood (1966) [70]; Scallon & Carpitella (1970) [83].
μ _v	Reid & Serwood (1966) [70]; Raznjevic (1970) [69]; Scallon & Carpitella (1970) [83].
k _l	Scallon & Carpitella (1970) [83].
k _v	Raznjevic (1970) [69]; Scallon & Carpitella (1970) [83].
σ	Scallon & Carpitella (1970) [83].

FLUID: WATER (Saturated)

T_b = 373,2 K

p_c = 2,212 x10⁷ Pa

CHEMICAL SYMBOL: H₂O

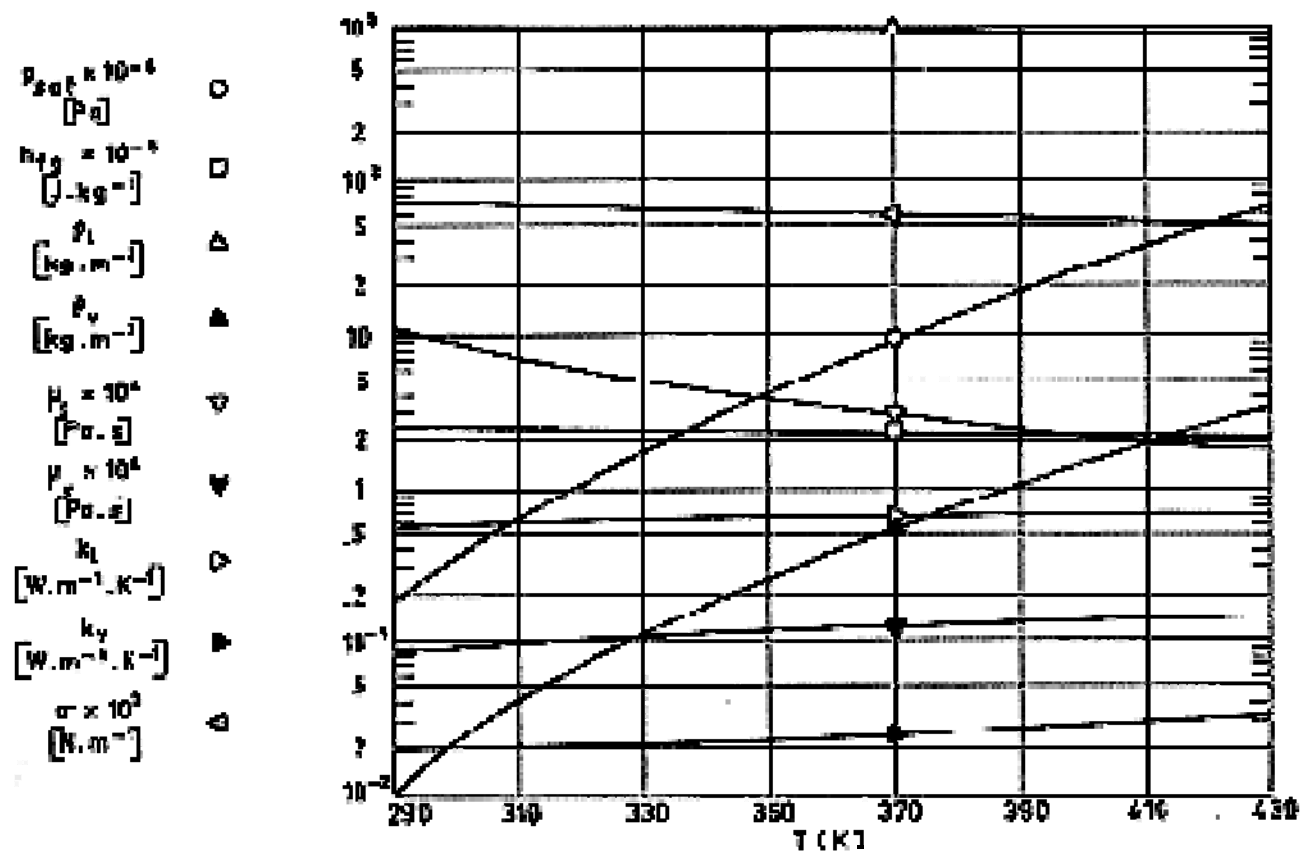
T_c = 647,3 K

ρ_c = 315,5 kg.m⁻³

MOLAR MASS: 18,015

T_f = 273,2 K

ρ_{lb} = 942,9 kg.m⁻³



Note: non-si units are used in this figure

Figure 6-7: Relevant physical properties of Water as a function of temperature, T , The labels have been drawn to guide in the selection of the appropriate curve, and do not correspond to experimental values. After Schmidt (1969) [82].

The table below presents the experimental data used to draw the curves of Figure 6-7.

T [K]	Vapour pressure, $p_{sat} \times 10^{-4}$ [Pa]	Ht. Of Vapor., $h_f \times 10^{-6}$ [J.kg ⁻¹]	Density, ρ [kg.m ⁻³]		Viscosity, $\mu \times 10^4$ [Pa.s]		Thermal Conductivity, k [W.m ^{-1.K⁻¹}]		Surface Tension, $\sigma \times 10^3$ [N.m ⁻¹]	Figure of Merit, $N \times 10^{-9}$ [W.m ⁻²]
			Liquid	Vapor	Liquid	Vapor	Liquid	Vapor		
290	0,19	2,53	998,8	0,01	10,82	0,087	0,598	0,0192	73,25	171,1
300	0,36	2,44	996,6	0,03	8,53	0,091	0,613	0,0198	71,72	204,5
310	0,63	2,41	993,3	0,04	6,92	0,095	0,628	0,0204	70,13	242,6
320	1,06	2,39	989,4	0,07	5,74	0,099	0,640	0,0210	68,47	282,1
330	1,73	2,37	984,6	0,11	4,86	0,103	0,651	0,0217	66,74	323,1
340	2,73	2,34	979,3	0,18	4,18	0,107	0,659	0,0223	65,00	356,3
350	4,19	2,32	973,5	0,26	3,65	0,111	0,668	0,0230	63,15	390,8
360	6,25	2,29	967,1	0,38	3,23	0,115	0,674	0,0237	61,30	420,3
370	9,09	2,26	960,2	0,54	2,88	0,119	0,680	0,0246	59,42	447,7
380	12,94	2,24	952,9	0,75	2,60	0,123	0,683	0,0256	57,54	472,4
390	18,04	2,21	945,3	1,03	2,37	0,127	0,686	0,0266	55,65	490,5
400	24,68	2,18	937,1	1,38	2,17	0,131	0,688	0,0278	53,77	506,2
410	33,17	2,15	928,5	1,82	2,00	0,135	0,688	0,0291	51,90	518,0
420	43,89	2,12	919,5	2,36	1,85	0,139	0,687	0,0304	50,07	527,6
430	57,23	2,09	910,2	3,03	1,73	0,143	0,685	0,0319	48,27	530,8

The figures of merit of all those liquids whose physical properties have been tabulated are given in Figure 6-8.

Each one of the curves plotted in this figure is limited between reasonable bounds imposed by the limiting values of the heat pipe working pressure. The upper limit, purely structural, is approximately 50×10^4 Pa, while the lower limit is either $0,3 \times 10^4$ Pa, or the saturation pressure of the working fluid at freezing point, whichever is larger.

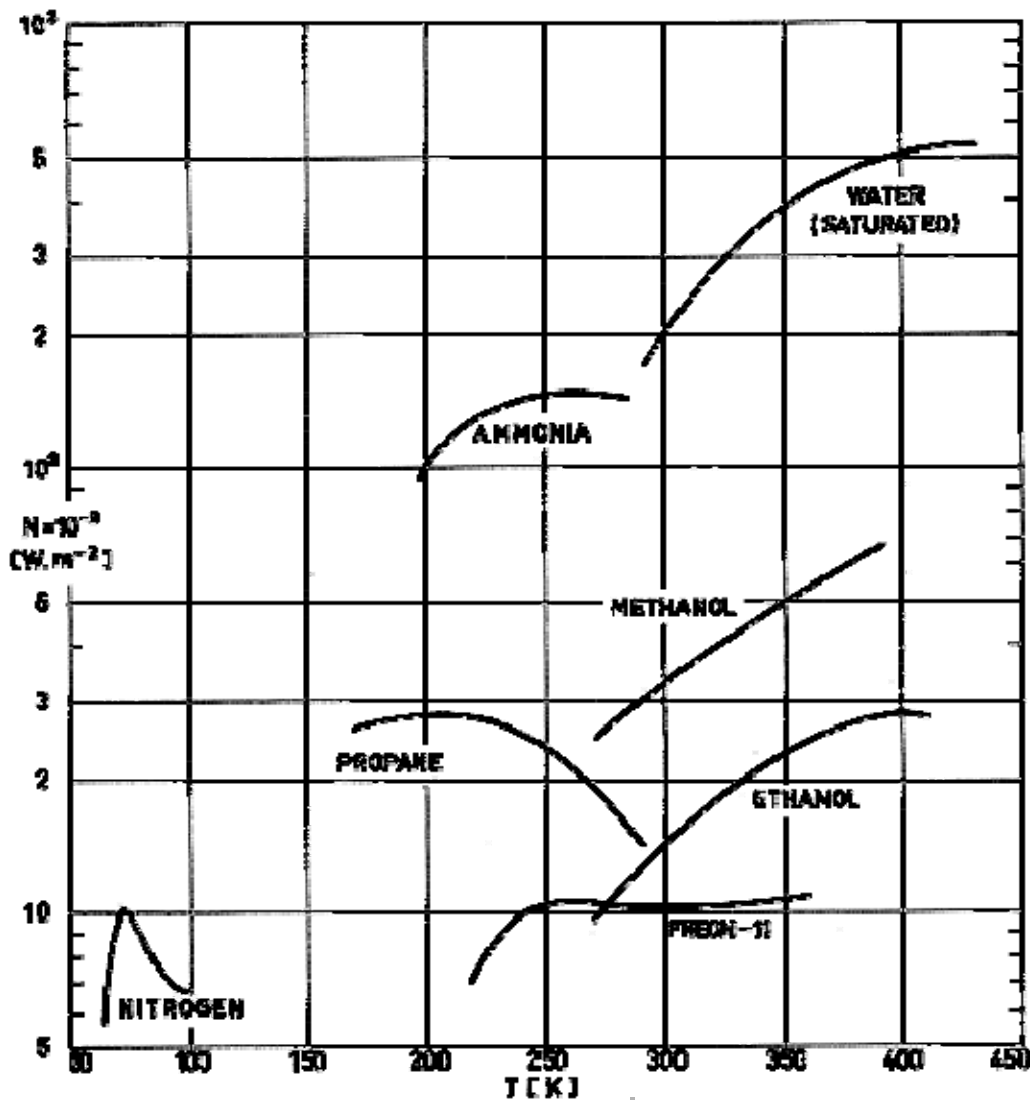


Figure 6-8: Figure of Merit, N , as a function of temperature, T , for several heat pipe working fluids. For each curve, the range of temperature variation is bounded between the largest and smallest operating pressures. Calculated by the compiler.

6.4 Compatibility with wicks

The choice of suitable materials for constructing heat pipes is dictated by the compatibility between the different components. In general, improper choice of components results in a gradual appearance of non-condensable gasses. The danger of corrosion and dissolution of the wick structure under high temperature conditions should not be overlooked.

The following table reports some information on the chemical compatibility between typical wick materials and working fluids.

Table 6-1: Chemical Compatibility between Typical Wick Materials and Working Fluids.

Working Fluid	Wick Material				
	Aluminium	Copper	Nickel	Refrasil	Stainless Steel
Acetone	RL	RU	PC	RU	PC
Ammonia	RU	NR	RU	RU	RU
Ethanol	NR				
Freon 11	RU				
Methanol	NR	RU	RL	RU	GNT
Nitrogen	RL				RL
Propane					
Water	GNC	RU	PC	RU	GNT
Explanation:	RU = Recommended by past successful use. RL = Recommended by literature. PC = Probably compatible. NR = Not recommended. GNC = Generation of non-condensable gas at all temperatures. GNT = Generation of non-condensable gas at elevated temperatures, when oxide is present.				

NOTE After Basiulis & Filler (1972) [3], Winter & Barsch (1971) [96].

7

Simple heat pipe

7.1 General

Heat is transferred along a heat pipe by continuous mass transfer and phase changing of suitable working fluid. The pumping back of the fluid, once condensed, is achieved by capillary action in the wick. These processes depend exclusively on the surrounding temperature field and, provided that the heat flow rate is kept below limits, there is, in principle, no possibility of controlling the heat pipe performance once the heat flow is fixed.

Heat pipes whose performance cannot be varied are called "simple heat pipes", whereas those devices in which some control of the evaporation, condensation or pumping phenomena can be achieved are called "variable conductance heat pipes".

7.2 Operating limits

Although the heat pipe exhibits a very high thermal conductance, the maximum heat transfer rate it can afford is limited. The operating limits are due either to a breakdown of the fluid flow or to any process that fixes a maximum value of the amount of fluid that can be forced through the tube by increasing the heat transfer.

These operating limits are discussed extensively in the following. Their main features are summarized in the following table.

LIMIT	EFFECT OF INCREASED HEAT FLOW
Capillary	The liquid evaporates faster than it can be supplied by capillary pumping to the evaporator.
Sonic	The vapour density decreases and simultaneously the vapour velocity increases due to heat addition until the velocity equals the sound velocity, and the flow in the tube is "choked".
Entrainment	The vapour stream shears-off droplets from the liquid-vapour interface, carrying them into the condenser.
Boiling	The liquid in the wick boils-off and a "vapour blanket" appears in the capillary structure.

7.2.1 Capillary heat transfer limit

Fluid circulation in a heat pipe is maintained by capillary forces developed in the wick structure at the liquid-vapor interface. These forces balance the pressure losses due to the flow in both the liquid and vapor phases. The capillary heat transfer limit will be reached when a given heat flux causes the liquid in the wick to evaporate faster than it can be supplied by capillary pumping. Under this condition drying and overheating of the wick will occur, until a "burnout" is reached which usually will result in the destruction of the pipe.

The limiting heat transfer rate can be predicted in several typical cases as it is indicated in the following clauses.

7.2.1.1 Mesh screen wick heat pipe

An expression for the capillary heat transfer limit in heat pipes using mesh screen wicks has been derived by Cotter (1965) [18].

For a heat pipe under steady state conditions in a gravitational field, Cotter equated the capillary pumping pressure with the sum of the liquid and vapor pressure drops plus the hydrostatic pressure.

$$\Delta p_c = \Delta p + \Delta p_v + \rho g l \sin\varphi.$$

1. The capillary pumping pressure has been introduced in clause 5.2.1

$$\Delta p_c = \frac{2\sigma \cos\theta}{r_c} \quad [7-1]$$

Note: non-si units are used in this figure

2. The liquid pressure drop in the wick can be expressed by use of Darcy's law for flow through porous media (Eq. 3.33, [ECSS-E-HB-31-01 Part 14, clause 7.4.2.4](#)) with a mean velocity

$$V = \frac{Q/h_{fg}}{\rho_l \frac{\pi}{4} (D_i^2 - D_v^2)} \quad [7-2]$$

Note: non-si units are used in this figure

as follows:

$$\Delta p_l = \frac{4\mu_l (Q \cdot l_{eff})}{\pi K h_{fg} \rho_l (D_i^2 - D_v^2)} \quad [7-3]$$

Note: non-si units are used in this figure

For the permeability, K , Cotter (1965) [18] suggests:

$$K = \frac{Q}{b} r_c^2 \quad [7-4]$$

Note: non-si units are used in this figure

where b is a dimensionless constant which depends on the geometry of the capillary structure. For non-connected parallel cylindrical pores, $b \approx 8$. For realistic capillary structures with tortuous and interconnected pores, $b \approx 10$ to 20.

3. The expression of the pressure drop in the vapor space is in general complex. When the vapor Reynolds number is small, viscous effects dominate and the Hagen-Poiseuille formula for the fully developed laminar flow in straight ducts ([ECSS-E-HB-31-01 Part 13, clause 7.2](#)), with $D = D_v$ and $l = l_{eff}$, can be used.

Now the mean velocity is

$$V = \frac{Q/h_{fg}}{\rho_v \frac{\pi}{4} D_v^2} \quad [7-5]$$

Note: non-si units are used in this figure

Hence,

$$\Delta p_v = \frac{128 \mu_v (Q \cdot l_{eff})}{\pi h_{fg} \rho_v D_v^2} \quad [7-6]$$

Note: non-si units are used in this figure

In the last expression ρ_v depends on p_v . l_{eff} is the heat pipe effective length which is the distance between mid points of evaporator and condenser.

Assuming that the heat pipe is operating under reduced gravity conditions, and that the vapor flow passage is much larger than the wick thickness, then

$$\Delta p_e \sim \Delta p_l,$$

and the equation for the maximum heat transfer rate, derived by Cotter, may be expressed as:

$$Q_{max} = N \frac{\pi}{2} \frac{K(D_i^2 - D_v^2)}{r_c l_{eff}} \quad [7-7]$$

Note: non-si units are used in this figure

In this expression N is the figure of merit of the working fluid, introduced in clause 6.1. Complete wetting ($\theta = 0$) has been assumed. The remaining variables in the right hand side of the above equation depend on the heat pipe design.

Values of the figure of merit, N , for several relevant fluids are given in Figure 6-8 (non cryogenic fluids) and Figure 10-2 (cryogenic fluids).

The assumptions on which Cotter's formula is based are not generally valid. It is convenient to write down the complete equation for the fluid flow pressure drop as follows:

$$1 - \frac{l \sin \varphi}{H} = \frac{Q}{Q_{\max}} \left[1 + 32K \frac{D_i^2 - D_v^2}{D_v^4} \frac{\mu_v \rho_l}{\mu_l \rho_v} \right] \quad [7-8]$$

Note: non-si units are used in this figure

where H is the equilibrium capillary height already quoted in clause 5.2.1, and Q_{\max} is the value of the maximum heat transfer rate.

Summarizing, the capillary heat transfer limit of a mesh screen wick heat pipe operating at room or high temperatures and under reduced gravity condition can be deduced from the above expression of Q_{\max} once the physical dimensions of the heat pipe and the working fluid are fixed. In other cases, as for cryogenic heat pipes, the situation is far more complicated as it will be discussed in clause 10.4.1.

7.2.1.2 Grooved heat pipe

Frank et al. (1967) [27] developed a theory to predict the capillary heat transfer limit for a grooved heat pipe. They assume Poiseuille flow for the liquid and use a modified Poiseuille pressure drop-flow rate relationship for the vapor:

$$\Delta p_v = F 8 \mu_{v,eff} m_v / \pi \rho_v r_v$$

The following variables are defined in connection with the above equation and with Figure 7-1 to Figure 7-5.

$$r_m = r_w - \delta/2 = r_v + \delta/2$$

$$\beta = (w+w')/w; \alpha = \delta/w; \psi = \delta/2r_m; \Gamma = \pi N/\beta l_{eff}$$

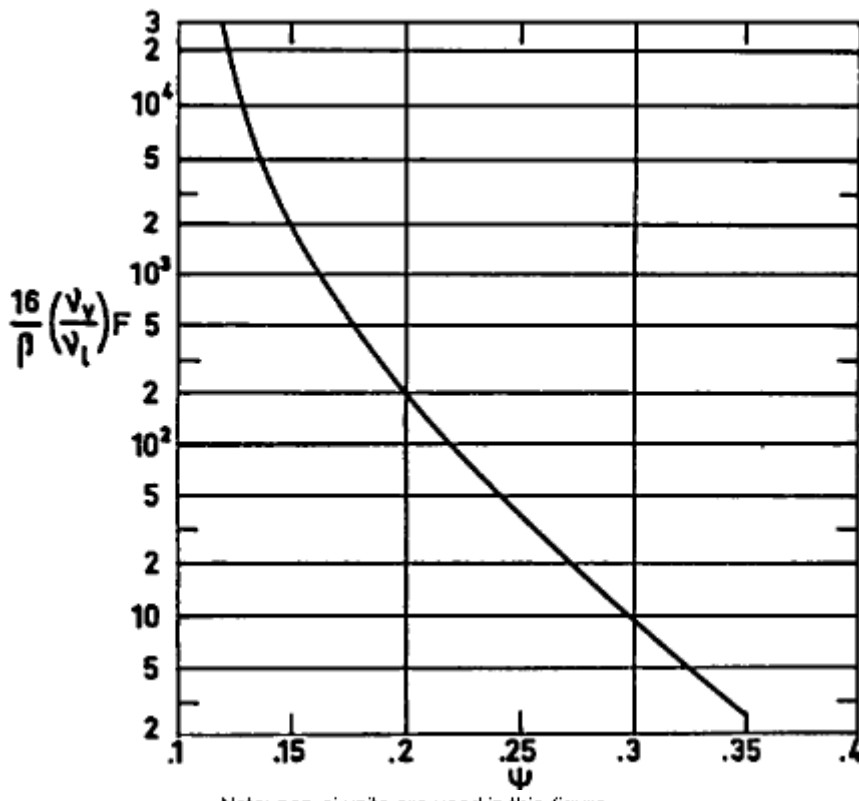
$F = 1$, when $Re \leq 2200$, Laminar Flow

$F = 0,00494 Re^{3/4}$, when $Re > 2200$, Turbulent Flow

Finally, l_{eff} has been already defined, and Re is the Reynolds number based on the inner diameter, D_i , of the tube.

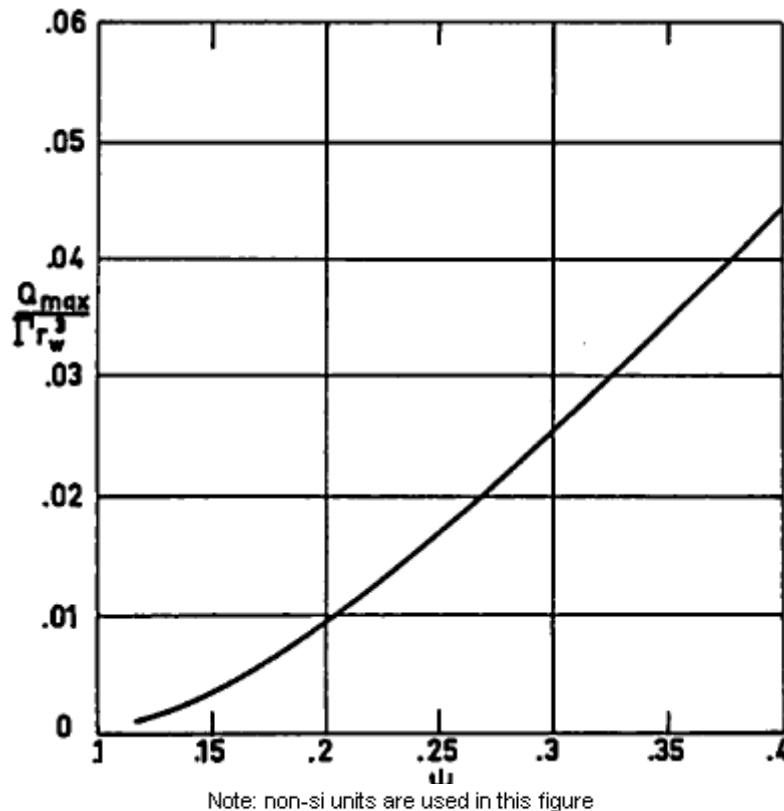


Figure 7-1: Sketch illustrating design variables in grooved heat pipes. From Frank et al. (1967) [27], quoted by Winter & Barsch (1971) [96].



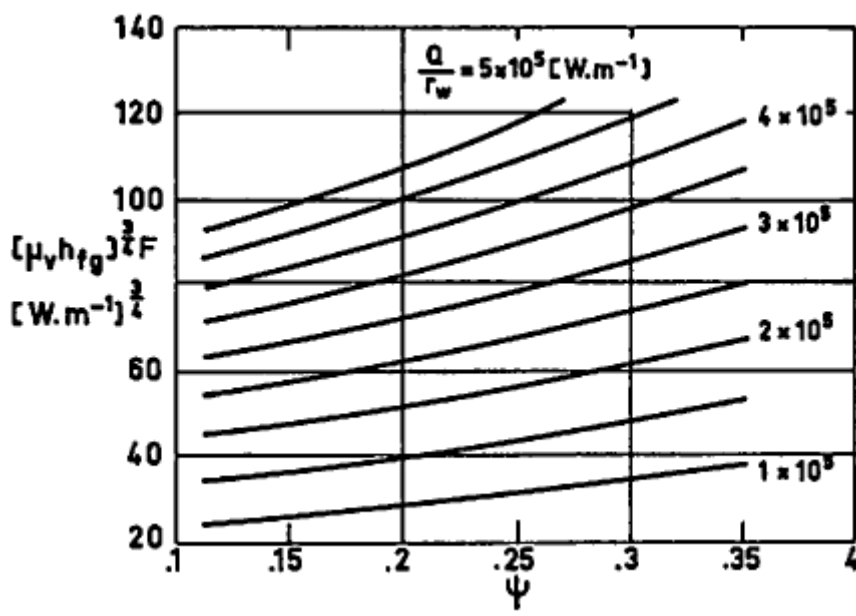
Note: non-si units are used in this figure

Figure 7-2: Relation between the dimensionless parameter $16/\beta(v_v/v_l)F$ and the geometrical parameter, ψ . From Frank et al. (1967) [27], quoted by Winter & Barsch (1971) [96].



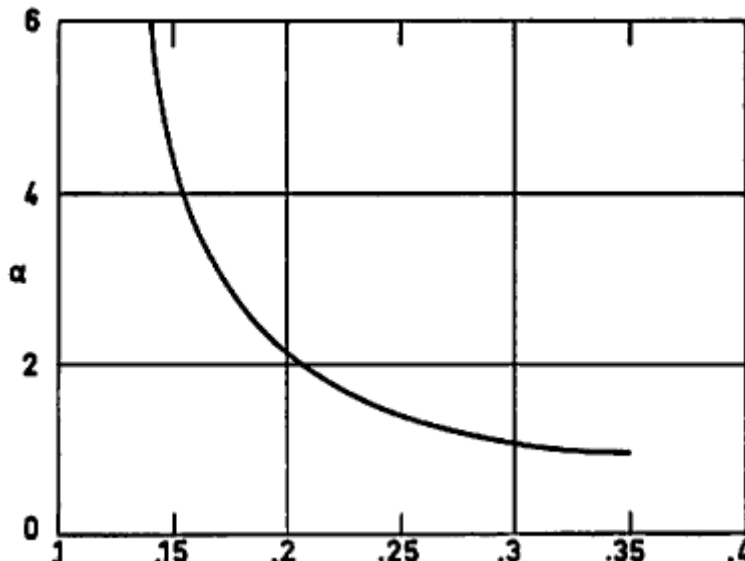
Note: non-si units are used in this figure

Figure 7-3: Optimum value of the dimensionless maximum heat transfer, Q_{max}/Tr_w^3 , vs. the geometrical parameter, ψ . From Frank et al. (1967) [27], quoted by Winter & Barsch (1971) [96].



Note: non-si units are used in this figure

Figure 7-4: Graph for determining F . From Frank et al. (1967) [27], quoted by Winter & Barsch (1971) [96].



Note: non-si units are used in this figure

Figure 7-5: Optimum value of the aspect ratio of the grooves, α , vs. the geometrical parameter, ψ . From Frank et al. (1967) [27], quoted by Winter & Barsch (1971) [96].

Frank's results are given in Figure 7-2 to Figure 7-5, which can be used for optimizing a grooved heat pipe, that is to say, for designing the heat pipe whose capillary limit is just above the heat flow rate which is intended to be transferred.

The procedure for optimizing the heat transfer ratio, $Q_{max}/\Gamma r_w^3$, is the following:

1. The operating temperature, the working fluid, the effective flow length, l_{eff} , and the pitch, β , are assumed to be known beforehand. In particular, the pitch has a minimum value of unity, and it is advisable to make it as small as possible. In general, the minimum pitch value is imposed by manufacture and strength requirements.
2. Assuming that $F = 1$, the geometric parameter ψ may be found in Figure 7-2.
3. The optimum value of $Q_{max}/\Gamma r_w^3$ is taken from Figure 7-3.
4. A new value of F may be obtained from Figure 7-4. If $F \leq 1$, the vapor flow is laminar and no further iterations are required. If, on the other hand, $F > 1$, the vapor flow regime is turbulent and the procedure should be repeated using the new value of F to enter in Figure 7-2.
5. The optimum value of the geometrical ratio α can be found from Figure 7-5 once the iterative procedure has supplied the value of F .

7.2.2 Sonic limit (choking)

This limit is often encountered in liquid-metal heat pipes operating at low vapor pressure and, hence, low density.

When heat is added, the vapor velocity increases for two reasons: 1, the vapor mass flow rate increases due to enhanced evaporation. 2, Even assuming that the mass flow rate is constant, heat addition causes the Mach number to increase along the tube if the flow is subsonic and to decrease if it is supersonic (the Mach number is the flow velocity to sound speed ratio). The reader is referred to Shapiro (1954) [85] or Rotty (1962) [71] for details concerning this effect, which is known as "choking".

On the other hand, the sound speed, which for a given perfect gas depends only on the temperature, is not affected by the heat transfer, provided that the liquid and vapor phases coexist in the tube.

From the above reasoning it is deduced that the supersonic conditions can not be reached by mere heat addition in a gas flow initially at low velocity, and that the maximum heat transfer rate is attained when the fluid velocity at the evaporator exit reaches the local sonic velocity.

The existence of the sonic limit or the gas-dynamic choking phenomenon in heat pipes was first suggested and analyzed by Levy (1968) [50], who performed a one-dimensional compressible vapor flow analysis, by treating the vapor as perfect gas. Levy obtained the following expression of the heat transfer rate under choking conditions:

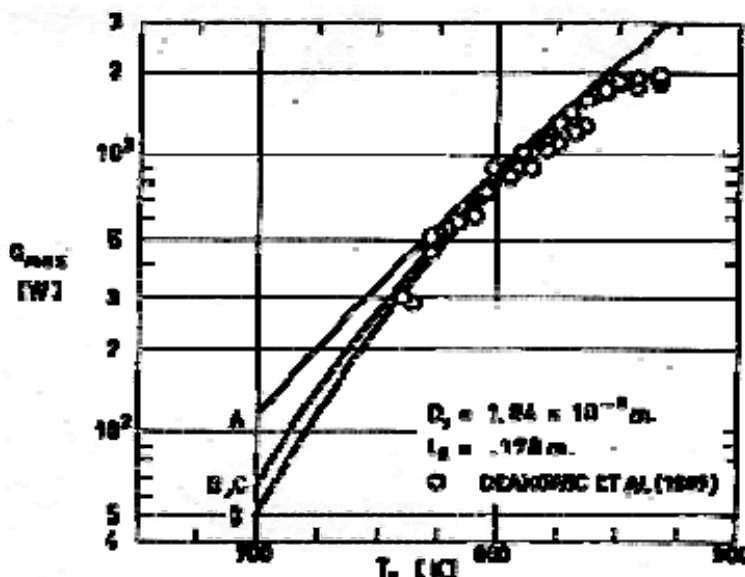
$$Q_{\max} = \frac{\pi \rho_v a h_{fg} D_v^2}{4[2(\gamma+1)]^{1/2}} \quad [7-9]$$

where:

a , velocity of sound at upstream end of the evaporator. [m.s⁻¹].

γ , vapor ratio of specific heats.

More recently Levy (1972) [49] has taken into account both the effects of the shear stress, τ , and the convective heat transfer, Q_{conv} , on the sonic limit. His results, summarized in the Figure 7-6, indicate that for a given value of the operating temperature, the shear stress will reduce the maximum rate of heat transfer based on the sonic limit to a value lower than it is expected from the frictionless analysis, and that this reduction can be quite large at the lower values of the operating temperature.



Note: non-si units are used in this figure

Figure 7-6: Maximum heat transfer, Q_{\max} , based on sonic limit, vs. evaporator temperature, T_E , for several values of the shear streets, τ , and of the convective heat transfer, Q_{conv} . Sodium heat pipe. A: $\tau=0$ and $Q_{conv}=0$; B: $\tau\neq 0$ and $Q_{conv}\neq 0$; C: $\tau\neq 0$ and $Q_{conv}=0$; D: $\tau\neq 0$ and $Q_{conv}\neq 0$. In this case the heat pipe had an adiabatic length. In curves A, B, and C choking is reached at the evaporator, while in curve D choking is reached at the adiabatic length end. From Levy (1972) [49].

7.2.3 Entrainment limit

The entrainment limit has its origin in the interfacial shear due to the flows of vapor and liquid in opposite directions. When the relative velocity between the vapor and liquid is sufficiently large, the interface becomes unstable, and liquid droplets are entrained in the vapor. This loss of liquid in the wick, which thus never reaches the evaporator, amounts to a certain reduction in the maximum evaporation heat transfer, and this lowered heat transfer rate defines the entrainment limit. The entrainment phenomenon is governed by the Weber number that compares the vapor inertial forces to the liquid surface tension forces. Because of the complexity introduced by the presence of the wick and the curved interface, the available quantitative information, either experimental or theoretical, concerning the entrainment limit is very scarce despite its undoubted relevance in heat pipe design.

The Weber number, We , is defined as:

$$We = (\rho_v V_v^2 l') / \sigma,$$

where l' is a characteristic length associated with the wick surface. In screen wicks, l' is very nearly equal to the wire diameter, and it probably depends to some extent on the wire spacing.

An estimate of the entrainment limited heat flux may be established introducing in the energy equation the assumption, $We = 1$, (Kemme (1969) [40]).

$$Q_{max} = (\rho_v \sigma / l')^{1/2} h_{fg} A_v$$

7.2.4 Boiling limit

This limit, which is associated with boiling within the wick, is difficult to predict since it requires a thorough knowledge of the cavity dimensions in the wick and of the effective thermal conductivity of the saturated wick, among other properties.

Neal (1967) [63] (quoted by Winter & Barsch (1971) [96]), taking into account the superheat required for the outset of nucleation in the wick, obtained the following expression for the boiling limit.

$$Q_{max} = \frac{2\pi l_E k_{eff}}{\ln \frac{D_i}{D_v}} \frac{\sigma T_{sat}}{\rho_v h_{fg}} \left[\frac{2}{r_b} - \frac{\cos \theta_E}{\pi \Phi D_v} \right] \quad [7-10]$$

Note: non-si units are used in this figure

where:

D_i , Inner diameter of the heat pipe. [m].

D_v , Diameter of the vapor space. [m].

T_{sat} , Saturation temperature. [K].

h_{fg} , Latent heat of vaporization. [J.kg⁻¹].

k_{eff} , Effective thermal conductivity of the wick. [W.m⁻¹.K⁻¹].

l_E , Evaporator length. [m].

r_b , Radius of the bubble nucleus. [m].

Φ , Wick porosity

ρ_v , Vapor density. [kg.m⁻³].

σ , Surface tension. [$\text{N} \cdot \text{m}^{-1}$].

θ_e , Wetting angle in the evaporator. [Angular Degrees].

7.3 Performance

This clause contains a compilation of performance curves of typical heat pipes, which has been prepared by Skrabek (1972) [88].

Several combinations of temperatures, working fluids, wicks, wick and container materials, and heat pipe diameter have been considered. Such combinations are indicated in the Table 7-1 below.

Table 7-1: Combinations of Temperatures, Working Fluids, Wick and Container Materials, and Heat Pipe Outer Diameters.

T [K]	Working Fluid	Container Material	Wick Material		Heat Pipe Diameter [m]
			Porous Slab	Circumferential Screen	
77	N_2	Al	SS	SS	$1,27 \times 10^{-2}$ $2,54 \times 10^{-2}$
273	NH_3	Al	SS	SS	
373	H_2O	Cu	Cu	Cu	

NOTE From Skrabek (1972) [88].

The performances have been calculated assuming a standard heat pipe 1,10 m long and with both evaporator and condenser lengths equal to 0,1 m. The walls are $0,89 \times 10^{-3}$ m thick, and the wick porosity is $\phi = 0,7$.

Since the effective transport length is $l_{eff} = 1$ m, Q_{max} and $(Q_{eff})_{max}$ have the same numerical value.

To perform the calculations it has been assumed that both the heat input and heat output were uniform.

Two types of performance curves are given for each one of the combinations of temperatures, wick types and heat pipe diameters.

One type, Figure 7-7 to Figure 7-12, gives the maximum heat transfer capability as a function of several wick parameters for a "zero g" environment. Also indicated on the curves is the range of wick thickness over which the vapor flow is laminar (solid lines). Within this range, the results can be expressed in terms of the Integral Heat Transport Factor, $(Q \cdot l_{eff})_{max}$, and are applicable to other heat pipe lengths. When the vapor flow is turbulent, (dotted part of the curves) the plotted, Q_{max} , is only applicable for the particular length of 1,1 m.

The other type of performance curves, Figure 7-13 to Figure 7-18, provides information about the heat pipe conductance. Unfortunately, conductance's are much less amenable to theoretical predictions than the heat transfer capability. The overall conductance was calculated from the reciprocal of the sum of five thermal resistances, namely: those corresponding to evaporator-wall, evaporator-wick, vapor temperature drop, condenser-wick, and condenser-wall.

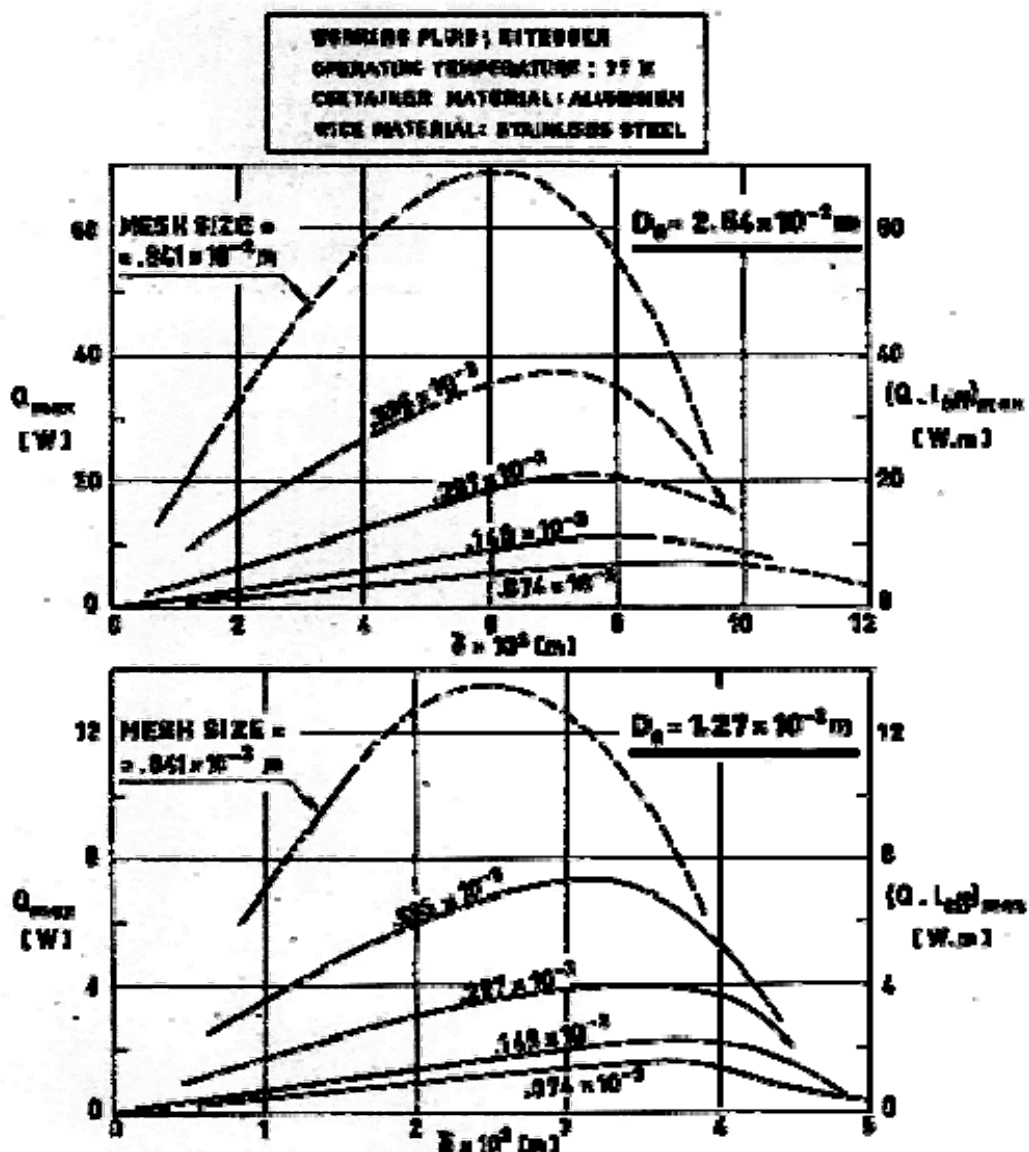
The greatest uncertainty exists for data on evaporator-wick and condenser-wick resistances. In the case of circumferential wicks, the conductance has been obtained from two values of the effective wick thermal conductivity corresponding to series and to parallel thermal conduction.

$$k_{eff(parallel)} = k_w[(1-\Phi) + \nu\Phi],$$

$$k_{eff(series)} = \nu k_w/[v + \Phi(1-v)].$$

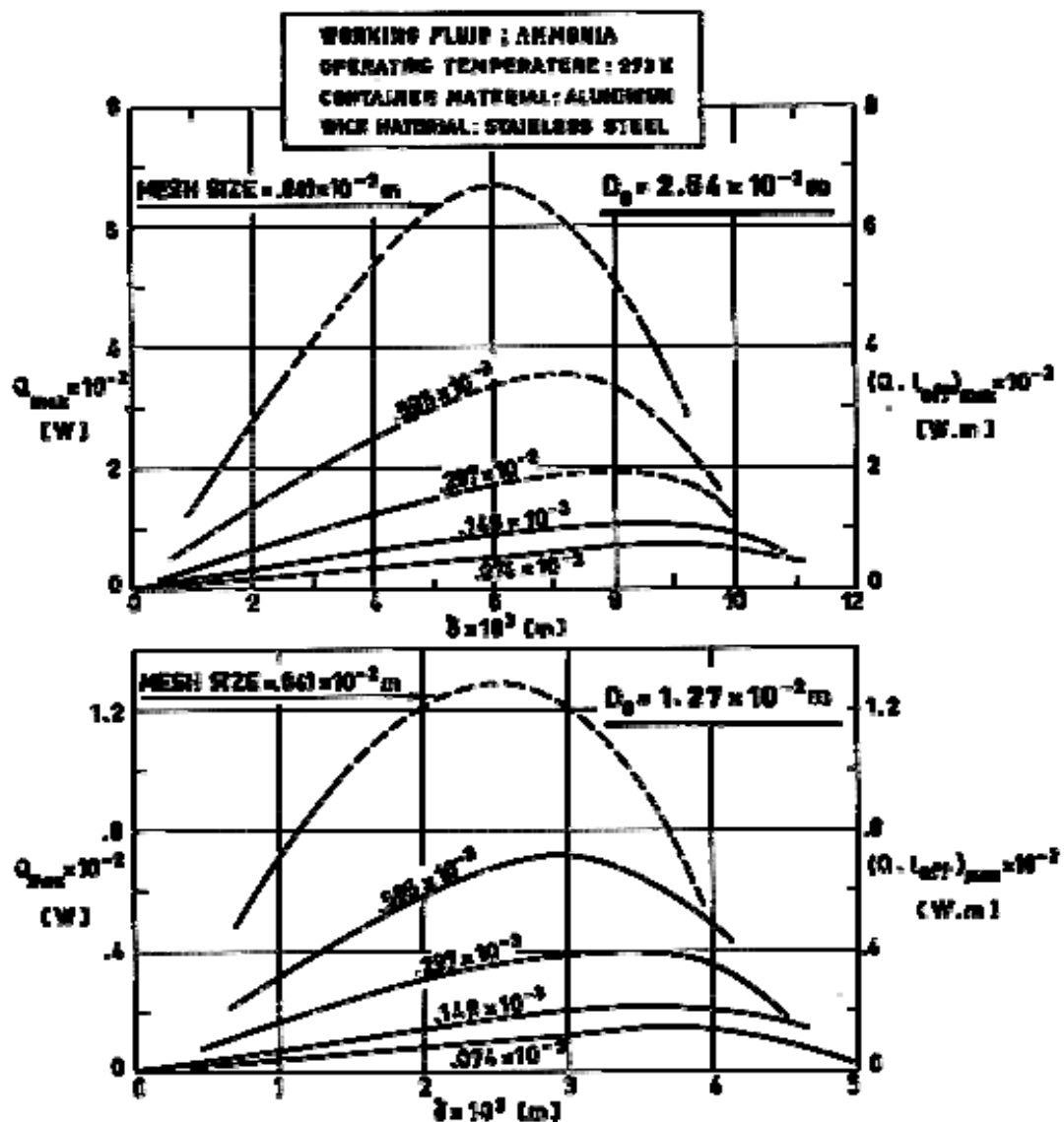
In the case of porous slab wicks, Figure 7-16 to Figure 7-18, the overall conductance is given for three different heat transfer coefficients, h , which are indicated on the respective curve.

For most wick designs, the temperature drops through the wall and through the wick are dominating, while the temperature drop through the vapor is small. The range for which the latter is less than 1% of the total temperature drop is indicated by a dotted line.



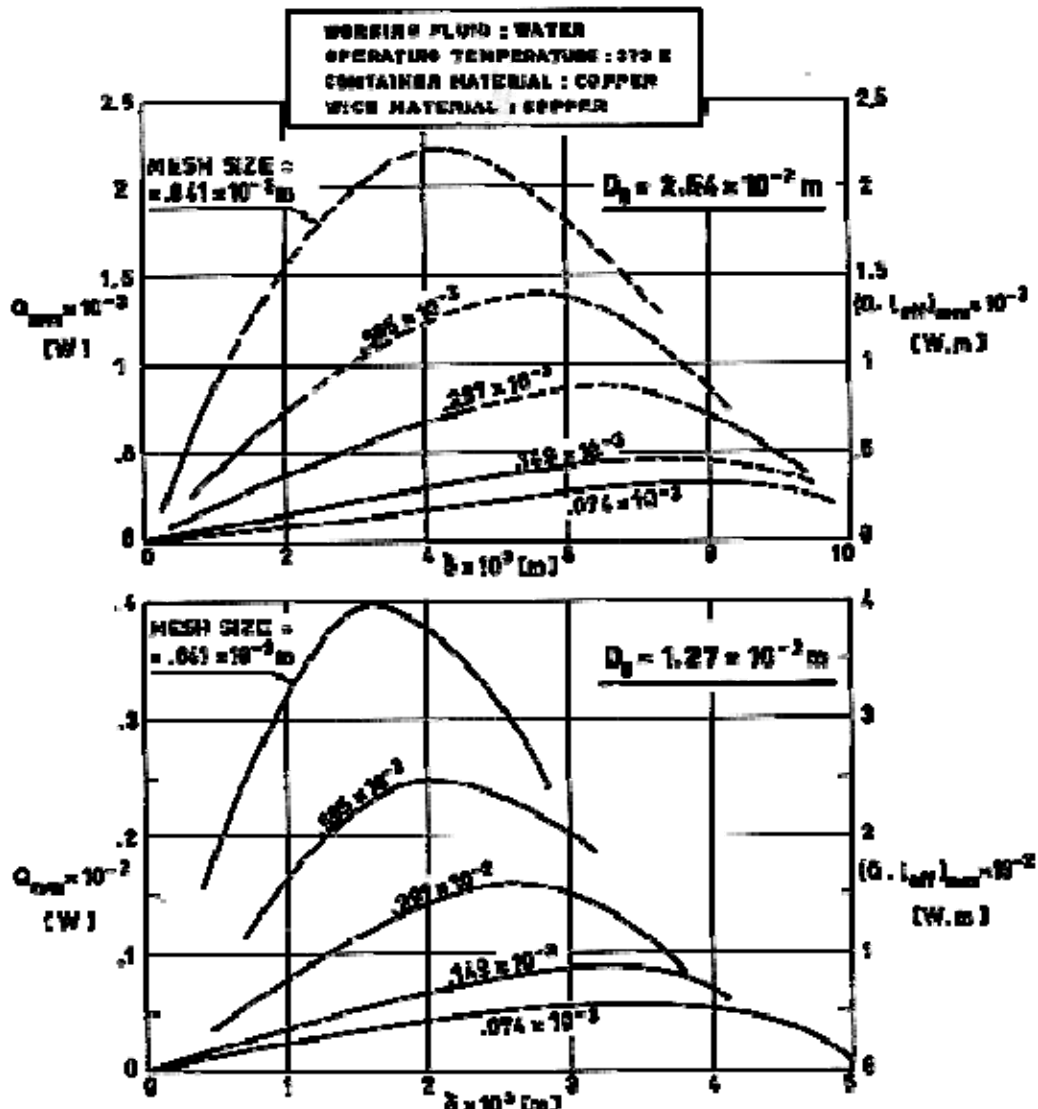
Note: non-si units are used in this figure

Figure 7-7: Heat Transfer, Q_{max} , and Integral Heat Transport Factor, $[Q.l_{eff}]_{max}$, vs. wick thickness, δ , for several mesh sizes and two heat pipe diameters, D_o . Circumferential screen wick. Solid lines: vapour laminar flow; dotted lines: vapour turbulent flow. From Skrabek (1972) [88].



Note: non-si units are used in this figure

Figure 7-8: Heat Transfer, Q_{max} , and Integral Heat Transport Factor, $[Q \cdot l_{eff}]_{max}$, vs. wick thickness, δ , for several mesh sizes and two heat pipe diameters, D_o . Circumferential screen wick. Solid lines: vapour laminar flow; dotted lines: vapour turbulent flow. From Skrabek (1972) [88].



Note: non-si units are used in this figure

Figure 7-9: Heat Transfer, Q_{max} , and Integral Heat Transport Factor, $[Q \cdot l_{eff}]_{max}$, vs. wick thickness, δ , for several mesh sizes and two heat pipe diameters, D_o . Circumferential screen wick. Solid lines: vapour laminar flow; dotted lines: vapour turbulent flow. From Skrabek (1972) [88].

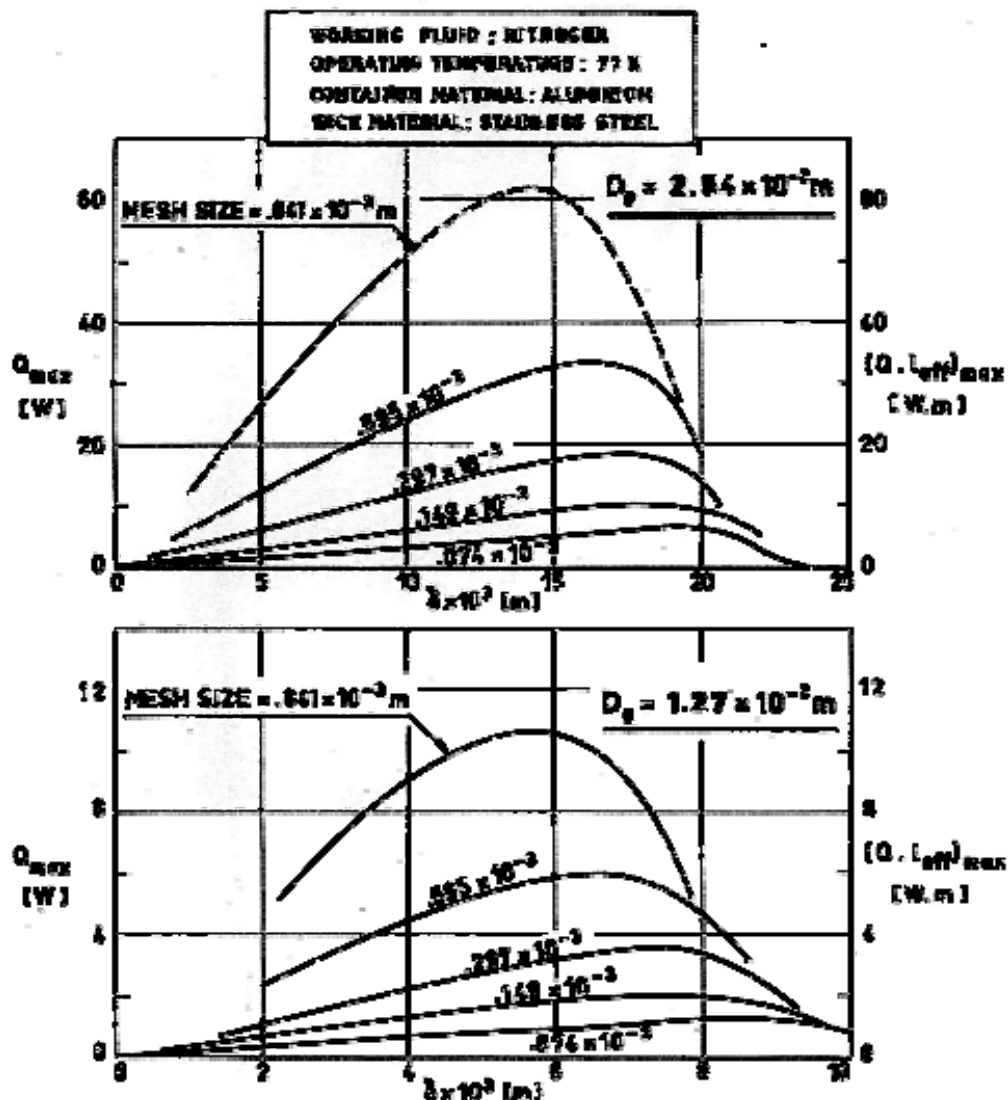
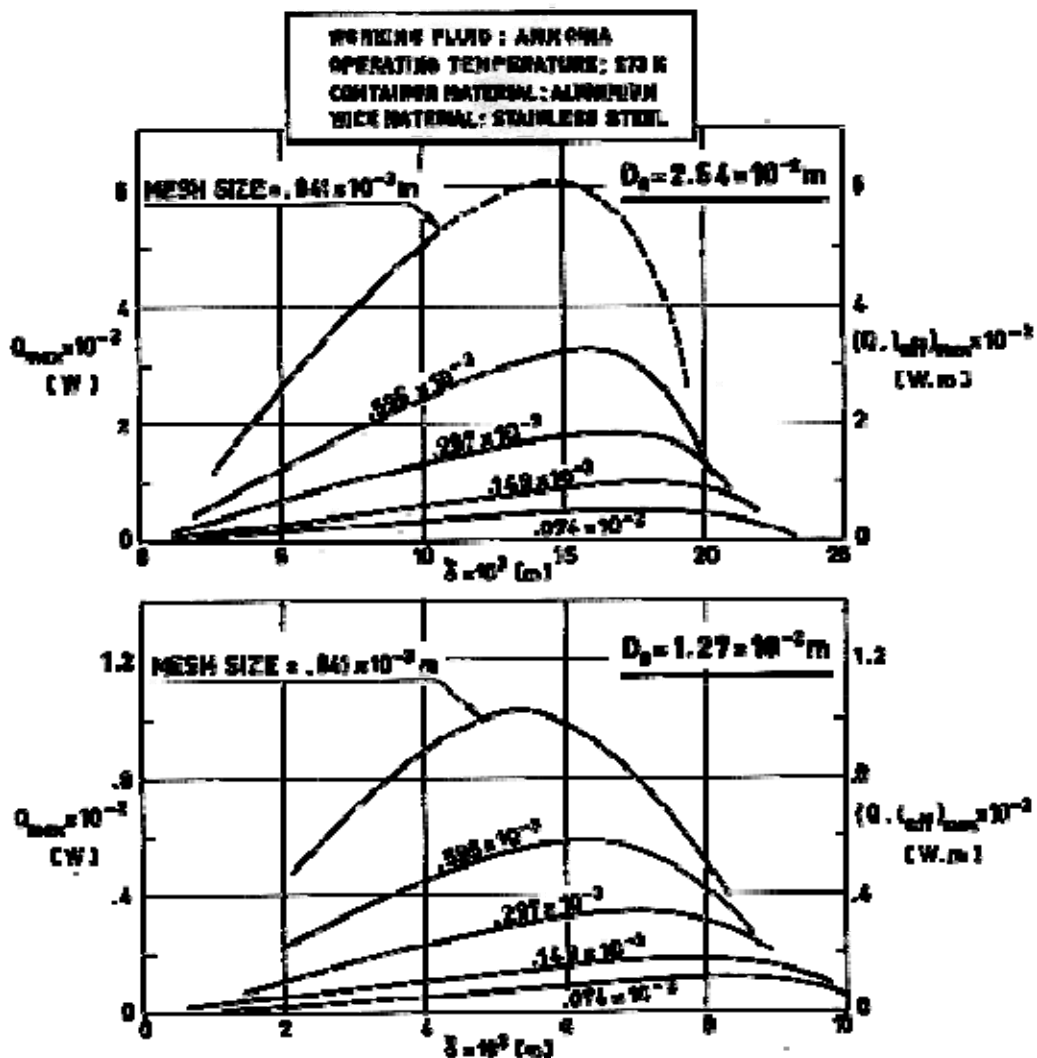


Figure 7-10: Heat Transfer, Q_{max} , and Integral Heat Transport Factor, $[Q \cdot l_{eff}]_{max}$, vs. wick thickness, δ , for several mesh sizes and two heat pipe diameters, D_o . Porous slab wick. Solid lines: vapour laminar flow; dotted lines: vapour turbulent flow.

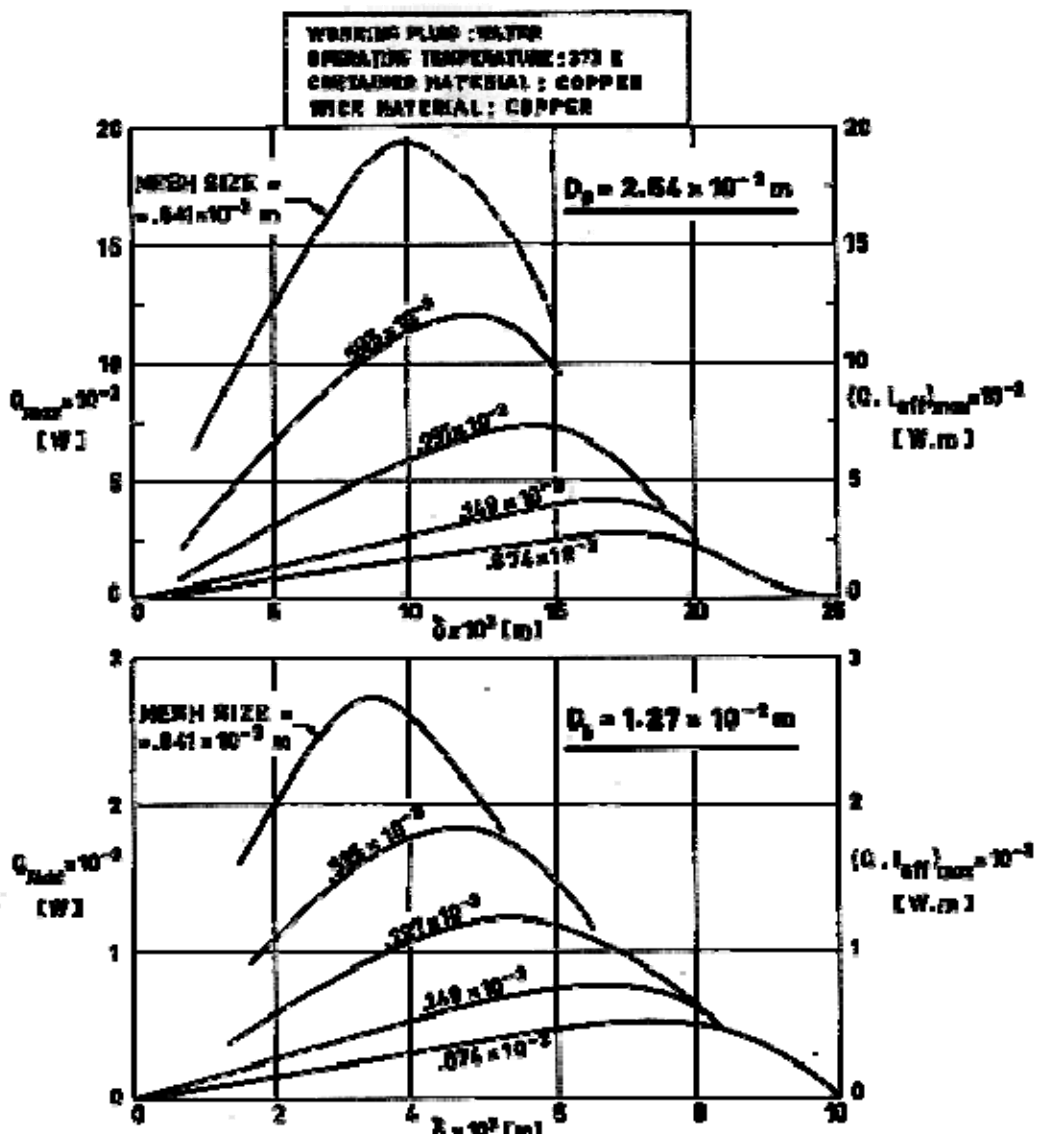
From Skrabek (1972) [88].



Note: non-si units are used in this figure

Figure 7-11: Heat Transfer, Q_{max} , and Integral Heat Transport Factor, $[Q \cdot l_{eff}]_{max}$, vs. wick thickness, δ , for several mesh sizes and two heat pipe diameters, D_o . Porous slab wick. Solid lines: vapour laminar flow; dotted lines: vapour turbulent flow.

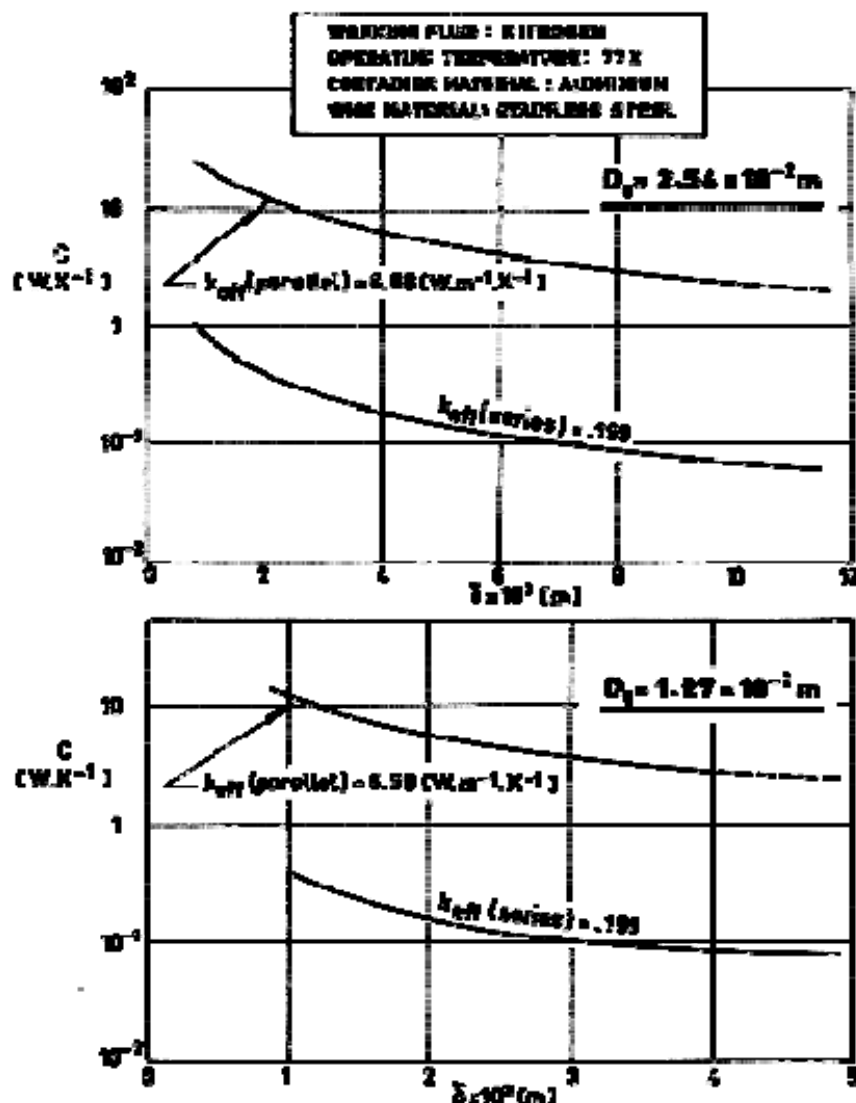
From Skrabek (1972) [88].



Note: non-si units are used in this figure

Figure 7-12: Heat Transfer, Q_{max} , and Integral Heat Transport Factor, $[Q \cdot l_{eff}]_{max}$, vs. wick thickness, δ , for several mesh sizes and two heat pipe diameters, D_o . Porous slab wick. Solid lines: vapour laminar flow; dotted lines: vapour turbulent flow.

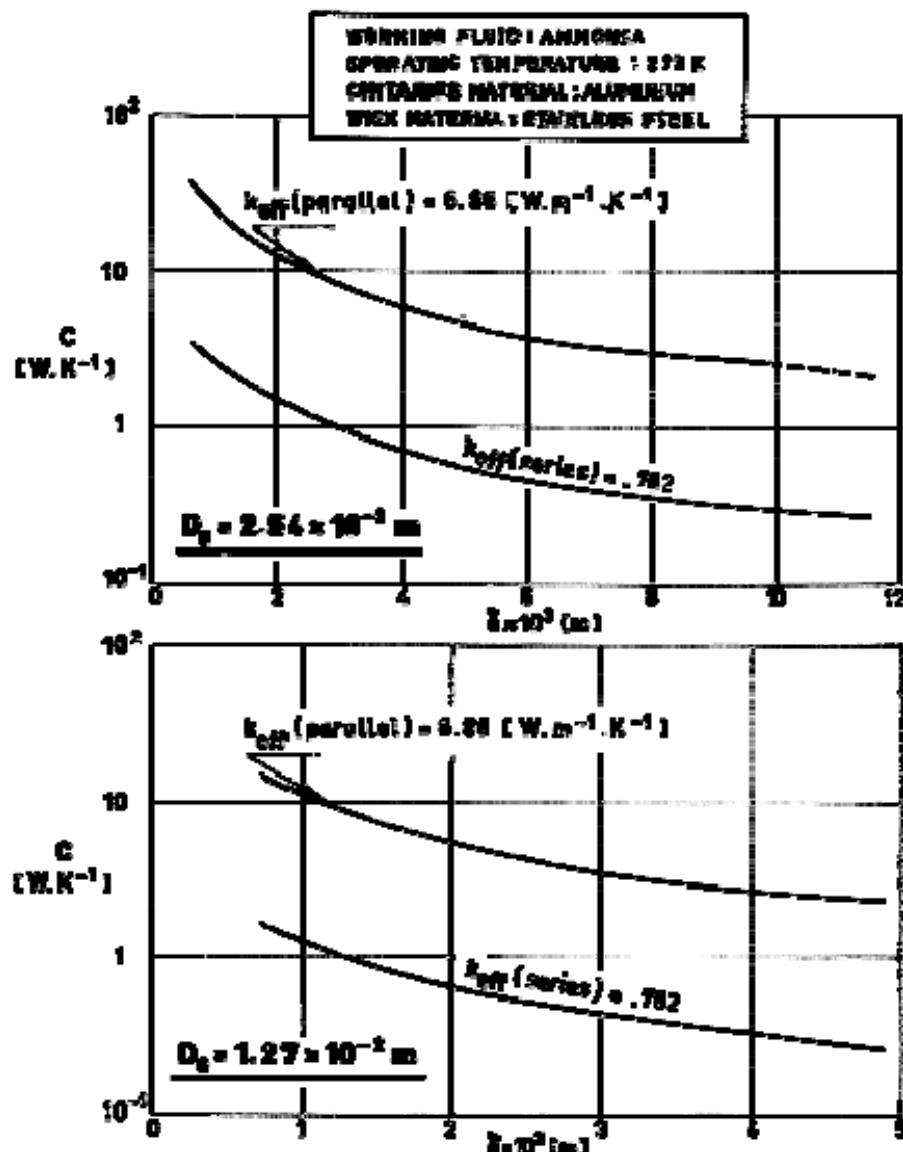
From Skrabek (1972) [88].



Note: non-si units are used in this figure

Figure 7-13: Heat pipe conductance, C , vs. wick thickness, δ , for several wick conductivities, k_{eff} , and two heat pipe diameters, D_o . Circumferential screen wick.

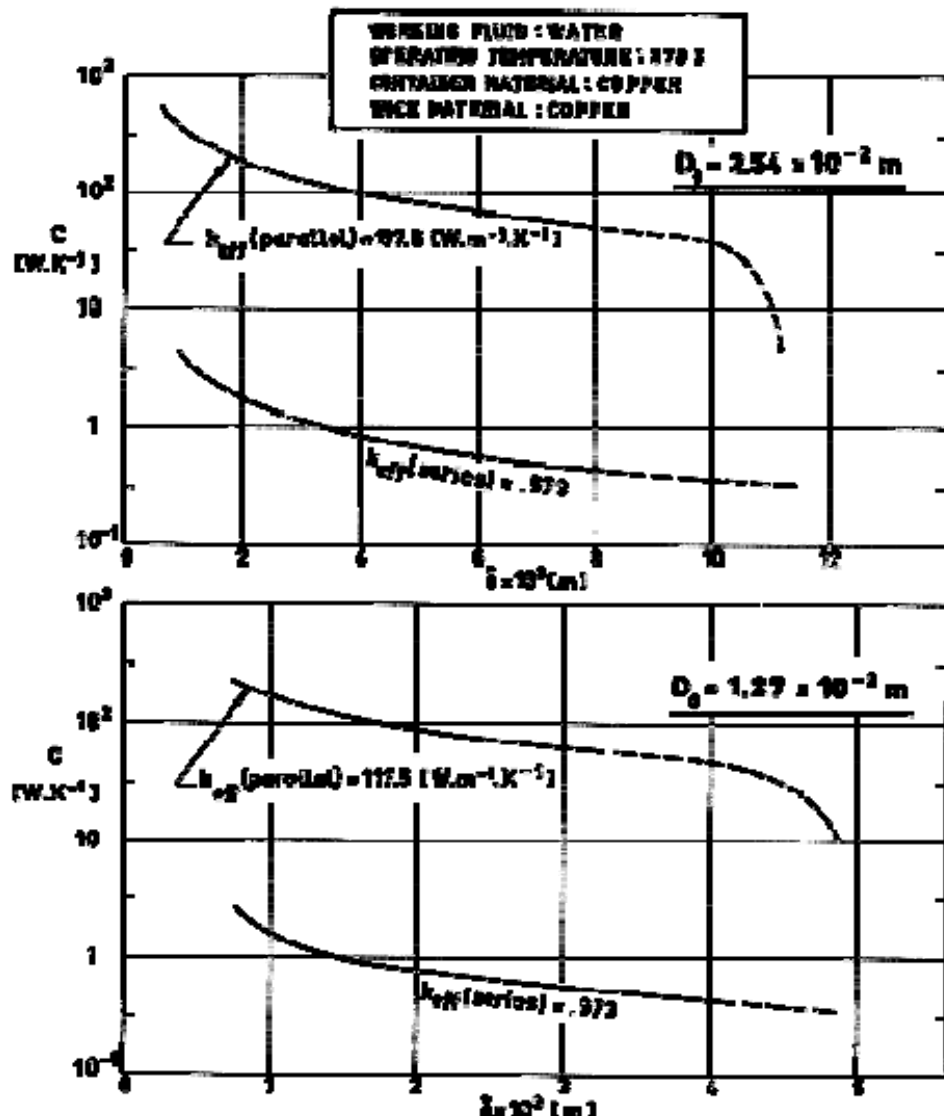
From Skrabek (1972) [88].



Note: non-si units are used in this figure

Figure 7-14: Heat pipe conductance, C , vs. wick thickness, δ , for several wick conductivities, k_{eff} , and two heat pipe diameters, D_o . Circumferential screen wick.

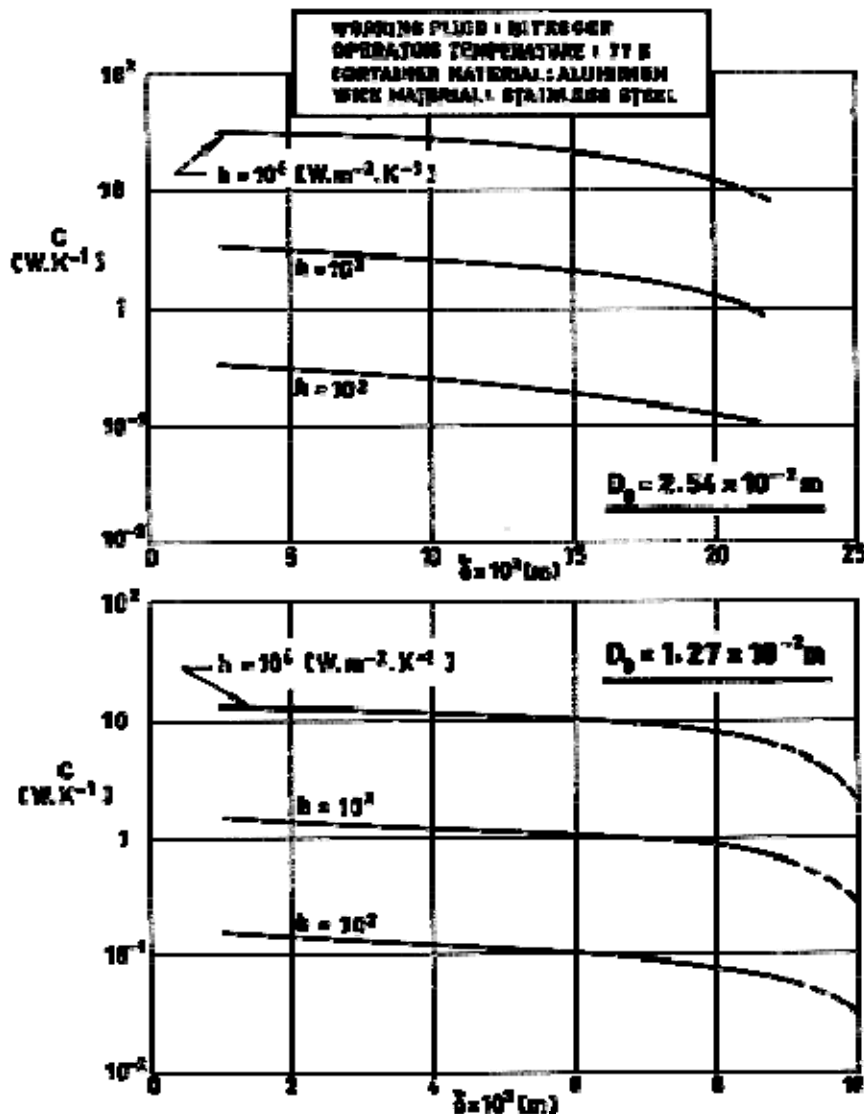
From Skrabek (1972) [88].



Note: non-si units are used in this figure

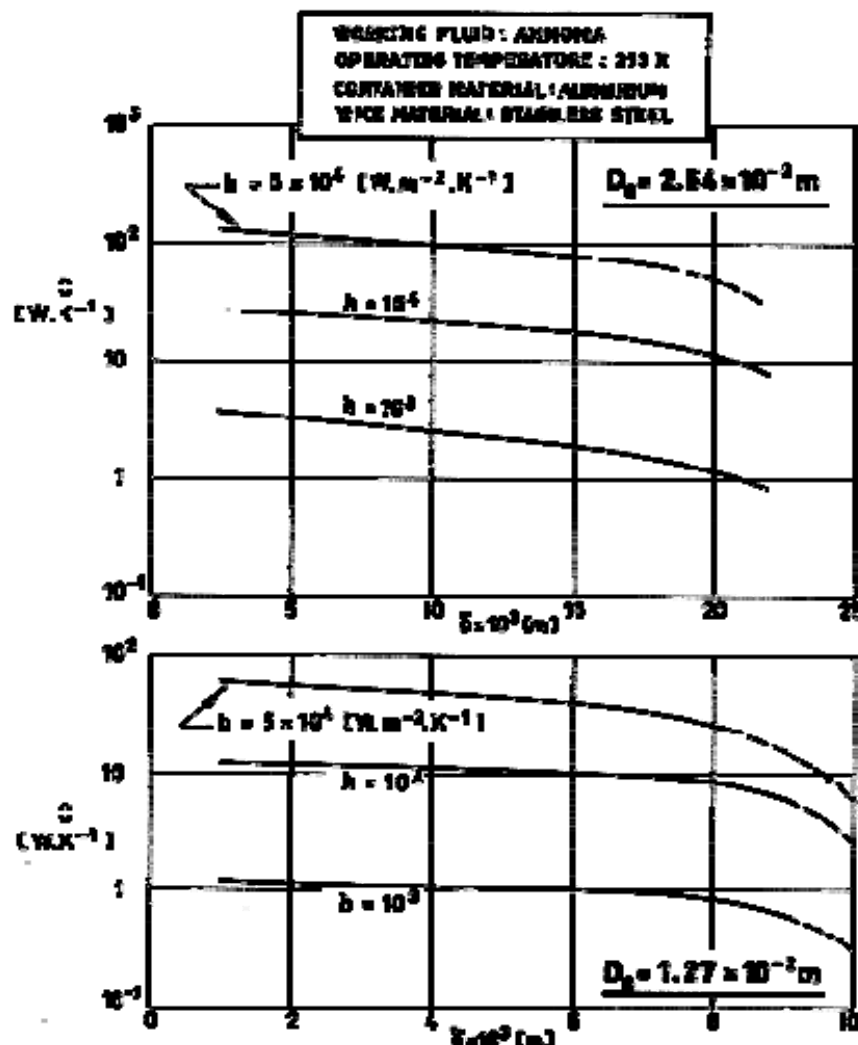
Figure 7-15: Heat pipe conductance, C , vs. wick thickness, δ , for several wick conductivities, k_{eff} , and two heat pipe diameters, D_o . Circumferential screen wick.

From Skrabek (1972) [88].



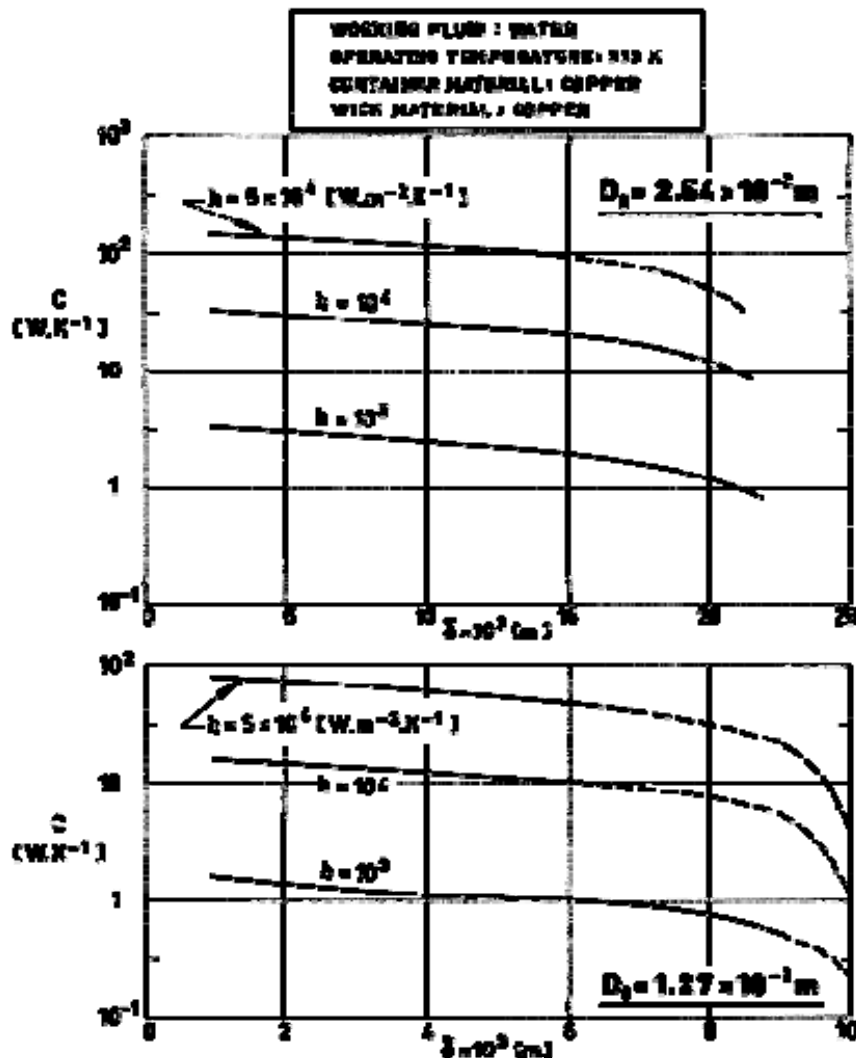
Note: non-si units are used in this figure

Figure 7-16: Heat pipe conductance, C , vs. wick thickness, δ , for several values of the heat transfer coefficient of the wick, h , and heat pipe diameters, D_o . Porous slab wick. From Skrabek (1972) [88].



Note: non-si units are used in this figure

Figure 7-17: Heat pipe conductance, C , vs. wick thickness, δ , for several values of the heat transfer coefficient of the wick, h , and heat pipe diameters, D_o . Porous slab wick. From Skrabek (1972) [88].



Note: non-si units are used in this figure

Figure 7-18: Heat pipe conductance, C , vs. wick thickness, δ , for several values of the heat transfer coefficient of the wick, h , and heat pipe diameters, D_o . Porous slab wick. From Skrabek (1972) [88].

8

Variable conductance heat pipes

8.1 General

The purpose of a variable conductance heat pipe (VCHP) is to control the operating temperature of a given component against variations in the heat dissipation of the component and in the environmental thermal conditions.

Inasmuch as the heat pipe transfers energy between two points utilizing a continuous circulation, some change in the conductance of the heat pipe may be exerted by controlling the mass flow using either of the following techniques:

1. Interruption of the fluid flow, either the liquid flow in the wick or the vapor flow in the core, by means of suitable thermostatically controlled valves.
2. Reduction of the condensation rate; this is normally achieved by a non-condensable gas which tends to collect in the condenser, partially displacing the condensable gas from there.

The second technique is the most widely used up to the present and the only one which is considered here.

In the beginning of the process both condensable and non-condensable fluids are uniformly mixed throughout the pipe.

During the start-up period the heat addition and consequent evaporation at the evaporator induces pressure waves which sweep both condensable and non-condensable gases toward the condenser zone.

Capillary pumping through the wick drives back the condensed gas to the evaporator, while there is no driving force for the non-condensable gas which is trapped (diffusion effects apart) in the condenser end, reducing the volume of the active condenser zone.

For a given mass of either fluid the volume of the inactive portion of the condenser depends on the pressure and temperature, which are controlled by the heat input and subsequent evaporation.

Passive mode of operation. When the pressure increases the interface separating both gases recedes in the condenser, increasing the condenser volume and thence the heat transfer capability, without requiring external power.

Active mode of operating. It is possible to decouple somewhat the volume of the non-condensable gas from the heat addition by means of an auxiliary non-condensable gas-heater with a feed-back temperature sensor attached to the heat source.

In order to decrease the stiffness of the non-condensable gas volume, placed at the end of the condenser, a gas reservoir could be provided. Two basic configurations have been considered which differ in the position of the reservoir relative to the pipe.

In the cold reservoir configuration, Figure 8-1, the reservoir is placed at the end of the condenser and is wicked in order to assure the return of the condensable gas which may enter there. In this configuration the partial vapor pressure of the non-condensable gas is controlled by the temperature of the environment surrounding the reservoir. The addition to the reservoir of a feed-back controlled heater to devise an active variable conductance heat pipe is straightforward, at least in principle.

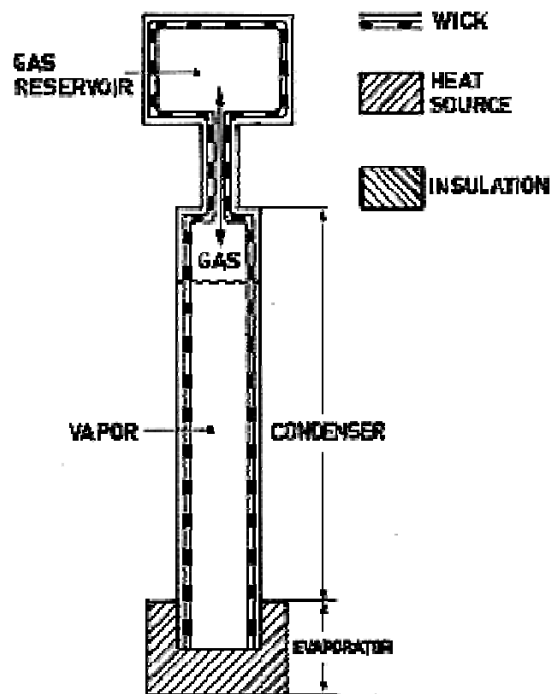


Figure 8-1: VCHP with cold reservoir.

The coupling of the non-condensable gas pressure with the heat source temperature can be made more exclusive with the hot reservoir configuration, Figure 8-2. There the reservoir (unwicked) is placed adjacent to the evaporator, thence its temperature is approximately equal to that of the evaporator. As Figure 8-2 shows, the condensed fluid has no chance of reaching the hot reservoir since it has an easier path to the evaporator through the wick, whereas the gas reservoir is unwicked.

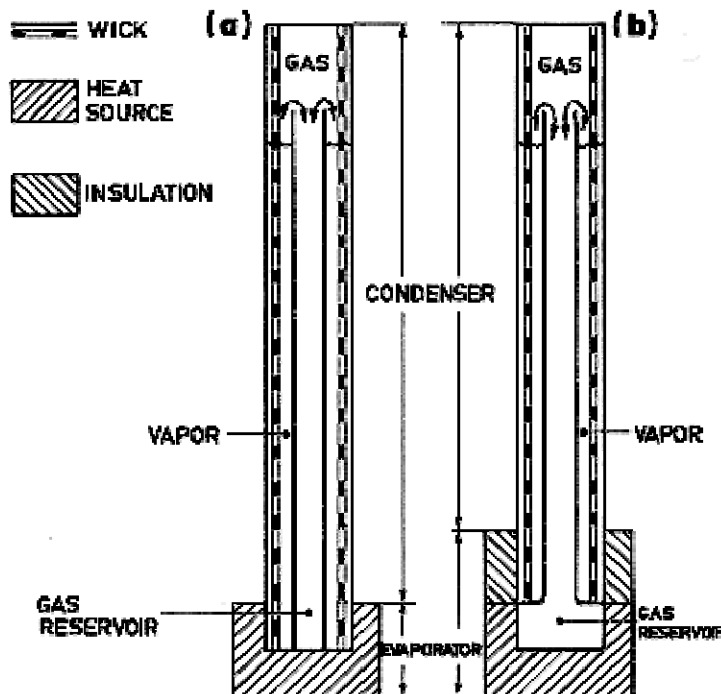


Figure 8-2: VCHP with hot reservoir. (a) Internal hot reservoir. (b) External hot reservoir.

8.2 Design considerations

This part concerns several aspects of VCHPs, namely: diffusion effects, working fluid selection, and reservoir sizing.

8.2.1 Diffusion of the working fluid

The thermal control achieved by a VCHP is defined in terms of a nominal control temperature and control range. For example, a component at 293 ± 2 K has a nominal control temperature of 293 K and a control range of 4 K. When variable conductance is accomplished by means of a non-condensable gas the control range is determined by the volume of the gas reservoir, whereas the nominal control temperature depends on the mass of the gas.

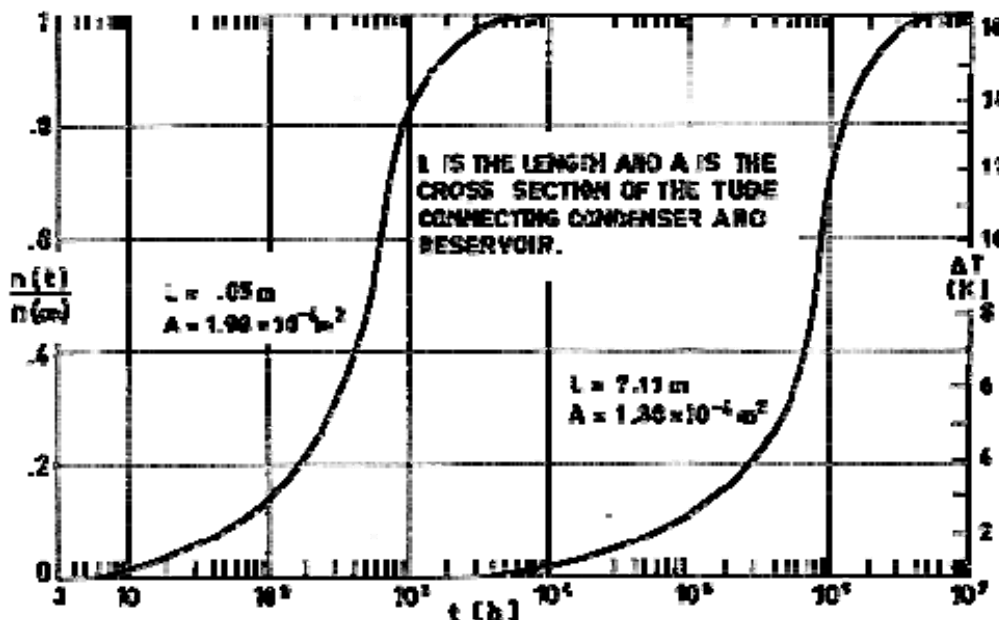
Diffusion, neglected up to now, influences the performance of the VCHP. When the partial pressure of the working fluid is below the equilibrium saturation pressure at the reservoir temperature, the working fluid, diffused as a gas into the reservoir, remains there, not being sucked by the wick. Thence, the volume of the non-condensable gas increases and the heat pipe conductance decreases.

In order to estimate the diffusion effects on the heat pipe thermal conductance, it is assumed that at instant $t = 0$ the reservoir is filled with pure non-condensable gas, while the remainder of the heat pipe, except evaporator and wick which are irrelevant in this analysis, is filled by the working gas. The rate at which the concentration, n , of the working gas in the reservoir approaches (by diffusion) its steady state value is a function of heat pipe geometry, the diffusion coefficient of the working gas through the non-condensable gas, and the distance between the condenser and the reservoir.

Figure 8-3 shows the ratio $n(t)/n(\infty)$ for a hypothetical non-condensable gas heat pipe. $n(t)$ is the number of moles of working fluid vapor diffused into the reservoir up to time t . The ordinate on the

right hand side shows the change by mass diffusion in nominal control temperature which this particular system experiences.

These results have been obtained analytically by solving the laminar diffusion equations in a system having two cylindrical regions of different length and area, which represent the separation tubing and the reservoir.



Note: non-si units are used in this figure

Figure 8-3: Vapor concentration at the reservoir, $n(t)$, over its steady-state value, $n(\infty)$, and control temperature range, ΔT , as functions of time, t . From Hinderman. Waters & Kaser (1972) [35].

8.2.2 Working fluid selection

In addition to the already mentioned criteria for selecting the working fluid of a constant conductance heat pipe, two new criteria should be considered in the selection of working fluid for VCHPs. These are, 1) freezing point, and, 2) slope of the vapor pressure versus temperature curve.

1. In a non-condensable gas VCHP, the working fluid should have a freezing point lower than the temperature of the remaining components of the system, including reservoir and the inactive portion of the condenser. Otherwise the frozen working fluid will not return to the evaporator which will result in drying of the wick.
2. The motion of the interface between vapor and non-condensable gas and, therefore, the control of a non-condensable gas VCHP for a given reservoir volume, is a function of the ratio of the internal pressure change to evaporator temperature change, which depends on the working fluid properties. The most effective fluid for a given control temperature range, $\Delta T = T_{E\max} - T_{E\min}$, will be that having the highest value of the dimensionless pressure ratio, π_r , defined as:

$$\pi_r = p(T_{E\max})/p(T_{E\min})$$

If ΔT is small, of the order of 5 K, one can assume that the latent heat of vaporization, h_{fg} , is independent of the temperature over the range of interest, and the vapor pressure can be approximated by the integrated Clausius-Claperyon equation,

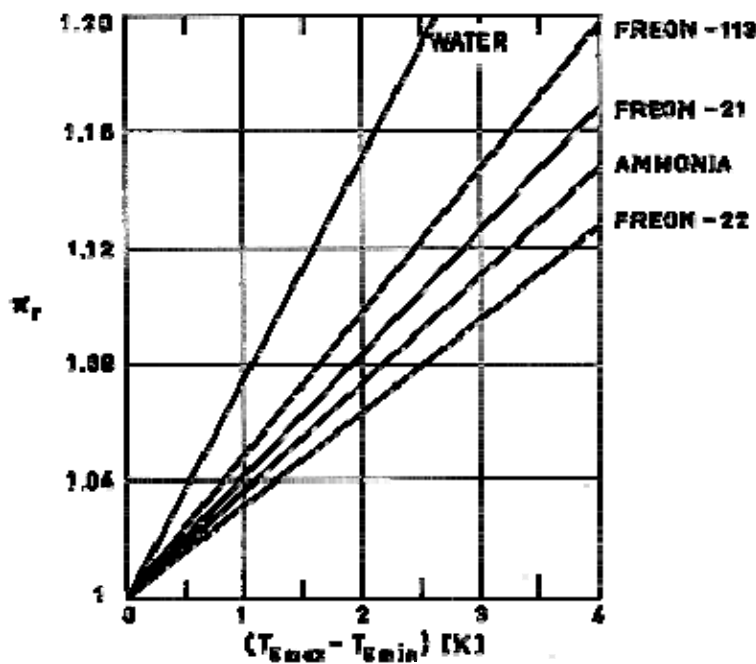
$$p = A \exp[-h_{fg}/RgT],$$

where A is a constant having the dimension of pressure, and

$$\pi_r = \frac{p(T_{E \max})}{p(T_{E \min})} = \exp\left[-\frac{h_{fg}}{R_g} \left(\frac{1}{T_{E \max}} - \frac{1}{T_{E \min}}\right)\right] \quad [8-1]$$

Note: non-si units are used in this figure

Values of π_r for several working fluids are given in Figure 8-4.



Note: non-si units are used in this figure

Figure 8-4: Dimensionless pressure ratio, π_r , vs. control temperature range, $T_{E \max} - T_{E \min}$, for several working fluids. From Hinderman, Waters & Kaser (1972) [35].

8.2.3 Reservoir sizing

The size of the reservoir can be determined by expressing the gas inventory at the hot and cold operating conditions.

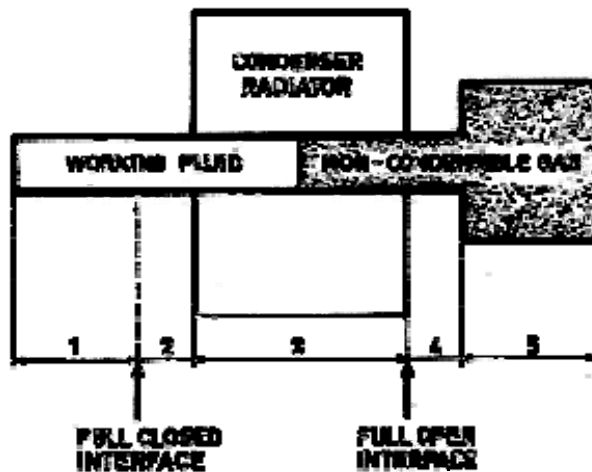


Figure 8-5: Sketch of a variable conductance heat pipe. 1: Evaporator. 2: Adiabatic Section. 3: Condenser. 4: Adiabatic Section. 5: Reservoir.

It is assumed that under cold operating conditions the condenser is blocked and the interface between vapor and non-condensable gas is positioned between the sections 1 and 2 of Figure 8-5.

Under hot operating conditions the heat pipe is fully operational with the abovementioned interface positioned between the section 3 and 4 of Figure 8-5

Data regarding the reservoir to condenser volume ratio, V_R/V_C , for different ranges of evaporator and reservoir temperatures are given in the following four figures.

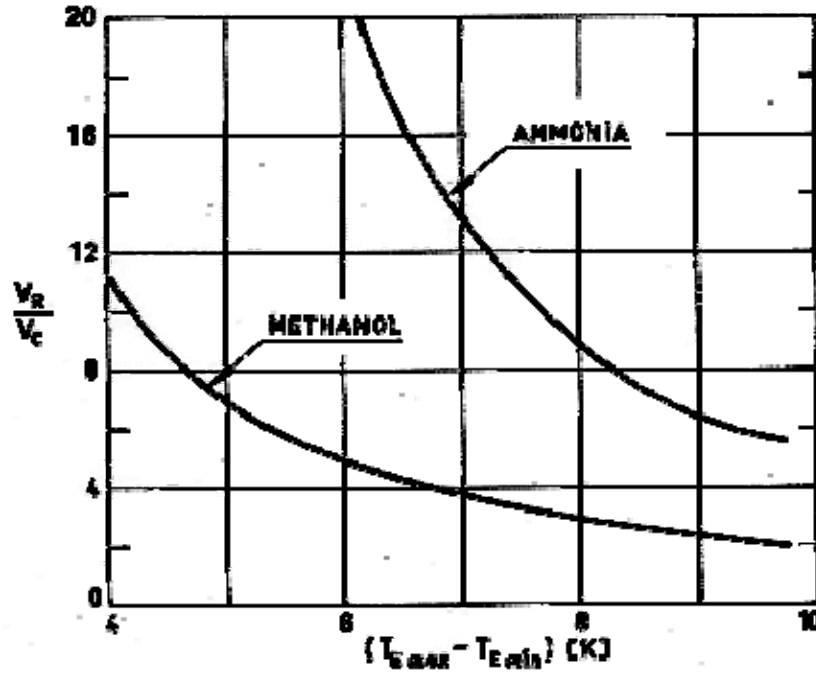


Figure 8-6: Dimensionless reservoir to condenser volume ratio, V_R/V_C , vs. evaporator temperature variation, $(T_{E\max} - T_{E\min})$, for two different working fluids, and a given reservoir temperature variation, $(T_{R\max} - T_{R\min}) = 28$ K. From Edelstein & Hembach (1972) [23].

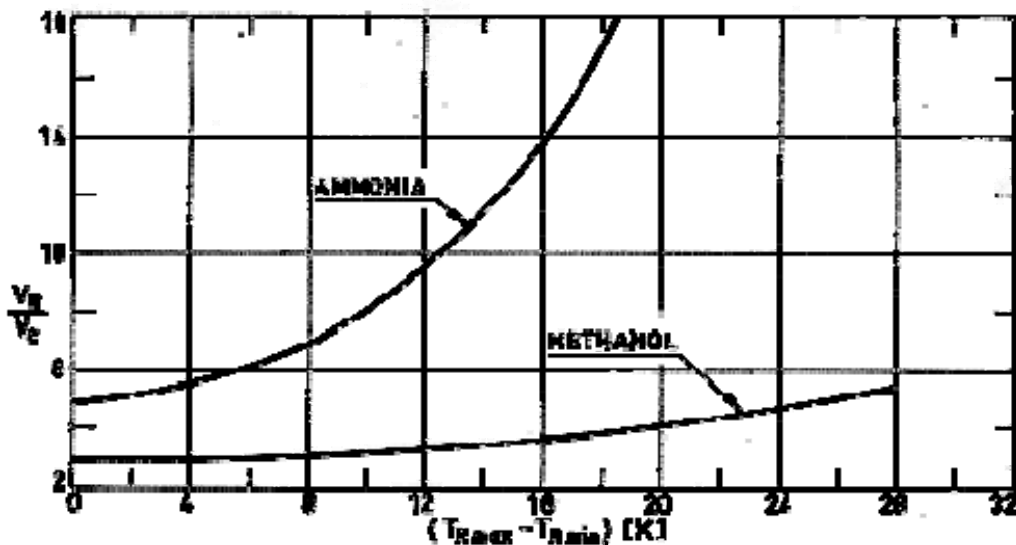


Figure 8-7: Dimensionless reservoir to condenser volume ratio, V_R/V_C , vs. reservoir temperature variation, $(T_{Rmax} - T_{Rmin})$, with fixed evaporator control temperature variation, $(T_{Emax} - T_{Emin}) = 6$ K. From Edelstein & Hembach (1972) [23].

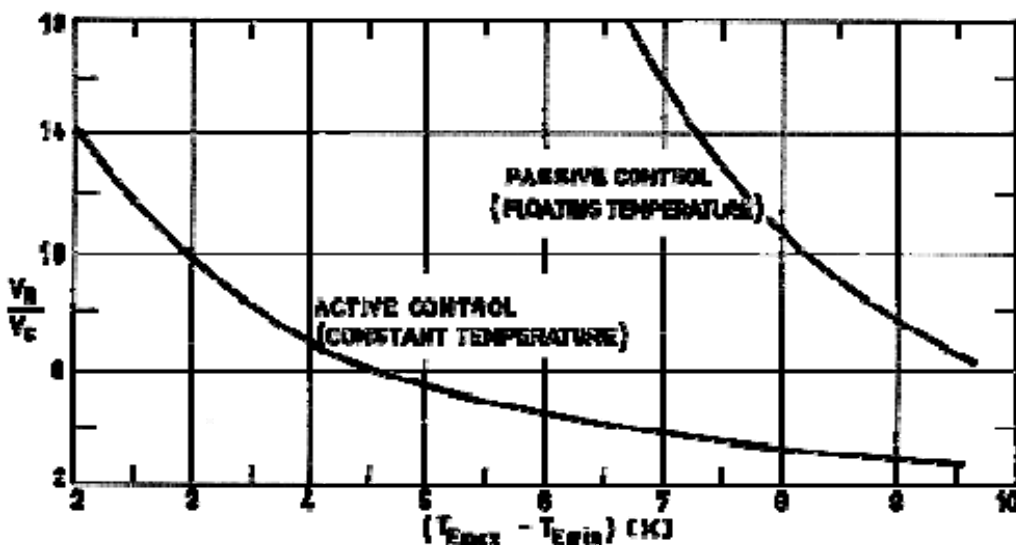


Figure 8-8: Dimensionless reservoir to condenser volume ratio, V_R/V_C , vs. evaporator temperature variation, $(T_{Emax} - T_{Emin})$, for ammonia working fluid. From Edelstein & Hembach (1972) [23].

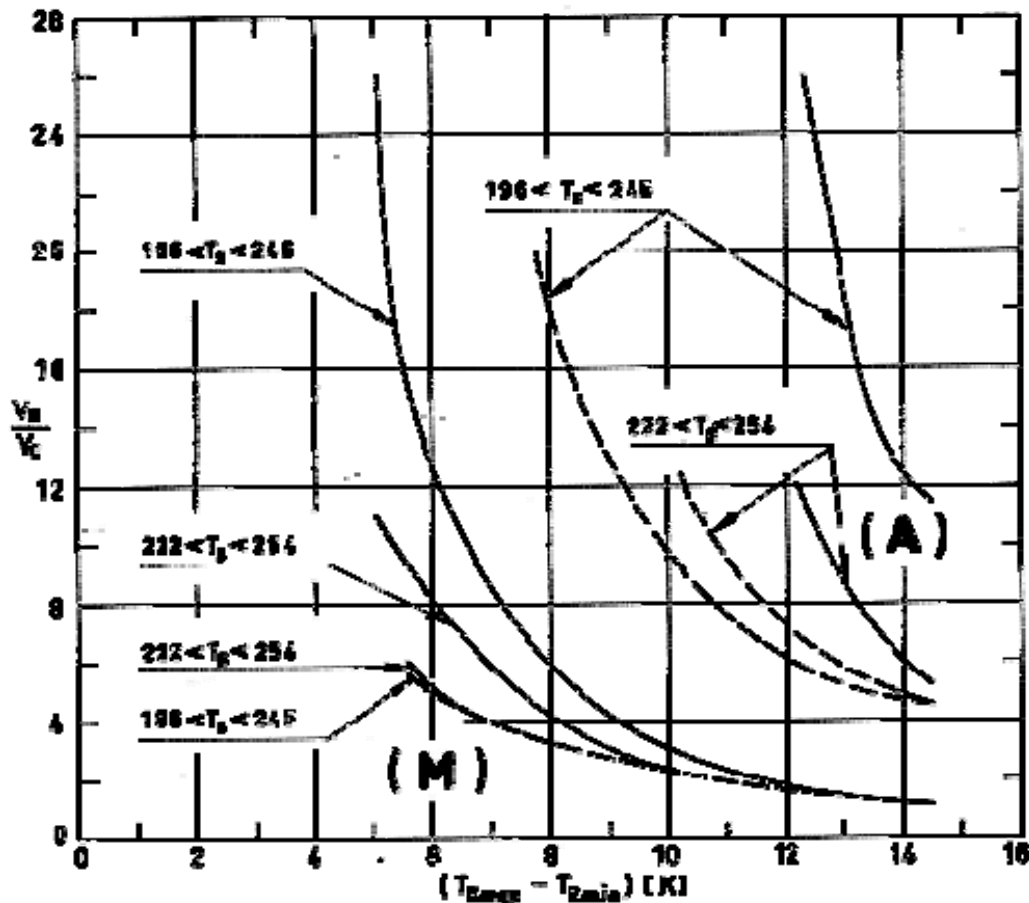


Figure 8-9: Dimensionless reservoir to condenser volume ratio, V_R/V_C , vs. evaporator temperature variation, $(T_{E_{max}} - T_{E_{min}})$. Solid lines: cold reservoir. Dashed lines: hot reservoir. (A) and (M) correspond to ammonia and methanol respectively. T_s is the sink temperature; in one case the back of the radiator is painted black ($222 \text{ K} < T_s < 254 \text{ K}$), and in the other it is aluminized ($196 \text{ K} < T_s < 245 \text{ K}$). Evaporator temperature, $T_E = (287 + (T_{E_{max}} - T_{E_{min}})/2) \text{ K}$. From Kirkpatrick & Marcus (1972) [42].

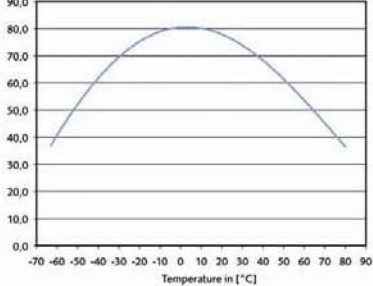
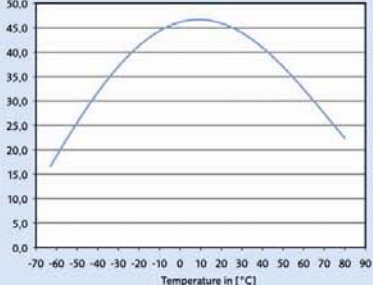
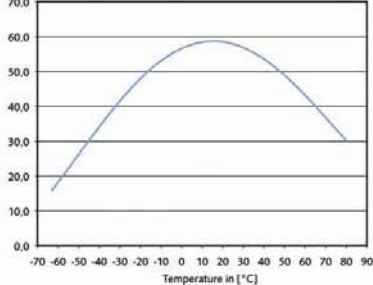
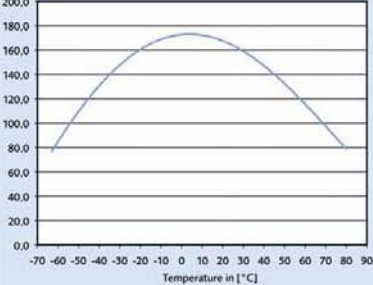
9**Existing System**

Data corresponding to the products supplied by the main European manufacturers are given in this clause.

9.1 Eads Astrium

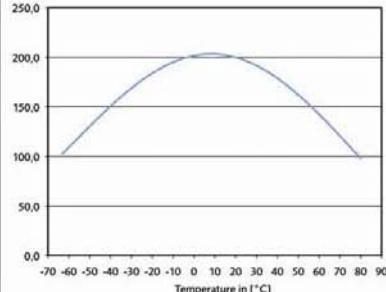
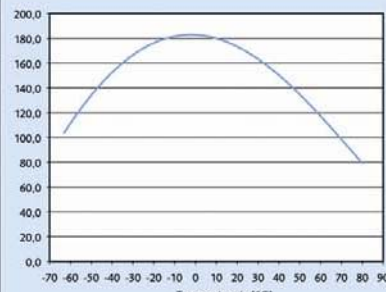
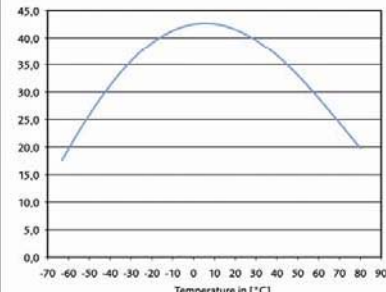
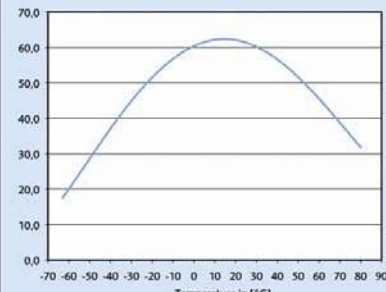
Following tables show the extended catalog of heat pipes from Eads Astrium

Table 9-1: Selected Aluminium Heat Pipe Profiles.

Profile Designation	Profile Geometry	Mass and Dimensions	Heat Transport Capability (Wm)	Qualification, Application, Remarks
WR 4		$m = 0.24 \text{ kg/m}$ $n = 18$ $W = 30 \text{ mm}$ $H = 12.5 \text{ mm}$ $D = 12 \text{ mm}$ $d = 8.2 \text{ mm}$	 Temperature in [°C]	<ul style="list-style-type: none"> National Qualification Programme (1975) Astro 8 ESTEC Life Test (from 1975 to 1986)
WR 6		$m = 0.30 \text{ kg/m}$ $n = 20$ $W = 12 \text{ mm}$ $H = 12 \text{ mm}$ $D = 12 \text{ mm}$ $d = 5.4 \text{ mm}$	 Temperature in [°C]	<ul style="list-style-type: none"> Cryogenic Heat Pipes for SCIAMACHY on Envisat (filled with methane)
WR 9		$m = 0.34 \text{ kg/m}$ $n = 20$ $W = 30 \text{ mm}$ $H = 10 \text{ mm}$ $D = 9 \text{ mm}$ $d = 5 \text{ mm}$	 Temperature in [°C]	<ul style="list-style-type: none"> 24 years ESTEC Life Test Programme (from 1978 to 2002) SPAS-01 Heat Pipe Experiment (STS-07 and STS-11)
WR 11		$m = 0.58 \text{ kg/m}$ $n = 30$ $W = 35.5 \text{ mm}$ $H = 15 \text{ mm}$ $D = 14.5 \text{ mm}$ $d = 8.6 \text{ mm}$	 Temperature in [°C]	<ul style="list-style-type: none"> OMUX Radiator AHR-Advanced Heat Pipe Radiator

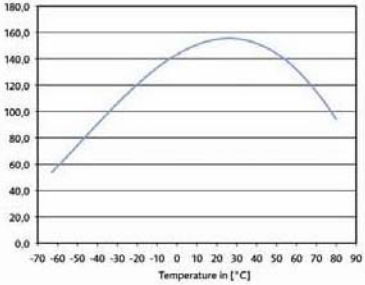
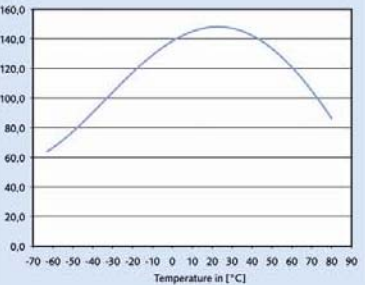
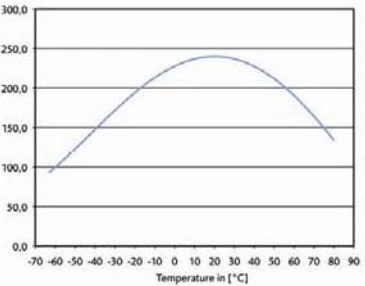
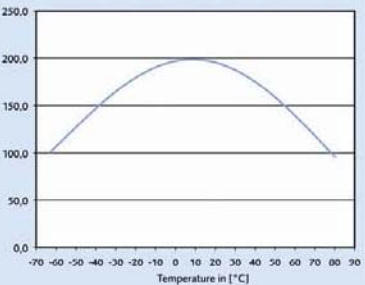
Legend: /m - Mass / W - Profil width / H - Profil height / D - outer tube diameter / d - Vapour diamete / n - Number of grooves

Table 9-2: Aluminium Heat Pipe Profiles (cont.)

Profile Designation	Profile Geometry	Mass and Dimensions	Heat Transport Capability (W/m)	Qualification, Application, Remarks
WR 12		$m = 0.57 \text{ kg/m}$ $n = 32$ $W = 31 \text{ mm}$ $H = 15.5 \text{ mm}$ $D = 15 \text{ mm}$ $d = 9.2 \text{ mm}$	 <p>The graph shows heat transport capability (W/m) on the y-axis (0.0 to 250.0) versus temperature in °C on the x-axis (-70 to 90). The curve starts at approximately 100 W/m at -70°C, rises to a peak of about 210 W/m at 10°C, and then gradually declines to about 100 W/m at 80°C.</p>	<ul style="list-style-type: none"> EUROSTAR Qualification Programme ERS-1 and ERS-2 HPA-Radiator Panel
WR 16		$m = 0.68 \text{ kg/m}$ $n = 32$ $W = 30 \text{ mm}$ $H = 16 \text{ mm}$ $D = 15 \text{ mm}$ $d = 9.2 \text{ mm}$	 <p>The graph shows heat transport capability (W/m) on the y-axis (0.0 to 200.0) versus temperature in °C on the x-axis (-70 to 90). The curve starts at approximately 100 W/m at -70°C, rises to a peak of about 180 W/m at 10°C, and then gradually declines to about 80 W/m at 80°C.</p>	<ul style="list-style-type: none"> OMUX Radiator AHR-Advanced Heat Pipe Radiator
WR 17		$m = 0.15 \text{ kg/m}$ $n = 20$ $W = 9 \text{ mm}$ $H = 9.5 \text{ mm}$ $D = 9 \text{ mm}$ $d = 5 \text{ mm}$	 <p>The graph shows heat transport capability (W/m) on the y-axis (0.0 to 45.0) versus temperature in °C on the x-axis (-70 to 90). The curve starts at approximately 15 W/m at -70°C, rises to a peak of about 40 W/m at 10°C, and then gradually declines to about 20 W/m at 80°C.</p>	<ul style="list-style-type: none"> OLYMPUS Qualification OLYMPUS Radiator Panel HALEX Experiment (STS-41 G)
WR 18		$m = 0.35 \text{ kg/m}$ $n = 20$ $W = 30 \text{ mm}$ $H = 9.5 \text{ mm}$ $D = 9 \text{ mm}$ $d = 5 \text{ mm}$	 <p>The graph shows heat transport capability (W/m) on the y-axis (0.0 to 70.0) versus temperature in °C on the x-axis (-70 to 90). The curve starts at approximately 20 W/m at -70°C, rises to a peak of about 60 W/m at 10°C, and then gradually declines to about 30 W/m at 80°C.</p>	<ul style="list-style-type: none"> OLYMPUS Radiator Panel ERS-1 Tape Recorder GOME AMOS NIS Panel SIILEX EOS Cooling Unit EOS Radiators

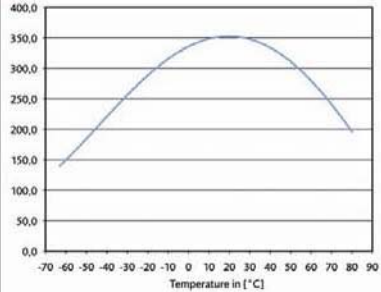
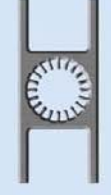
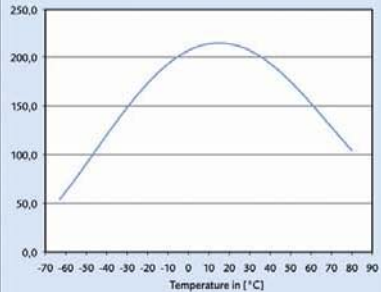
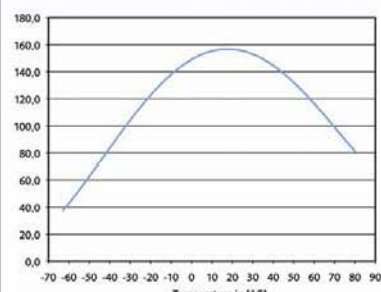
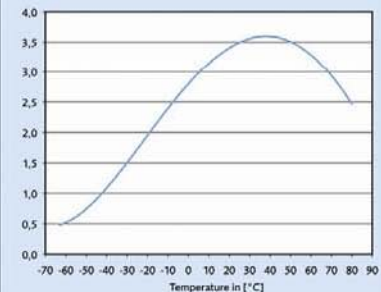
Legend: /m - Mass / W - Profil width / H - Profil height / D - outer tube diameter / d - Vapour diamete / n - Number of grooves

Table 9-3: Aluminium Heat Pipe Profiles (cont.)

Profile Designation	Profile Geometry	Mass and Dimensions	Heat Transport Capability (W/m)	Qualification, Application, Remarks
WR 19		$m = 0.27 \text{ kg/m}$ $n = 22$ $W = 12.5 \text{ mm}$ $H = 13 \text{ mm}$ $D = 12.5 \text{ mm}$ $d = 7 \text{ mm}$	 <p>The graph shows heat transport capability (W/m) on the y-axis (0.0 to 180.0) versus temperature in °C on the x-axis (-70 to 90). The curve starts at approximately (0, 60), rises to a peak of about 155 W/m at 20°C, and then gradually declines.</p>	<ul style="list-style-type: none"> • ERS-1 and ERS-2 - Y Radiator Panel
WR 20		$m = 0.45 \text{ kg/m}$ $n = 22$ $W = 30 \text{ mm}$ $H = 13 \text{ mm}$ $D = 12.5 \text{ mm}$ $d = 7 \text{ mm}$	 <p>The graph shows heat transport capability (W/m) on the y-axis (0.0 to 160.0) versus temperature in °C on the x-axis (-70 to 90). The curve starts at approximately (0, 60), rises to a peak of about 145 W/m at 20°C, and then gradually declines.</p>	<ul style="list-style-type: none"> • SCIAMACHY Radiator A • Polar Platform • TerraSAR-X LCT • Tandem-X LCT
WR 21		$m = 0.73 \text{ kg/m}$ $n = 32$ $W = 39.5 \text{ mm}$ $H = 15.5 \text{ mm}$ $D = 15 \text{ mm}$ $d = 9.2 \text{ mm}$	 <p>The graph shows heat transport capability (W/m) on the y-axis (0.0 to 300.0) versus temperature in °C on the x-axis (-70 to 90). The curve starts at approximately (0, 100), rises to a peak of about 220 W/m at 20°C, and then gradually declines.</p>	<ul style="list-style-type: none"> • OMUX Radiator • Radarsat HPMC Panel • Cryosat-1 Panel • Cryosat-2 Panel
WR 22		$m = 0.47 \text{ kg/m}$ $n = 32$ $W = 30 \text{ mm}$ $H = 15.6 \text{ mm}$ $D = 15 \text{ mm}$ $d = 9.2 \text{ mm}$	 <p>The graph shows heat transport capability (W/m) on the y-axis (0.0 to 250.0) versus temperature in °C on the x-axis (-70 to 90). The curve starts at approximately (0, 100), rises to a peak of about 200 W/m at 20°C, and then gradually declines.</p>	<ul style="list-style-type: none"> • TELECOM 2 NIS Radiator Panels • ERS-1 and ERS-2 ATSR Heat Pipe • ERS-2 Gome External HP

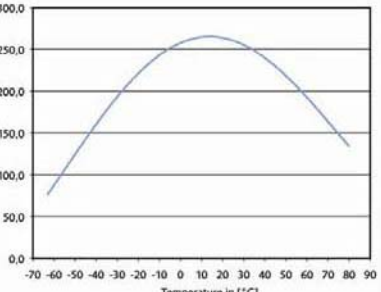
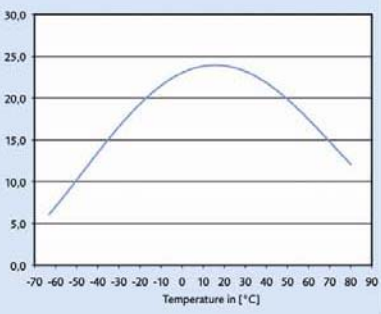
Legend: /m - Mass / W - Profil width / H - Profil height / D - outer tube diameter / d - Vapour diamete / n - Number of grooves

Table 9-4: Aluminium Heat Pipe Profiles (cont.)

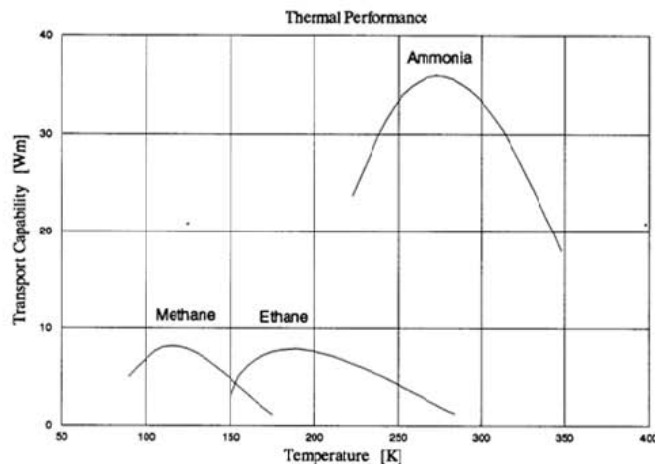
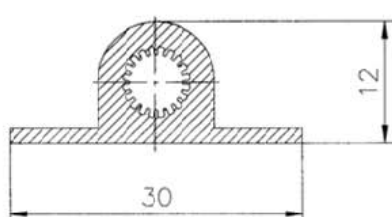
Profile Designation	Profile Geometry	Mass and Dimensions	Heat Transport Capability (Wm)	Qualification, Application, Remarks
WR 24		$m = 0.47 \text{ kg/m}$ $n = 24$ $W = 30 \text{ mm}$ $H = 15.6 \text{ mm}$ $D = 15 \text{ mm}$ $d = 9.1 \text{ mm}$	 Temperature in $^{\circ}\text{C}$	• Profile Characterization
WR 25		$m = 0.45 \text{ kg/m}$ $n = 20$ $W = 30 \text{ mm}$ $H = 13 \text{ mm}$ $D = 12.5 \text{ mm}$ $d = 6.8 \text{ mm}$	 Temperature in $^{\circ}\text{C}$	• Profile Characterization
WR 26		$m = 0.39 \text{ kg/m}$ $n = 18$ $W = 30 \text{ mm}$ $H = 11.5 \text{ mm}$ $D = 11.0 \text{ mm}$ $d = 5.6 \text{ mm}$	 Temperature in $^{\circ}\text{C}$	• Profile Characterization
WR 27		$m = 0.03 \text{ kg/m}$ $n = 6$ $D = 4 \text{ mm}$ $d = 1.6 \text{ mm}$	 Temperature in $^{\circ}\text{C}$	• Mini Heat Pipe

Legend: /m - Mass / W - Profil width / H - Profil height / D - outer tube diameter / d - Vapour diamete / n - Number of grooves

Table 9-5: Aluminium Heat Pipe Profiles (cont.)

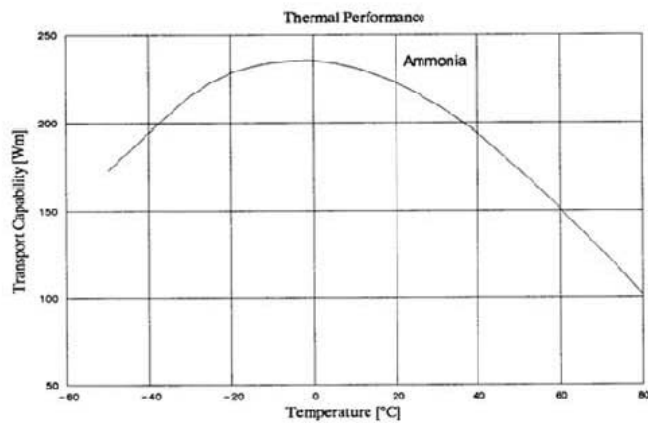
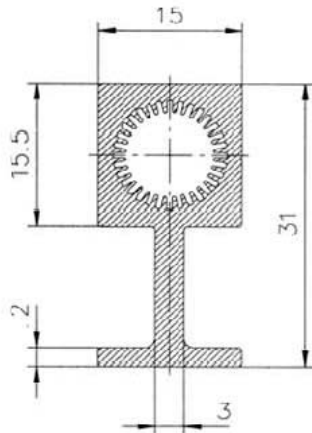
Profile Designation	Profile Geometry	Mass and Dimensions	Heat Transport Capability (Wm)	Qualification, Application, Remarks
WR 28		m = 0.40 kg/m n = 22 W = 30 mm H = 14.2 mm D = 13.1 mm d = 7 mm	 Temperature in [°C]	• Profile Characterization
WR 29		m = 0.14 kg/m n = 10 W = 22 mm H = 6.2 mm D = 6 mm d = 3.1 mm	 Temperature in [°C]	• Cryosat-1 • Kompsat-3 FPA Heat Pipes

Legend: /m - Mass / W - Profil width / H - Profil height / D - outer tube diameter / d - Vapour diamete / n - Number of grooves



Mass and Dimensions	Qualification, Application
Mass: *) 0.33 kg/m Total width: 30 mm Total height: 12 mm Vapour core diam.: 5.4 mm Number of grooves: 20	<ul style="list-style-type: none"> ASTRO 8 (1978) (WR6/Ammonia) Cryogenic Heat Pipes Methane Qualification SCIAMACHY TBU (Methane)

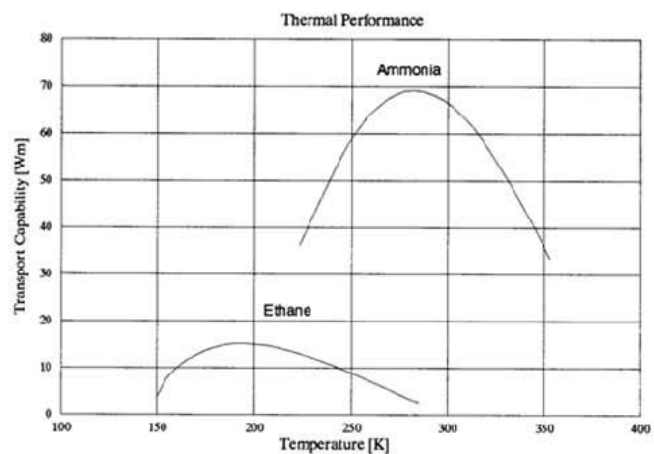
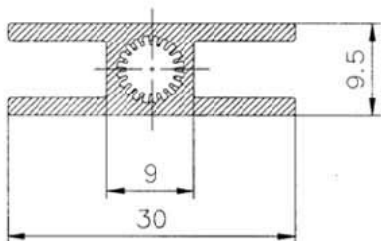
Figure 9-1: WR7 Heat Pipe Profile (Cryogenic Application)

**Mass and Dimensions**

Mass: *) 0.57 kg/m
 Total width: 15 mm
 Total height: 31 mm
 Vapour core diam.: 9.2 mm
 Number of grooves: 32

Qualification, Application

- EUSTAR Qualification
- ERS-1/2
- RADARSAT
- Life test at 100°C since 1991
- Performance Tests with Fluorocarbons

Figure 9-2: WR12 Heat Pipe Profile**Mass and Dimensions**

Mass: *) 0.34 kg/m
 Total width: 30 mm
 Total height: 9.5 mm
 Vapour core diam.: 5.0 mm
 Number of grooves: 20

Qualification, Application

- Lifetests since 1978 (WR8)
- OLYMPUS Qualification
- ERS-1/2, GOME-1/2
- AMOS
- SILEX
- APCF (R114)
- Kompsat-2 (EOS Cooling)

Figure 9-3: WR18 Heat Pipe Profile

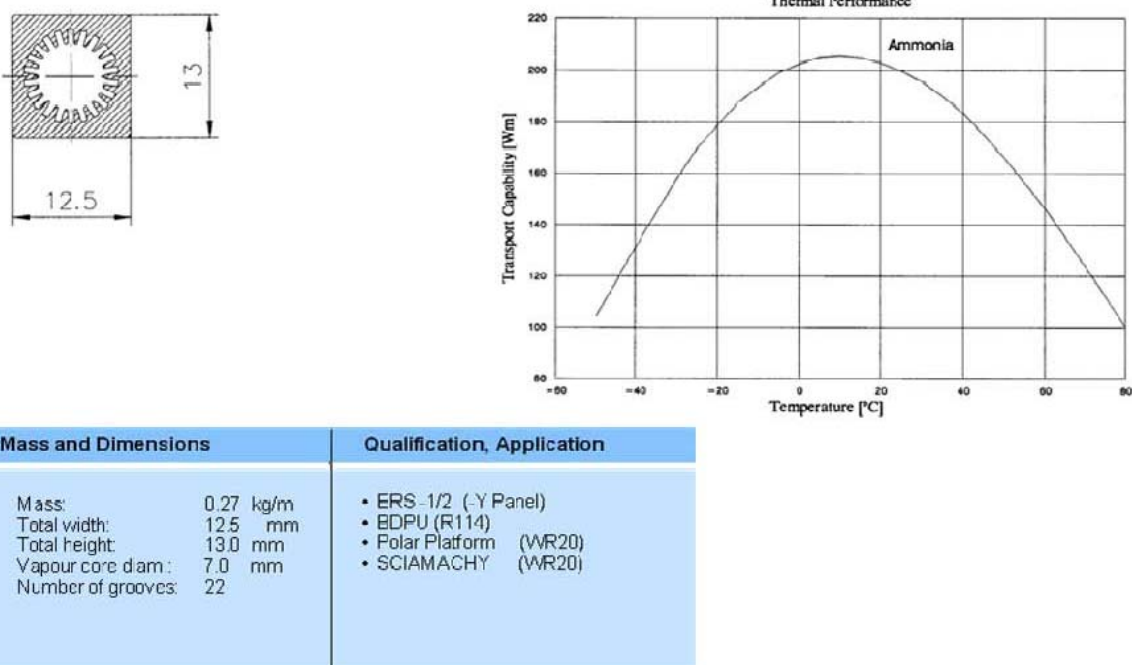


Figure 9-4: WR19 Heat Pipe Profile

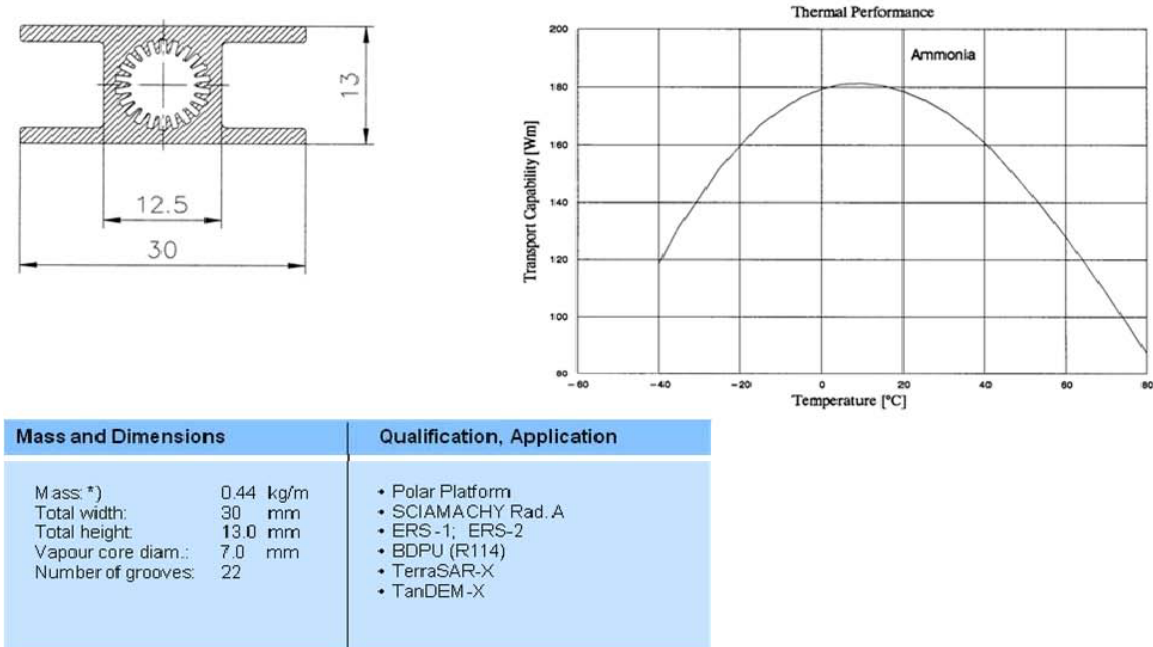


Figure 9-5: WR20 Heat Pipe Profile

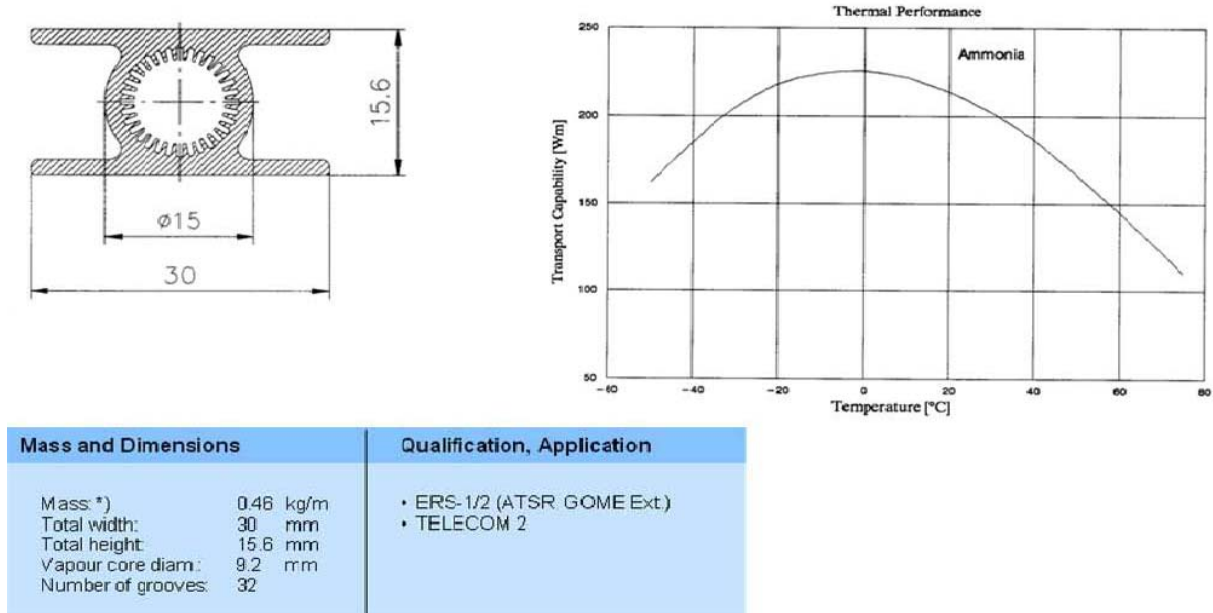


Figure 9-6: WR22 Heat Pipe Profile

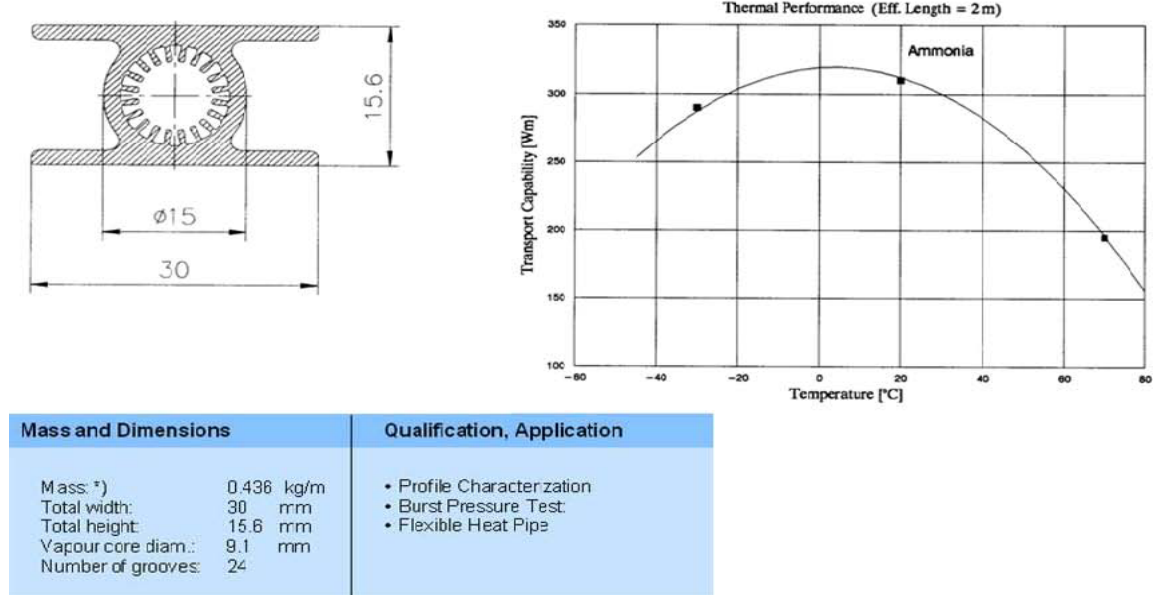
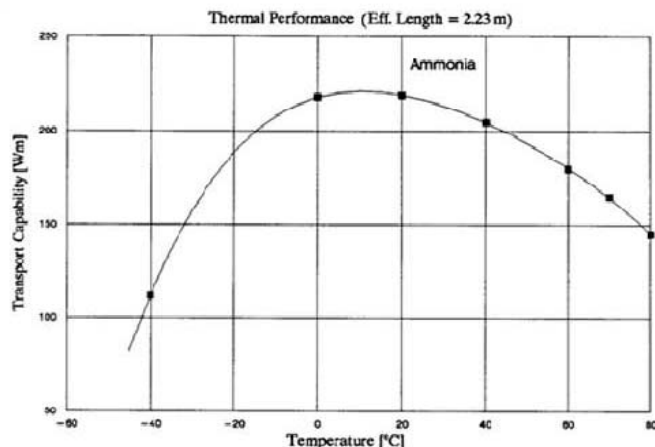
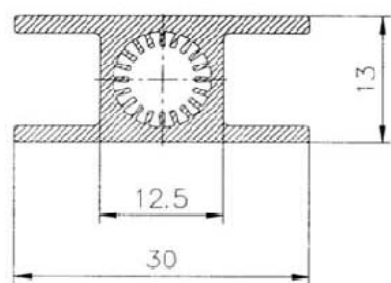
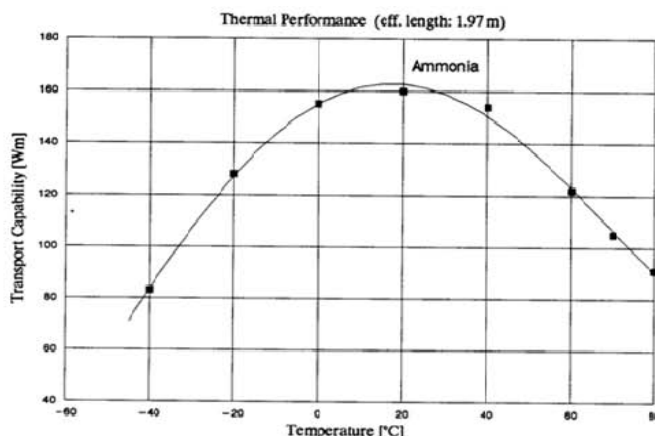
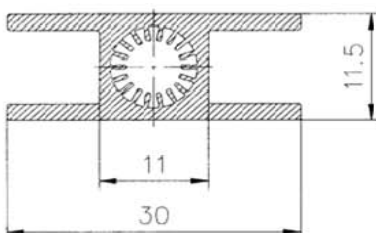


Figure 9-7: WR24 Heat Pipe Profile



Mass and Dimensions	Qualification, Application
Mass: *) 0.42 kg/m Total width: 30 mm Total height: 13.0 mm Vapour core diam.: 6.8 mm Number of grooves: 20	<ul style="list-style-type: none"> Profile Characterization

Figure 9-8: WR25 Heat Pipe Profile



Mass and Dimensions	Qualification, Application
Mass: *) 0.38 kg/m Total width: 30 mm Total height: 11.5 mm Vapour core diam.: 5.6 mm Number of grooves: 18	<ul style="list-style-type: none"> Profile Characterization

Figure 9-9: WR26 Heat Pipe Profile

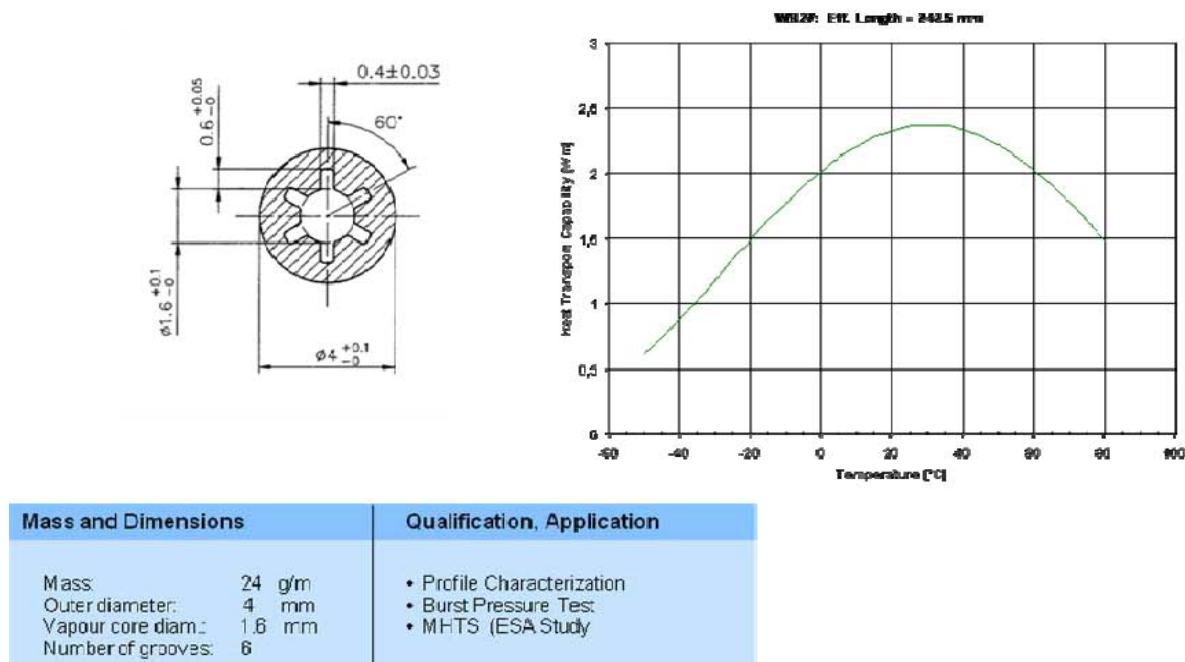


Figure 9-10: WR27 Heat Pipe Profile

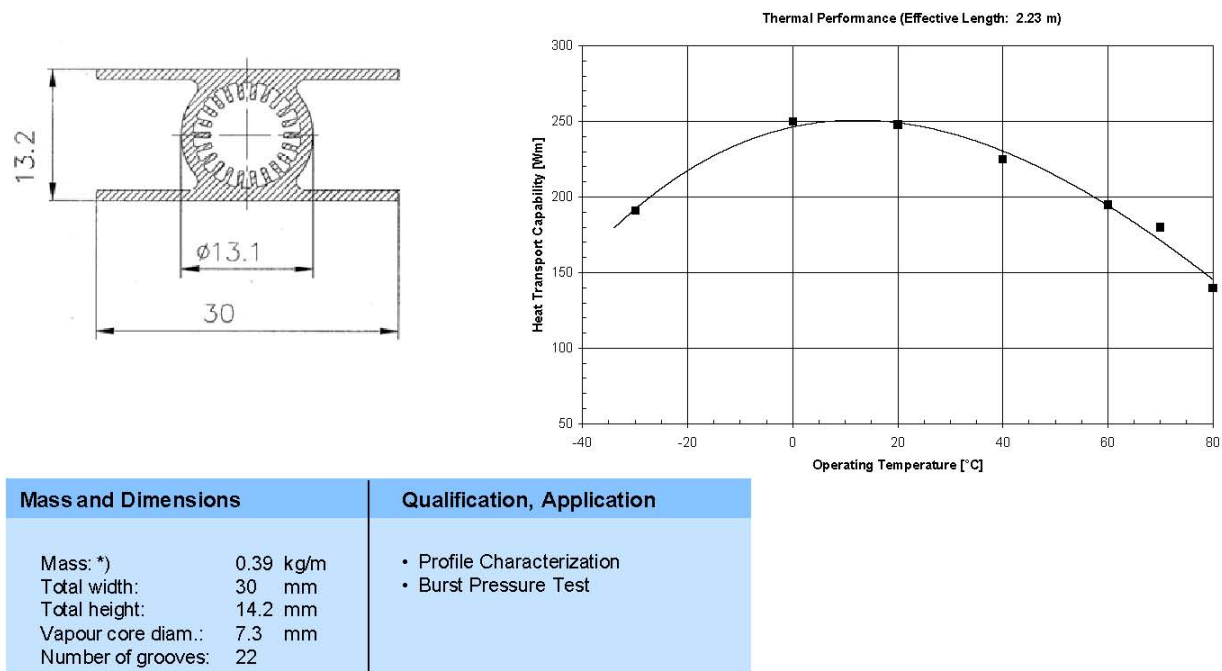


Figure 9-11: WR28 Heat Pipe Profile

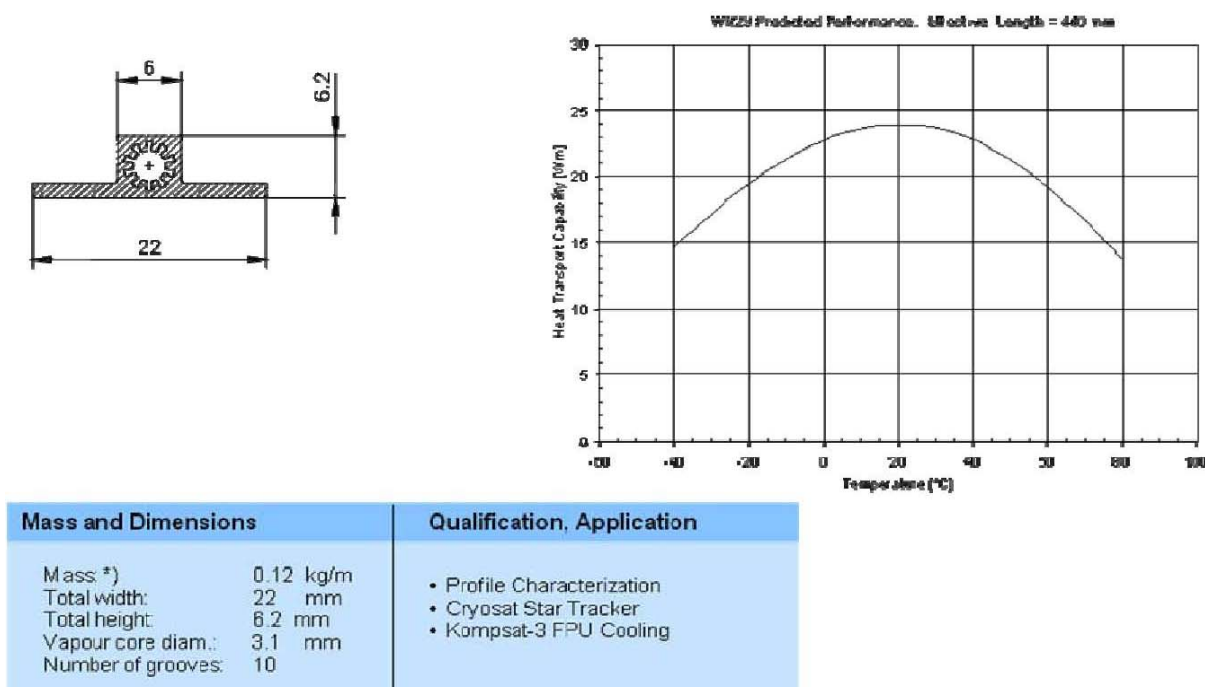


Figure 9-12: WR29 Heat Pipe Profile



Figure 9-13: WR7 Heat Pipe used for SCIAMACHY on ENVISAT

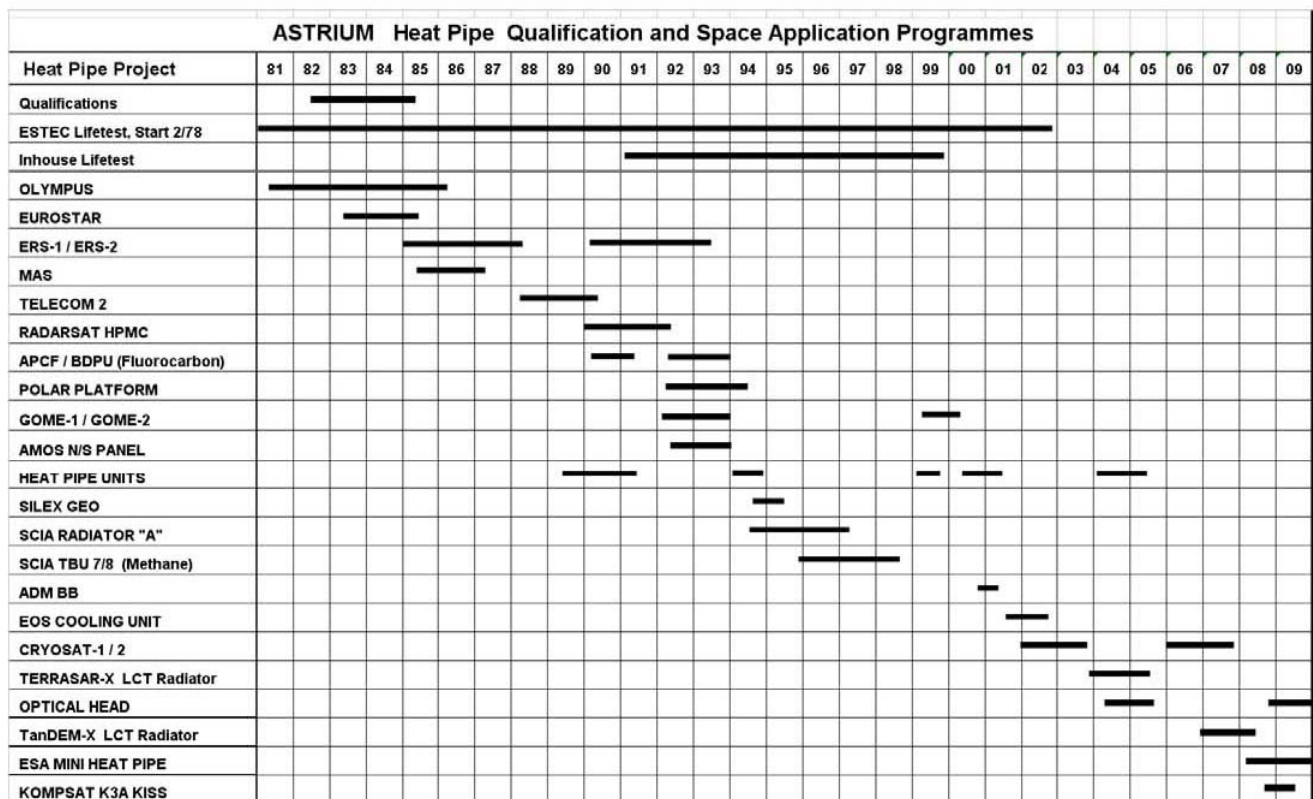


Figure 9-14: EADS ASTRUM HP experience

9.2 Euro Heat Pipes

9.2.1 Aluminium Heat Pipes

This chapter deals with the products from Technical Data Sheet n° 1A: EHP Aluminium Heat Pipes.

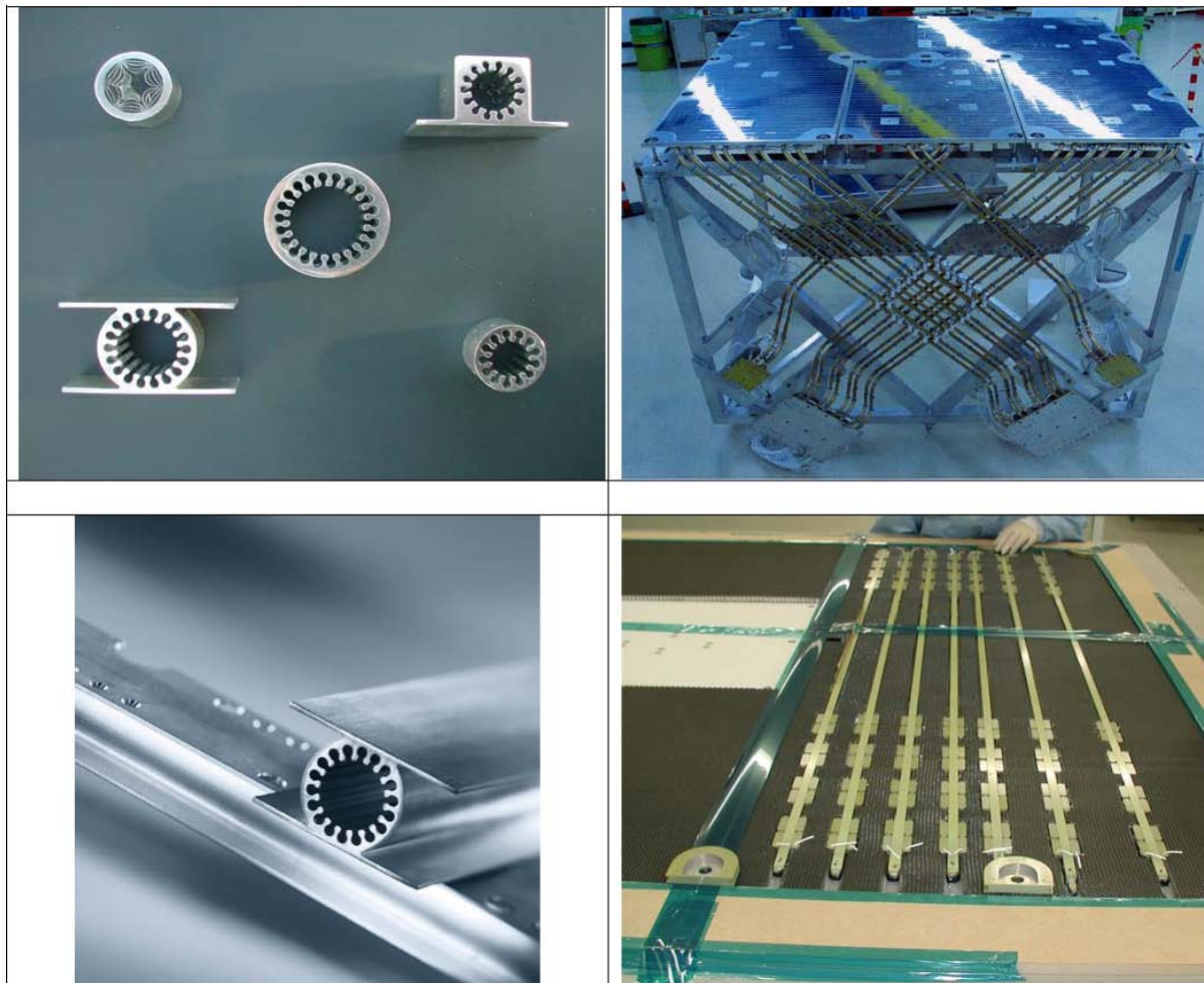


Figure 9-15: EHP: typical Aluminium extruded HP

Table 9-6: EHP Aluminium Heat Pipes Performance

Items	EHP performances	Comments
Type	CCHP	Constant conductance HP
Material	Aluminium 6063 (T5)	
External coating	Alodine or BR127	
Working fluid	NH3	High purity NH3 type N50
Capillary structure	Extruded re-entrant grooves	
Off-the-shelf HP dimensions	Size 6, Size 11 (round and squared shapes) & 11.1LW & 13.2 & 13.2LW & 15 & 19LW & 20 & 25mm	LW = lightweight version Other sizes from 3 to 30mm upon request
HP length	≤ 4 m	
Bending radius	$> 3.5 \times OD$	11.1LW & 13.2LW heat pipes are cannot be bent
Maximal power load	See figure 1	Homogeneous heat spreading on evaporator
Maximum evaporator heat flux	7 W/cm ²	Typical at saddle level
Maximum condenser heat flux	5 W/cm ²	Typical at saddle level
Evaporator conductance	> 5.000 W/m ² K > 120 W/mK	Typical 0G performances at T>-20°C
Condenser conductance	> 3.500 W/m ² K > 85 W/mK	Typical 0G performances at T>-20°C
Mass (without NH3, before machining)	Size 6mm (squared) : 150g/m Size 11mm (round) : 274g/m Size 11mm (squared) : 307g/m Size 11.1LWmm : 147g/m Size 13.2mm : 300g/m Size 13.2LWmm : 264g/m Size 15 mm : 367g/m Size 19 mm LW : 540g/m Size 20 mm : 566g/m Size 25 mm : 575g/m	With 1 saddle 22 x 1.5mm with 2 saddles 30 x 1mm with 2 saddles 30 x 1mm without saddle (squared) with 2 saddles 30 x 1mm with 2 saddles 30 x 1mm with 2 saddles 30 x 1mm with 2 saddles 38 x 1.5mm with 2 saddles 35 x 1.5mm without saddles (round)
Operating T° range	-60°C / + 80°C	
Non op T° range	-65°C / + 90°C	This range can be extended to lower temperature on demand, but it has to be studied due to ammonia

Items	EHP performances	Comments
		freezing below - 77°C.
Proof pressure	> 65 bar for 13.2LW > 110 bar (> 2 x MNOP) > 125bar for 11LW	Cold proof tests
Burst pressure	> 78 bar for 13.2LW > 150bar for 11LW > 166 bar (> 4 x MNOP)	Hot burst tests (at +150°C)
Mechanical environment	-sinus 5-25Hz : +/-10mm -sinus 25-100Hz : 25G -random 20-2000Hz : 30.7Grms -constant acceleration : 35G -20.000 pressure cycles between 1 and 42 bars	
Thermal cycling	1000 cycles between -50°C (1min) and +80°C (1min) 5 cycles between -70°C (2 hours) and +120°C (2hours)	Typical
Ageing tests	Ageing tests for more than 10 years on 3 HP	
He leak rate	< 3.10 -7 atm.cm ³ /s	Typical
Life time	15 years	Typical
Qualification level	0G in orbit qualification & ESA-PSS-49	External and embedded applications

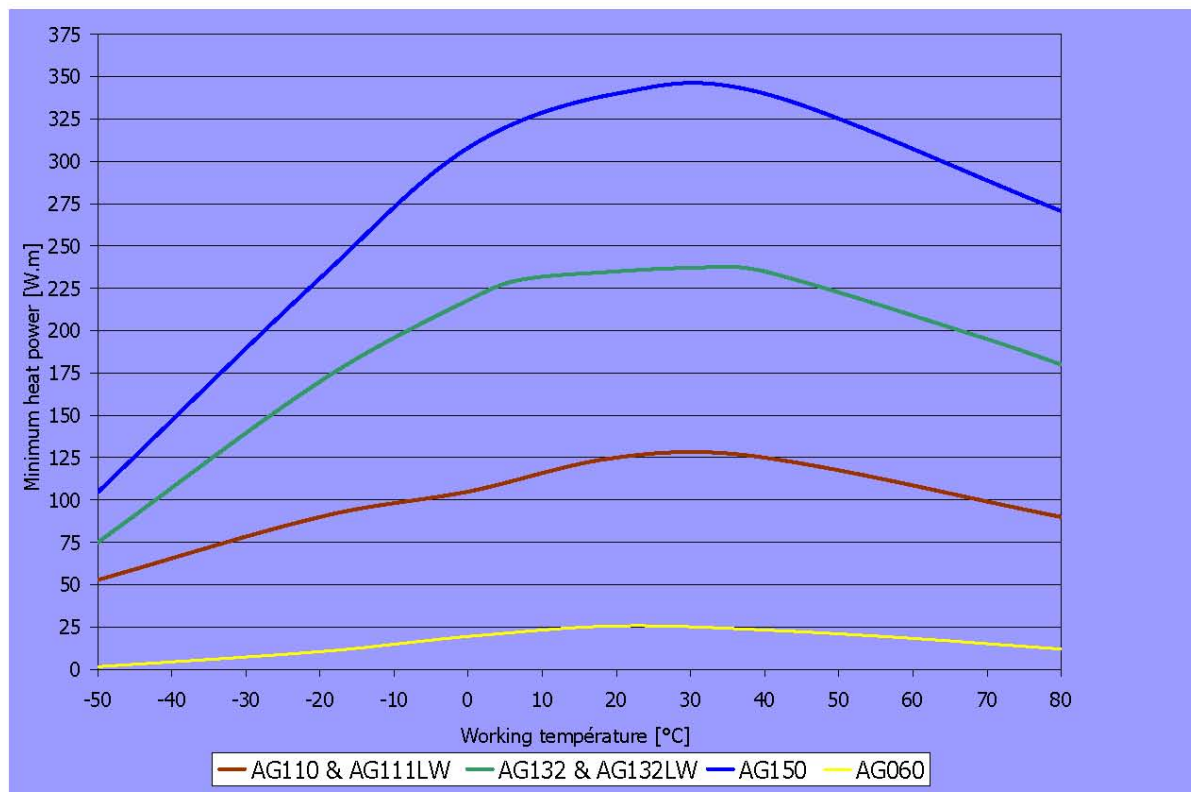
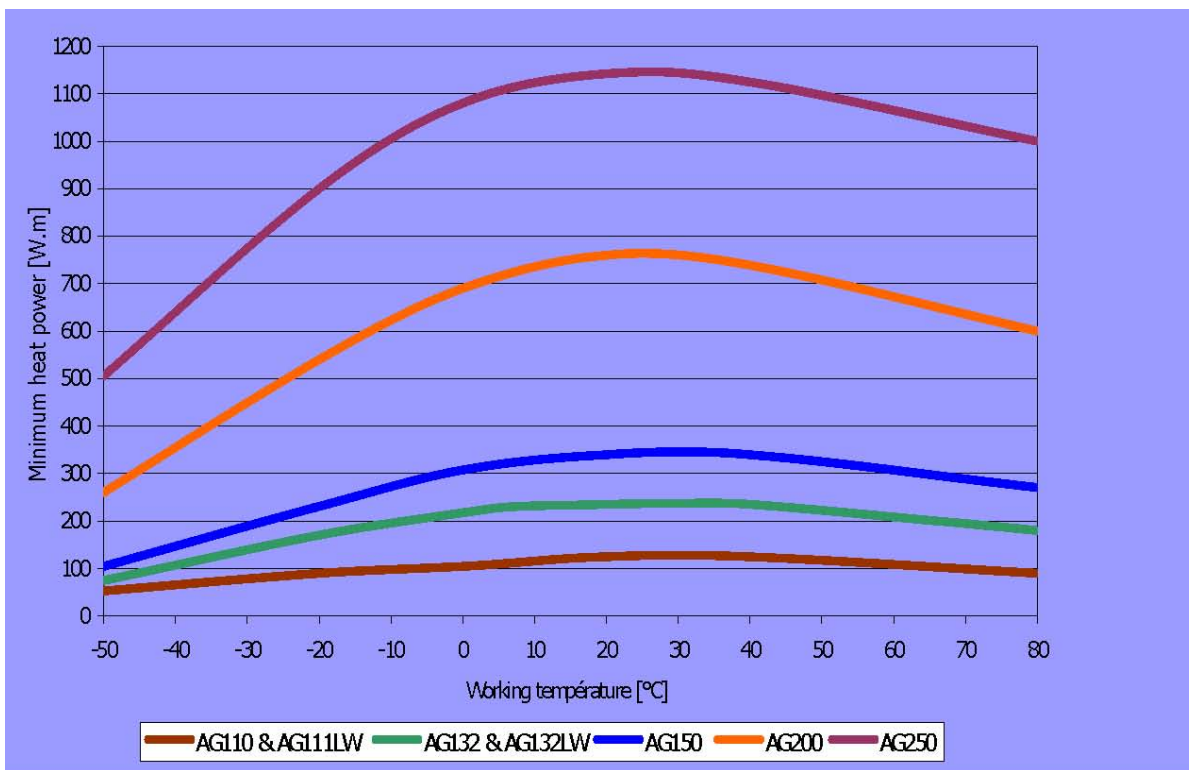
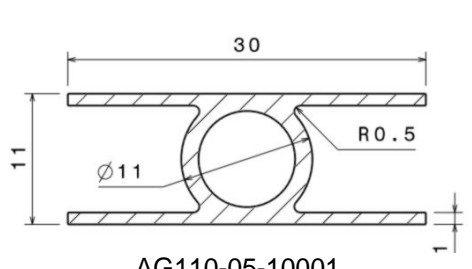
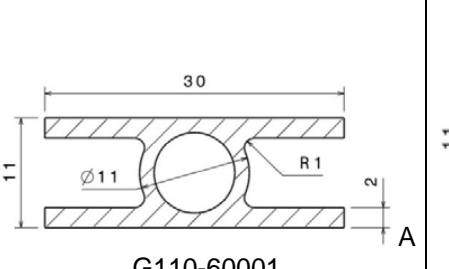
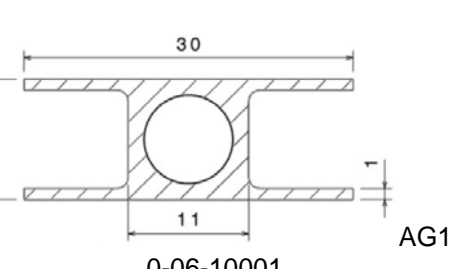
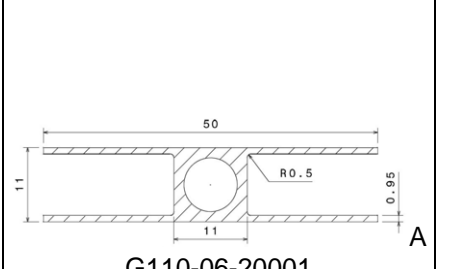
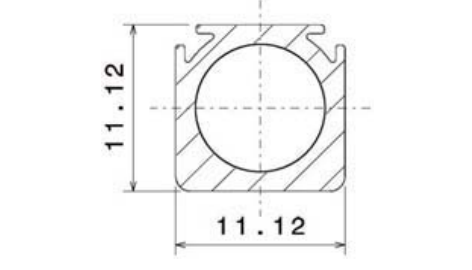
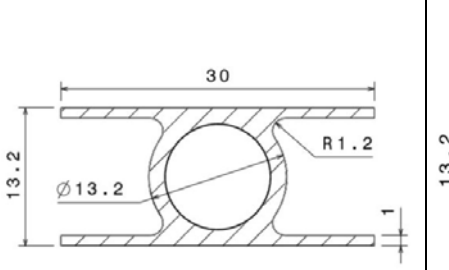
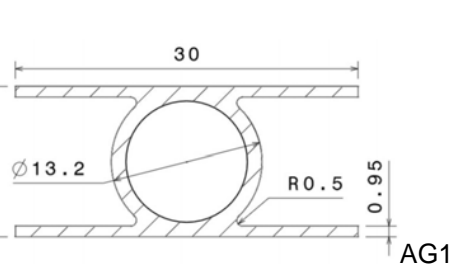
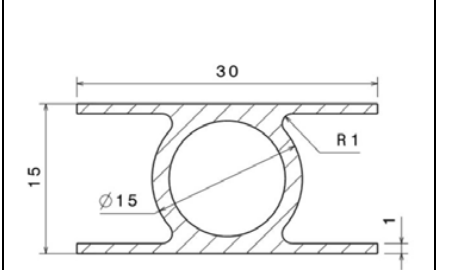
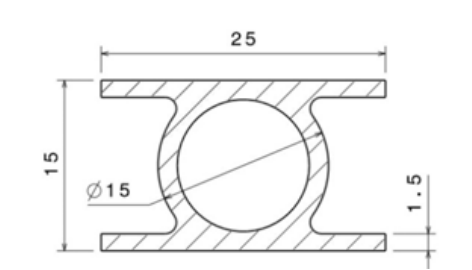
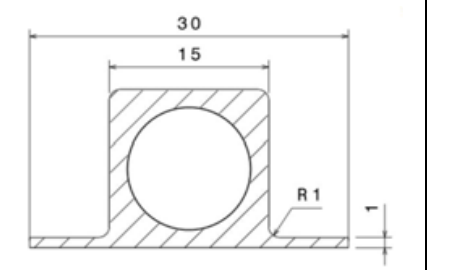
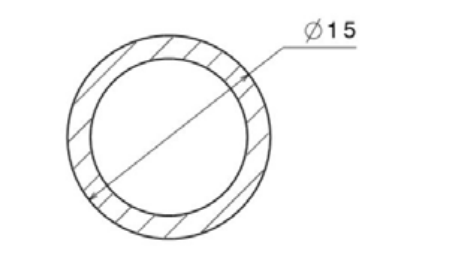
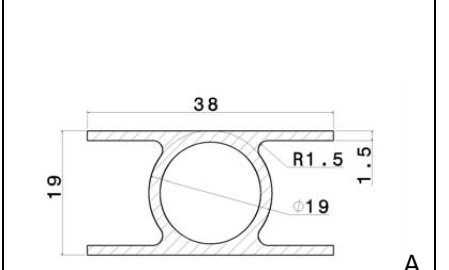
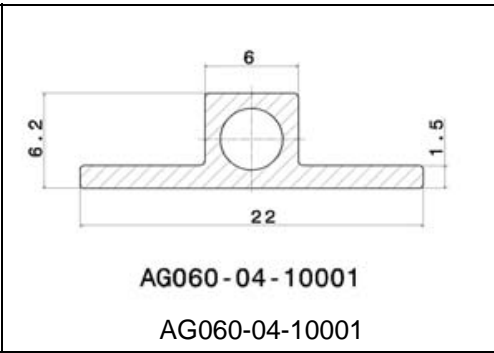
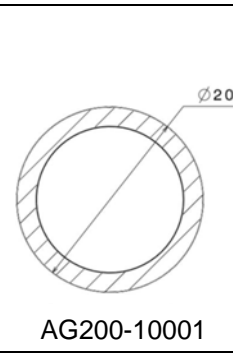
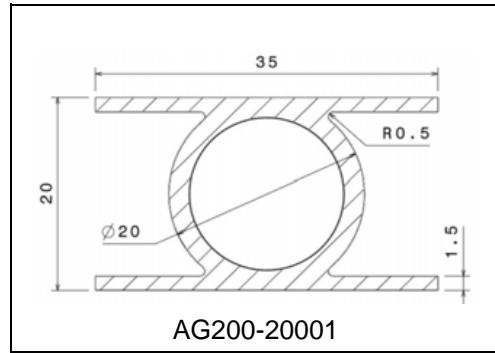
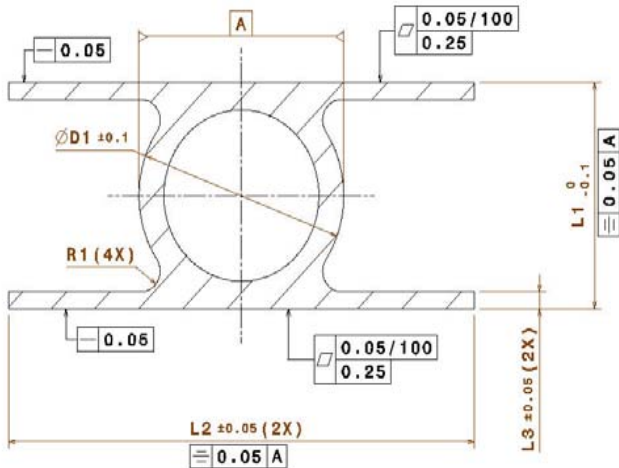


Figure 9-16: Heat transport capability – NH₃ (Note: AG110 = size 11 mm in tens of millimetres.)

Table 9-7: Available HP Profiles

 AG110-05-10001	 G110-60001	 0-06-10001	 AG11
 AG111-05-10001-LW	 AG132-05-10001	 2-05-20001-LW	 AG13
 AG150-20007	 AG150-20001	 AG150-10001	 G190-05-10001



**Notes:**

1. PROCUREMENT SPECIFICATION QUA-EHP-MS-004.
2. GENERAL TOLERANCE I.A.W. DIN 17615 PART 3.
3. FLATNESS IS INSPECTED AS SET BELOW:
PLACE THE HEAT PIPE FLAT ON THE SURFACE TABLE
WITH ITS MOUNTING FACE IN CONTACT WITH THE TABLE.
TO PROVIDE A CONSISTENT LOADING, PLACE 1 KG WEIGHT
EVERY 300 MM ALONG THE LENGTH OF THE PIPE. AN
ADDITIONAL WEIGHT OF 3 KG MAY BE PLACED ON TOP OF
EACH OF THE 1 KG WEIGHTS FOR FLATNESS MEASUREMENTS.

AGXXX STANDARD EHP
PROFILE TOLERANCES
ONLY FOR INFORMATION
08/05/08

Figure 9-17: HP Profile Tolerances

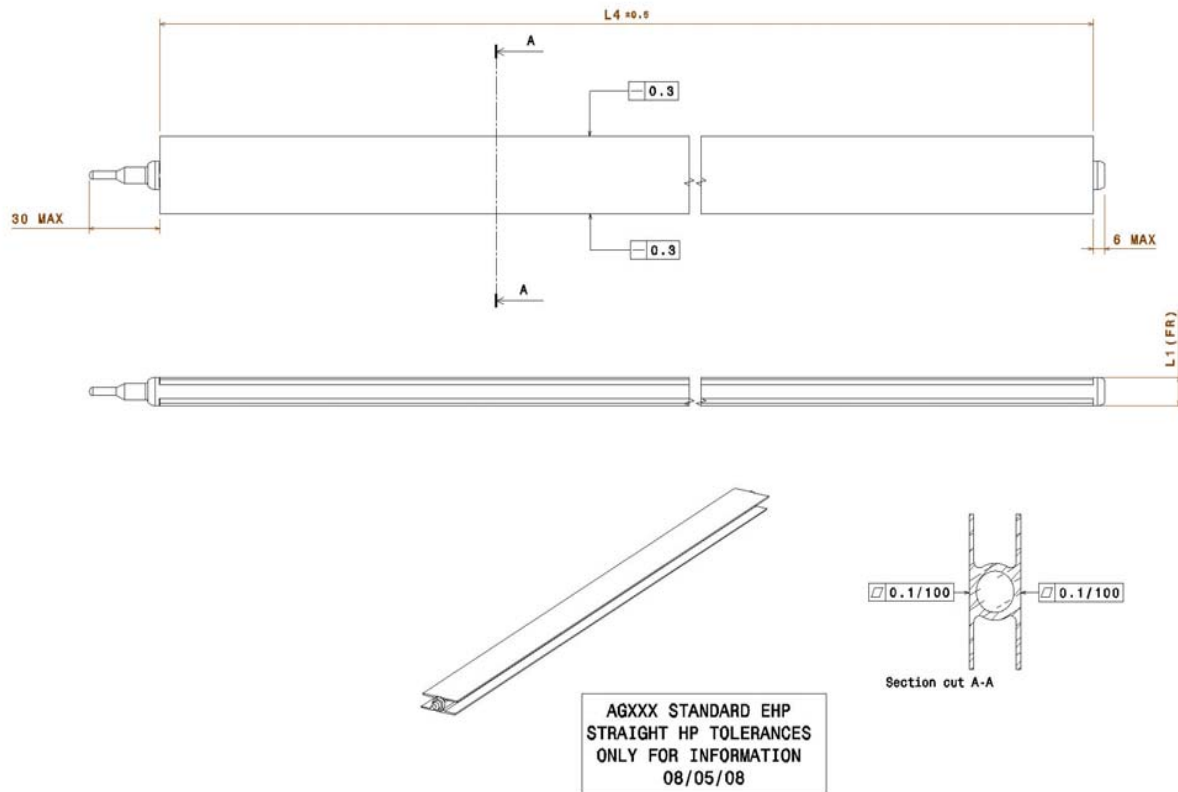


Figure 9-18: HP Profile Tolerances (cont.)

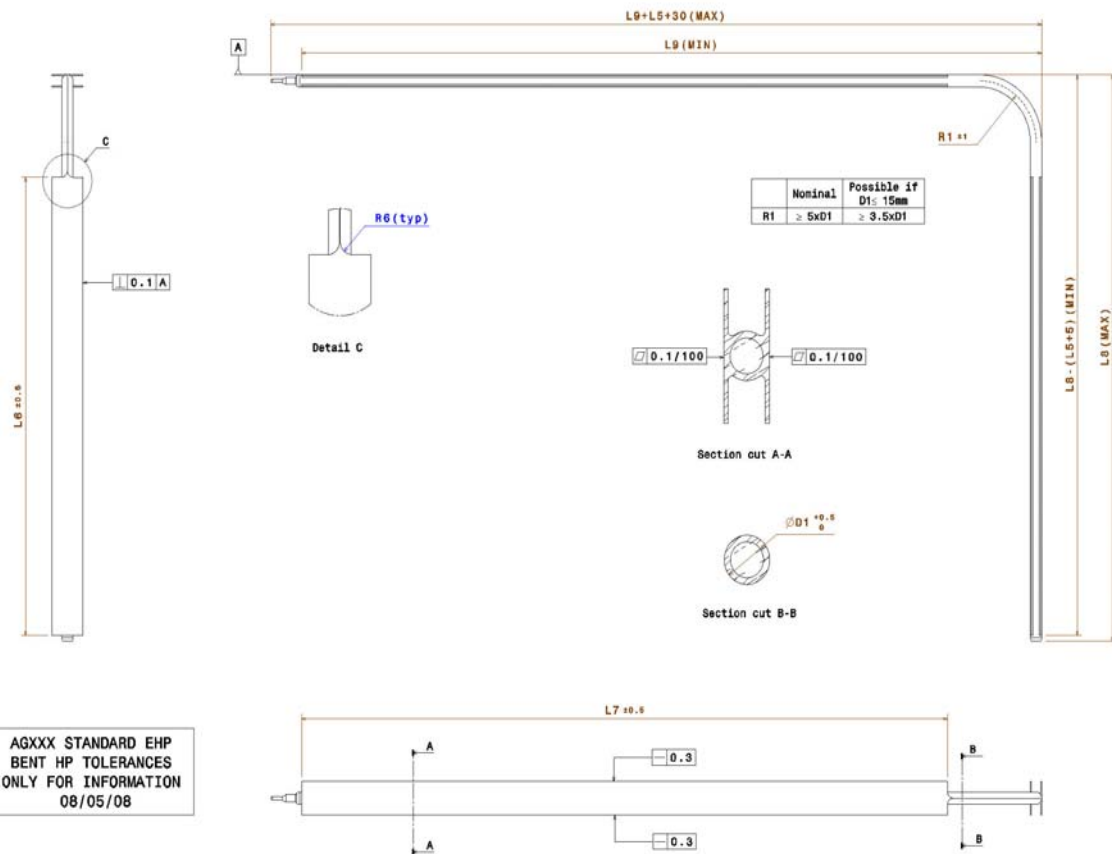


Figure 9-19: HP Profile Tolerances (cont.)

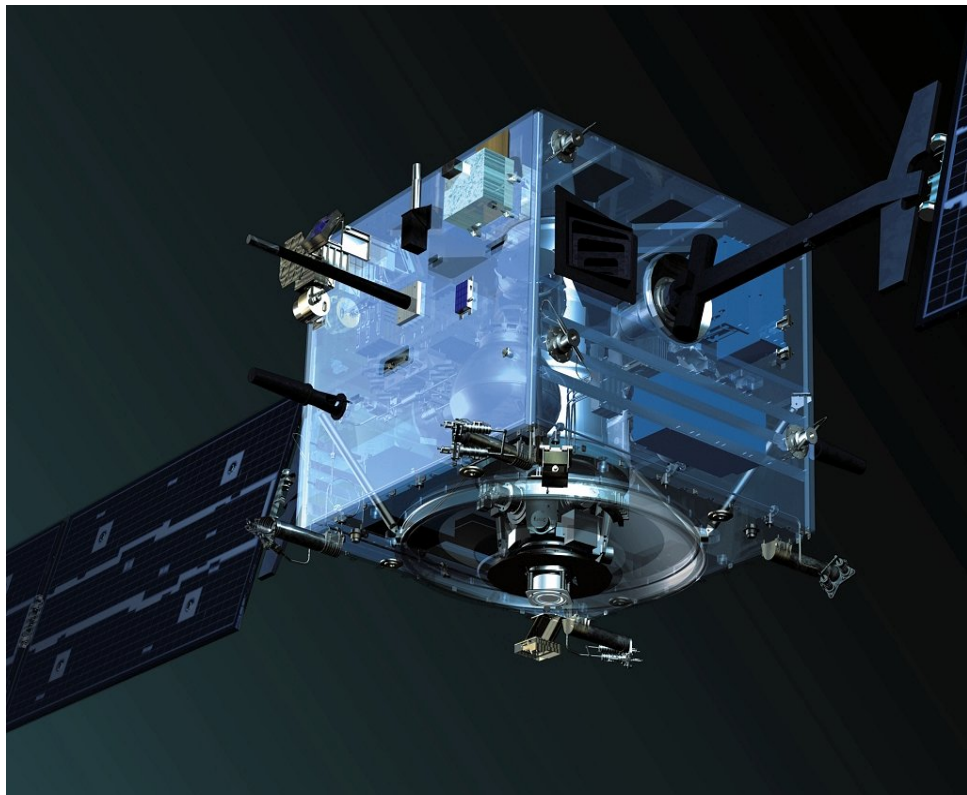


Figure 9-20: ESA SMART 1 with HP

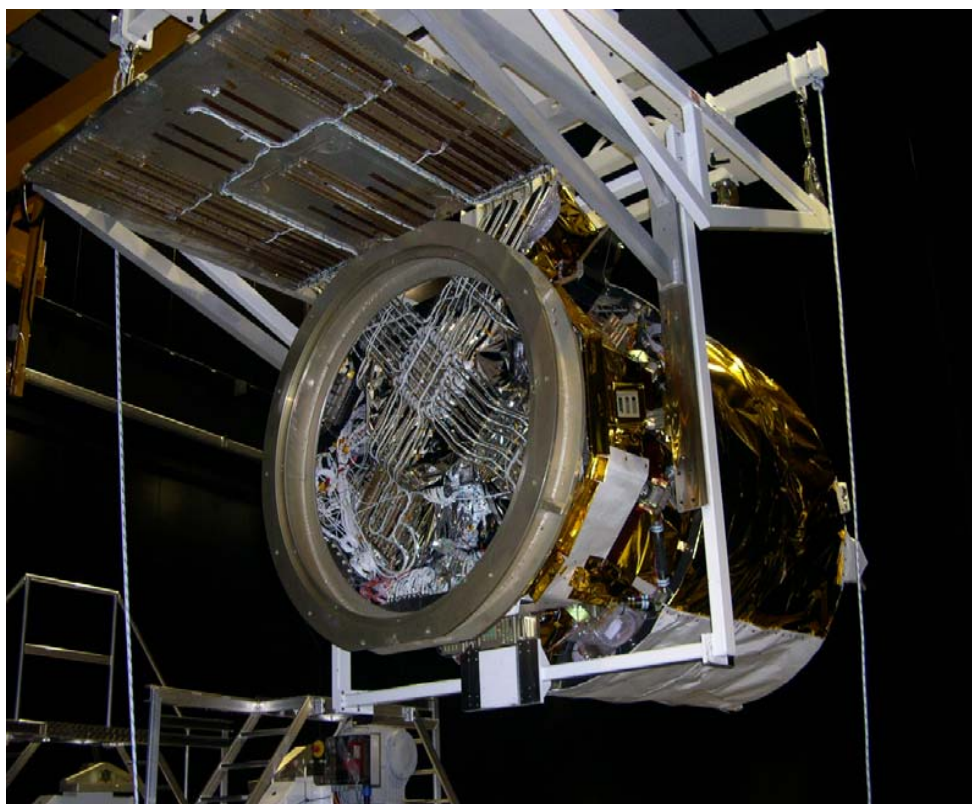


Figure 9-21: ESA AEOLUS – ALADIN instrument with HP network

9.2.2 STAINLESS STEEL HEAT PIPES. This part deals with the products from Technical Data Sheet n° 1B: EHP Stainless Steel

Heat Pipes dia 9.5mm.

Types: Constant Conductance Heat Pipe – Variable Conductance Heat Pipes

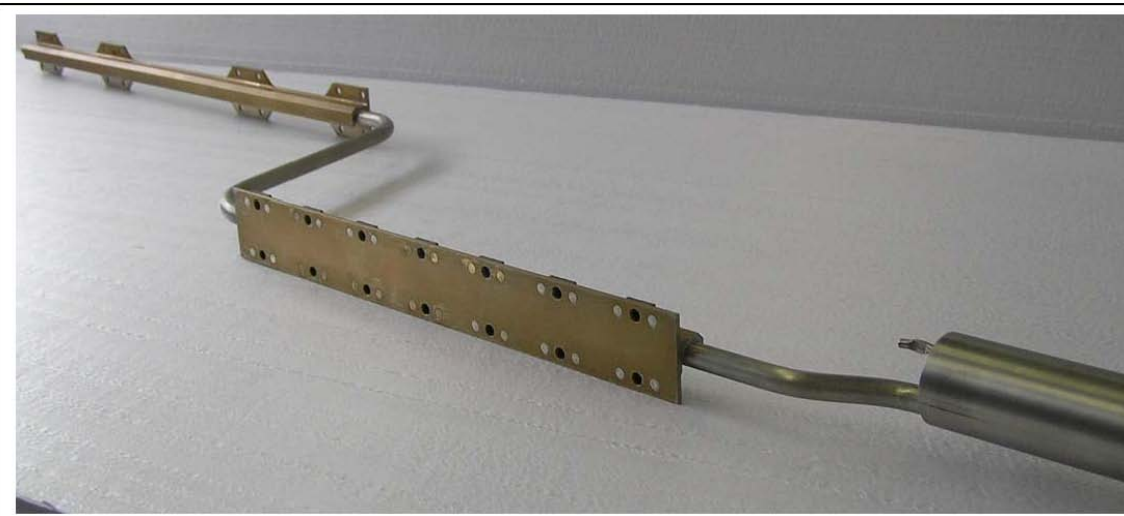


Figure 9-22: Constant Conductance Heat Pipe

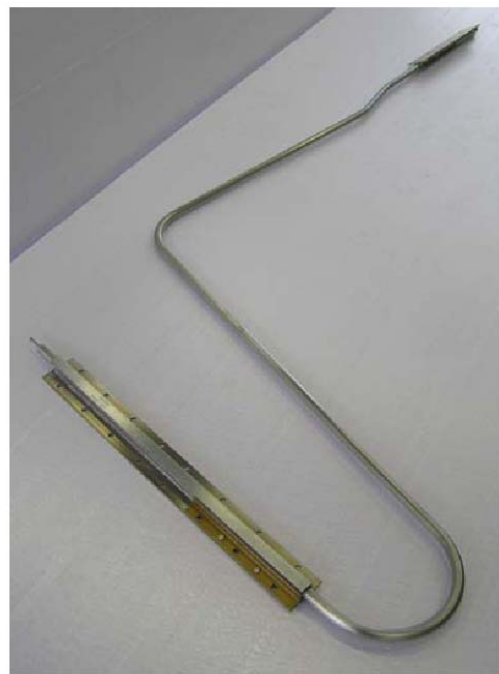
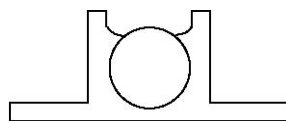


Figure 9-23: Variable Conductance Heat Pipe

Interface: direct circular shape or Brazed aluminium saddle (shape according to customer need).

U-shape



C-Shape H-Shape

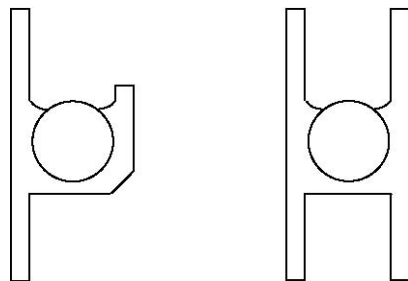


Figure 9-24: Heat Pipe Profiles examples Table 9.2-3. Stainless Steel Heat Pipes types.

Table 9-8: Stainless Steel Heat Pipes types

HEAT PIPE	
TYPE	Improved A95
CCHP/VCHP	Both
Artery/Screen-wicked/Groove	Screen-wicked
Working fluid	High purity Ammonia
GEOMETRICAL DATA	
Body	9.5 mm
O.D.	8.5 mm
I.D.	3 m
Maximum length	40 mm
Minimum bending radius	SS 321
Material	SS 321 – shape and size according to customer need and working conditions
Reservoir	
Wick	Multilayer screen mesh
Configuration Material	SS 316
General	160 g/m, (without saddle)
Mass	Circular body or Aluminium saddles (interface)

HEAT PIPE	
Interface	according to customer design,)
PERFORMANCES	
Q_{\max} (20°C)	> 100 W/m
Tilt _{max} at 50 % Q_{\max}	> 10 mm
bending	Included in performance
K_{evap} (20°C)	> 1.2 kW/.m ² K (\approx 0.4 W/cm ²) > 2.7 kW/.m ² K (\approx 1.3 W/cm ²)
K_{cond} (20°C)	> 2 kW/.m ² K (saddle I/F, C-shape)
Max radial flux density	> 4 W/cm ² (Condenser saddle I/F) > 8 W/cm ² (Evaporator saddle I/F)
Operating temperature range	-50°C to +80°C
Non Operating temperature range	-130°C to +130°C
Maximum storage temperature	110°C
Proof Pressure / temperature	110 bar / 130°C
Burst pressure / temperature	> 166 bar / 156°C (tested: > 215 bar)
Introduced working fluid quantity	16 g/m
VCHP mode	Control of equipment temperature down to $\pm 0.4^\circ\text{C}$
Thermal / Pressure cycling	Qualified
Mechanical	Qualified wrt sinus, random, pyro and shock test
OTHER	ESA Qualification according to PSS49 (1988) 10 years without any degradation (performance NCG, ...) 20 years without any degradation (performance NCG, ...)
Qualification	
Life testing (ground)	
Storage (ground – at CNES)	
Flight Experience	<ul style="list-style-type: none"> • No degradation of performance between 1-g and 0-G • More than 10 years flight without any degradation



Figure 9-25: “*Thank to 40 state-of-the art variable conductance heat pipes located in the avionics bay the ATV is able to carry away the heat and release the energy directly into space or, otherwise, to warm up other parts in a very economic fashion*”
Astrium – ESA “Jules Verne goes hot and cold” – Successful achievement of the Qualification Thermal Test campaign – 14 Dec 2006.

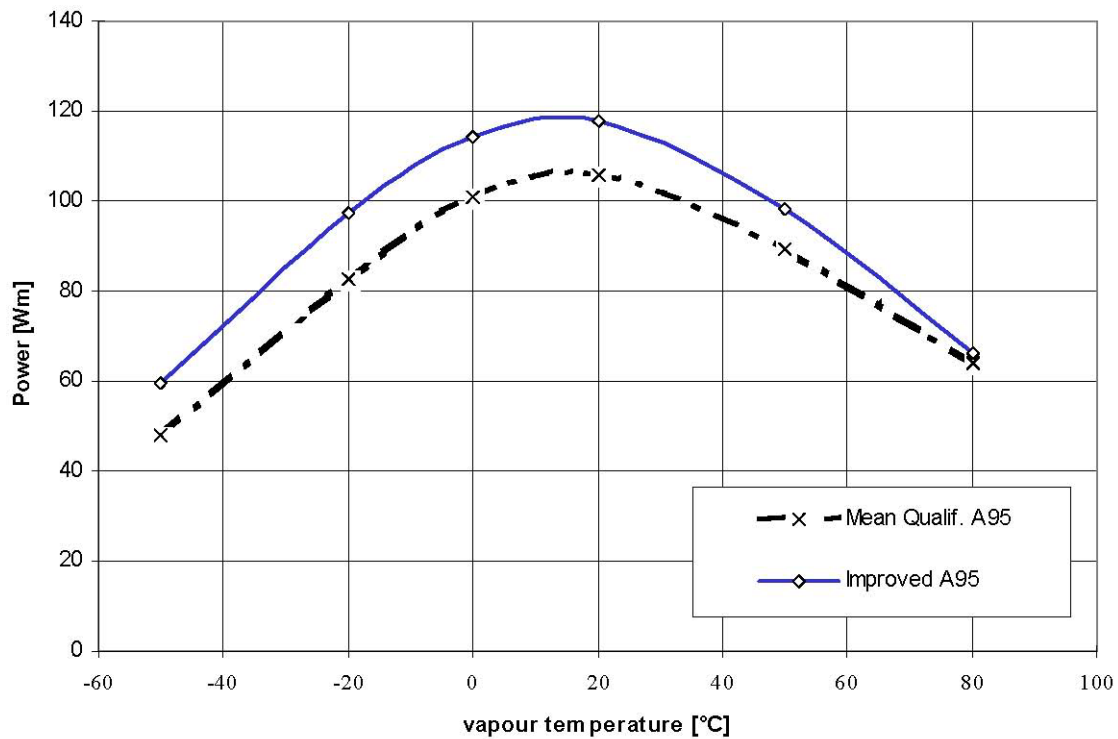


Figure 9-26: Stainless Steel HP Performance curves

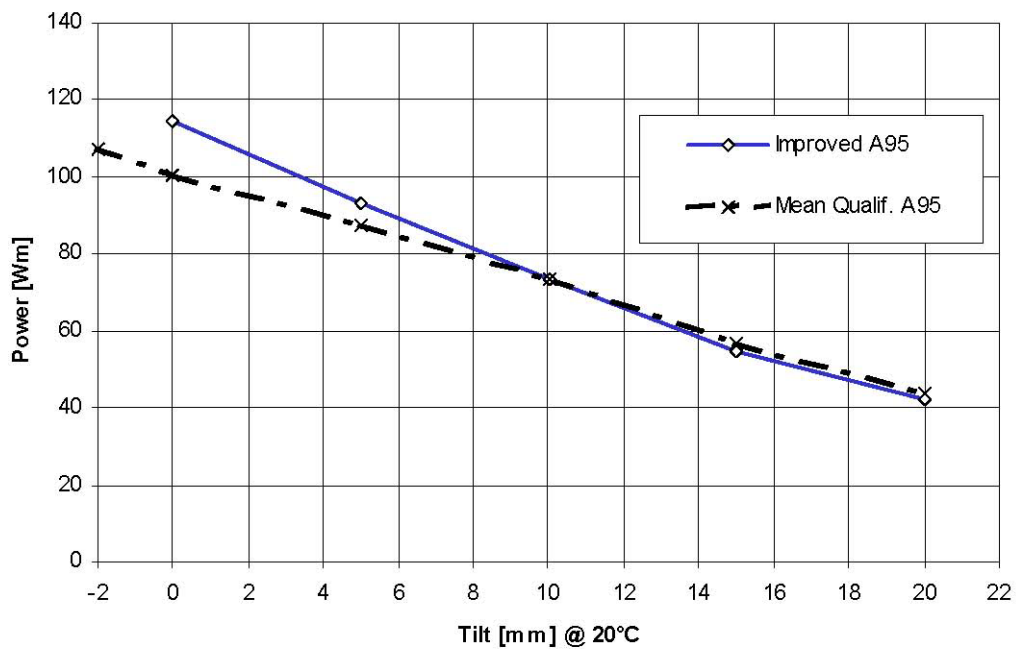


Figure 9-27: Stainless Steel HP Performance curves (cont.)

9.3 Iberespacio

9.3.1 Axial Grooved Heat Pipes

A Heat Pipe is a two phase (liquid-vapor) flow heat transfer device made of a tube with a capillary structure and partly filled with a fluid. The heat transfer is achieved by the fluid evaporation / condensation. The fluid circulation is due to capillary forces.

The Axial Grooved Heat Pipes capillary structure is made of extruded aluminium alloy. External coating according to customer requirements. New profiles upon customer request.



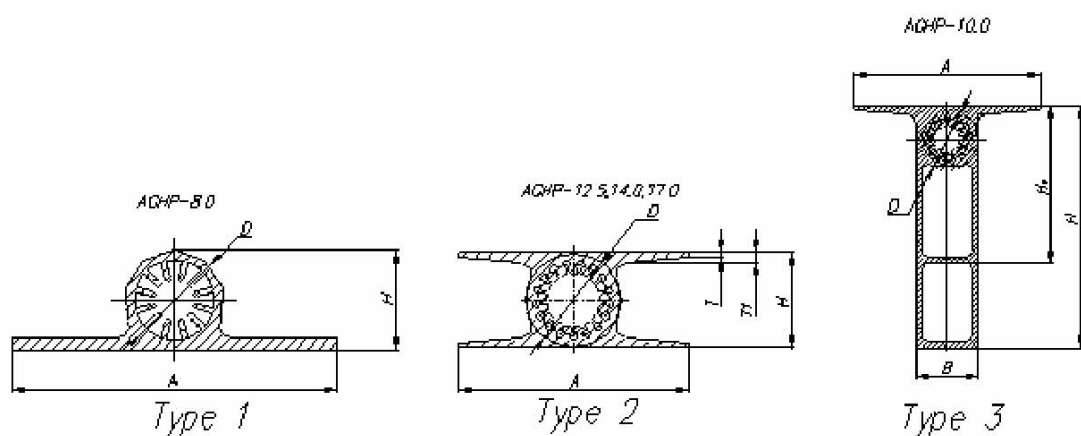
Figure 9-28: Axial Grooved HP profiles

Technical characteristics:

- Constant Conductance Heat Pipes
- Aluminum alloy extrusions
- Working fluids: High purified ammonia, propylene, ethane, methane, nitrogen, toluene
- From 1D to 3D shaping
- 25 years life time from the moment of charging

Table 9-9: Geometrical Parameters

	$\phi 8 \text{ mm}$	$\phi 10 \text{ mm}$	$\phi 12.5 \text{ mm}$	$\phi 14 \text{ mm}$	$\phi 17 \text{ mm}$	$\phi 20 \text{ mm}$
A	26	30	30	30	30	30
H	8,0	39,0	12,5	14,0	17,0	20
B	-	10,0	-	-	-	-
D	8,0	10,0	12,5	13,0	17,0	19,5
H1	-	25,4	-	-	-	-
T	1,0	1,25	1,25	1,25	1,25	1,25
T1	1,0	0,65	0,6/1,25	1,25	1,25	0,8
Mass g/m	140	412	334	417	491	548

**Figure 9-29: Axial Grooved HP profiles drawings**

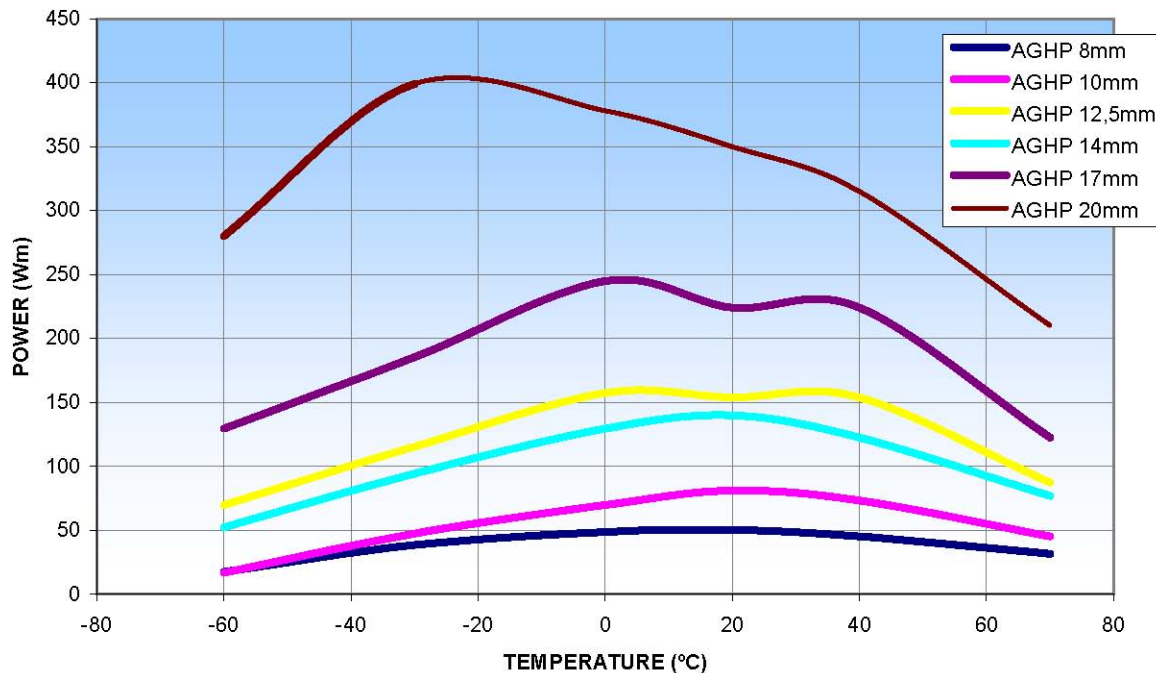


Figure 9-30: Dependence of AGHP Heat Transfer Capacity on Working Fluid (Ammonia)

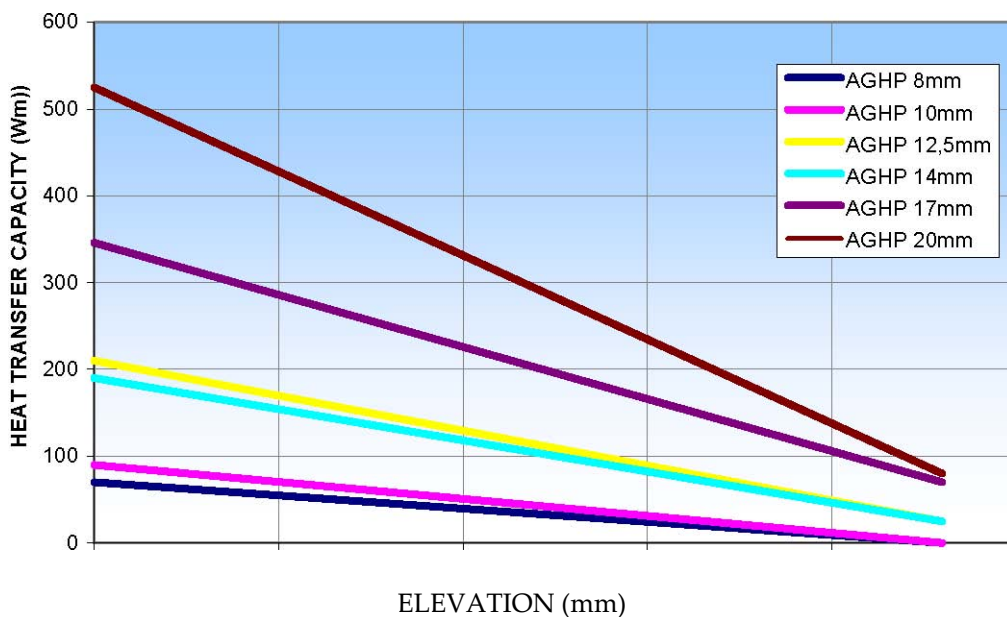


Figure 9-31: Influence of tilt angle on AGHP maximum Heat Transfer Capacity at 20°C

9.3.2 Arterial Heat Pipes

The Arterial Heat Pipes capillary structure is made of machined stainless steel and an artery for flow separation.

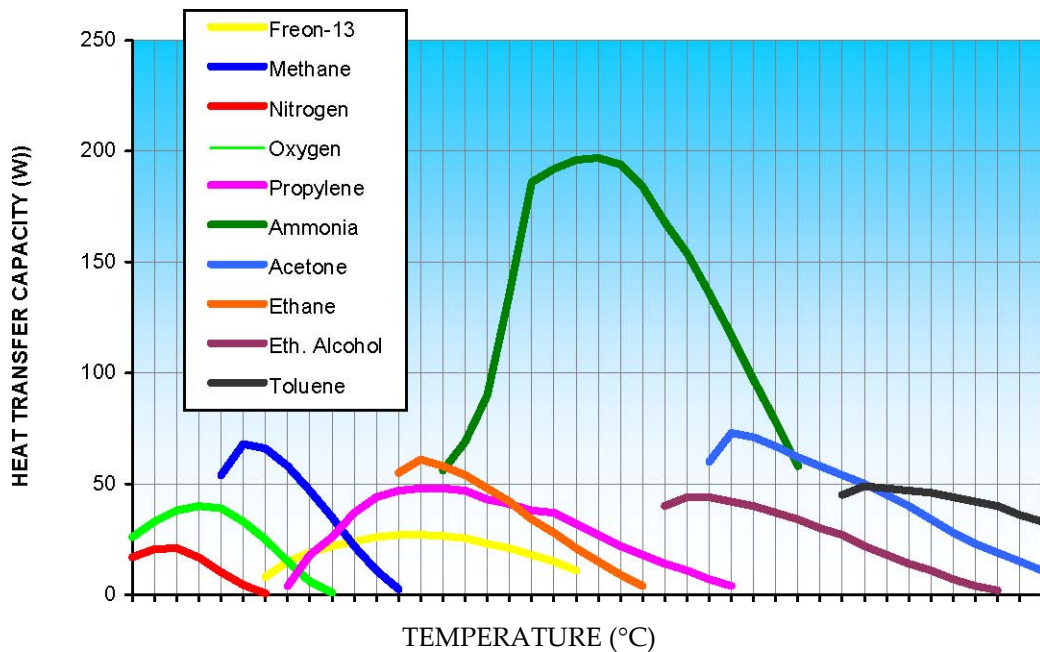


Figure 9-32: Thermal performance of Arterial HP with different working fluids

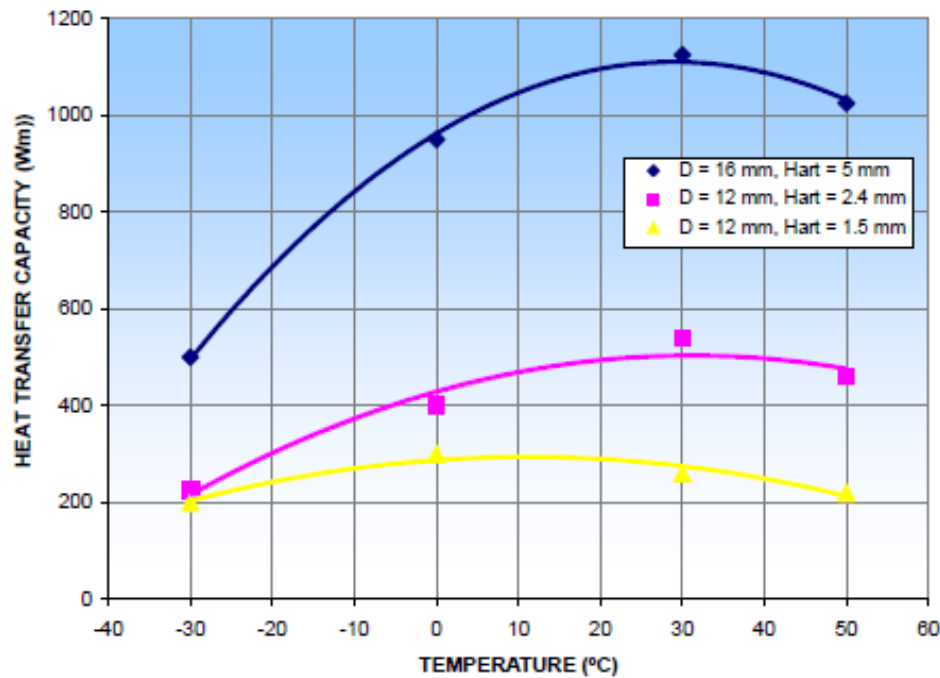


Figure 9-33: Experimental data for Arterial HP with ammonia

Technical characteristics:

- Diode heat pipes, flexible heat pipes, variable conductance heat pipes, cryogenic heat pipes, high temperature heat pipes and routing heat pipes
- Working fluids: High purified ammonia, propylene, ethane, ethanol, methane, nitrogen, ace complicated tone, toluene, oxygen, Freon-13
- From 1D to 3D shaping
- Body and capillary wick material: stainless steel
- Contact surface of saddles material: Al alloys (including low CTE), Cu
- 25 years life time from the moment of charging

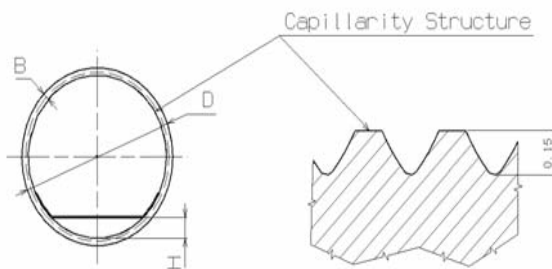


Figure 9-34: Arterial HP profile schematics



Figure 9-35: Arterial HP typical configurations



Figure 9-36: Arterial HP for rotator application. Length 2400 mm. Power 150 W.

9.4 Thales Alenia Space

9.4.1 Technical Description

- Type: Constant Conductance Heat Pipes
- Construction: Axially grooved heat pipes
- Material: Aluminium 6063
- Working fluid: Ultra high purity ammonia (99.9995% minimum)
- Operating Temperature Range: -60/+90°
- ThalesAlenia Space catalog: 5 mono-core heat pipes + 2 dual core heat pipes
- Heat Input: Up to 10 W/cm²
- Life expectancy:
 - Storage: 10 years
 - In Orbit: 20 years
- Profile Geometry:
 - For external and embedded applications
 - Diameter from 11mm to 22mm
 - Length up to 4m
- Heat transport Capability at 0g (minimum):

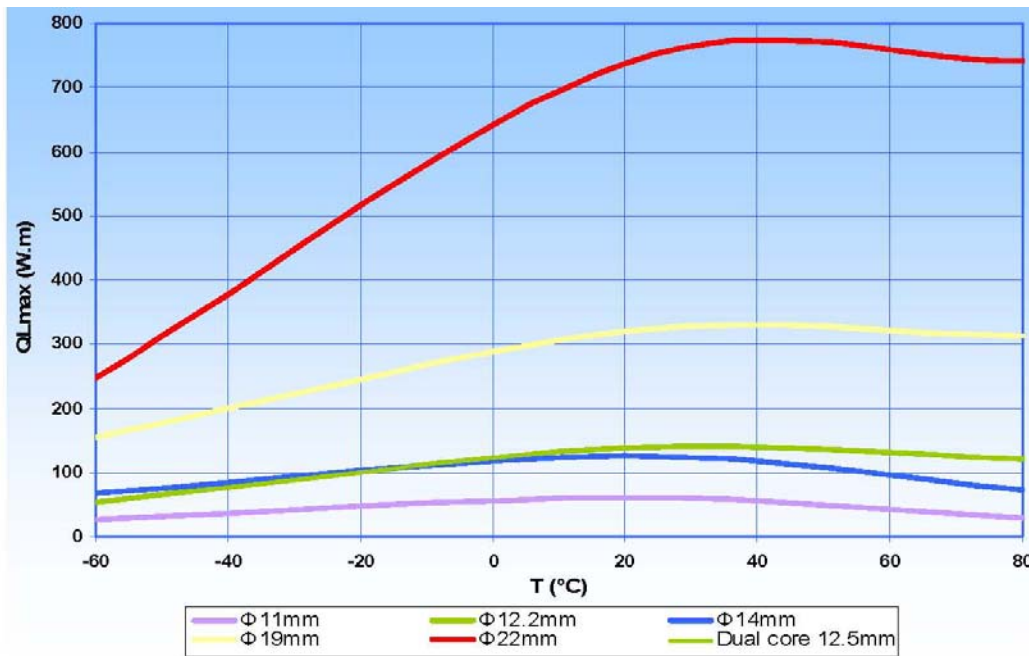


Figure 9-37: 0g guaranteed heat transport capability for ThalesAlenia Space Heat Pipes

Nota: Mono-core Ø12.2 and the two dual core heat pipes have the same heat transport capability because these heat pipes have the same internal geometry. The second pipe of dual core heat pipes is considered as a redundant pipe (non operating in nominal functioning).

- Heat transfer coefficient:
 - At evaporator, > 60 W/mK
 - At condenser, > 100 W/mK

Table 9-10: Thermal Performances of ThalesAlenia Space Heat Pipes
 (*): QL_{max} 6mm guaranteed

Diameter	Ø11	Ø12.2	Ø14	Ø19	Ø22	Dual core Ø 12.5 H29	Dual core Ø 12.5 H shape
QL _{max} 0g guaranteed (20% security margin)	T=80°	28	116	75	312	725	116
	T=20°	62	140	125	320	740	140
QL _{max} 4mm guaranteed (20% security margin)	T=80°	23	74	55	225	450(*)	74
	T=20°	50	96	105	245	530(*)	96
Density (W/cm ²)		6.6	5.3	10	6	7.7	>10
							>10

Table 9-11: Mass of ThalesAlenia Space Heat Pipes

Diameter	$\varnothing 11$	$\varnothing 12.2$	$\varnothing 14$	$\varnothing 19$	$\varnothing 22$	Dual core $\varnothing 12.5$ H29	Dual core $\varnothing 12.5$ H shape
Mass (g/m)	348	339	395	564	668	From 465 to 586	From 465 to 519 (*)

This mass per length unit includes ammonia end caps and aluminium profile without flange machining.

(*): after flange machining

9.4.2 External Geometries

Mono-core heat pipes:

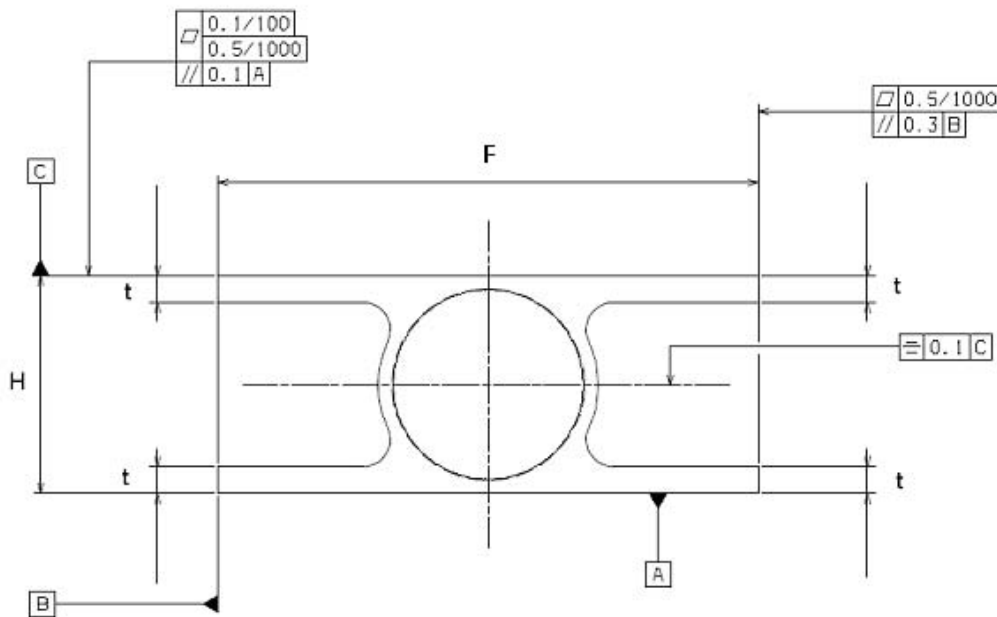


Figure 9-38: Mono-core heat pipe profile

Dual core heat pipes:

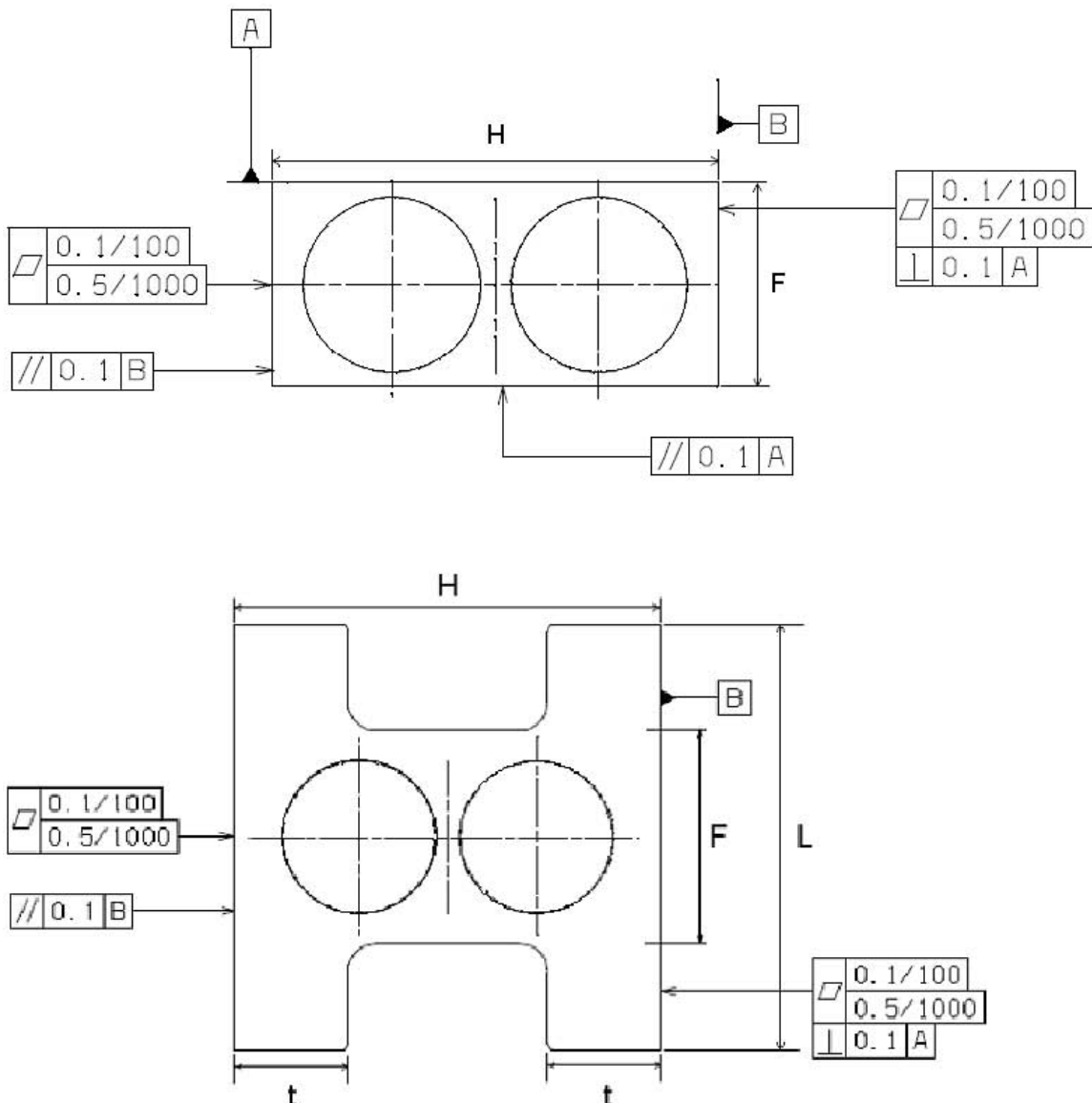


Figure 9-39: Dual-core heat pipe profiles

Table 9-12: External geometries of ThalesAlenia Space Heat Pipes

Diameter	$\varnothing 11$	$\varnothing 12.2$	$\varnothing 14$	$\varnothing 19$	$\varnothing 22$	Dual core $\varnothing 12.5$ H29	Dual core $\varnothing 12.5$ H shape
F (mm)	30	30	30	38	39	12.5	12.5
H (mm)	11	12.2	14	19	22	From 25.4 to 29	From 25.4 to 27
t (mm)	1.5	1.5	1.5	1.5	1.5	/	From 7.2 to 8
L (mm)	/	/	/	/	/	/	30

Possibility to bend these heat pipes.

Standard bending radius = 5 times heat pipe diameter

Necessity to have straight parts before and after the bent section of heat pipe.

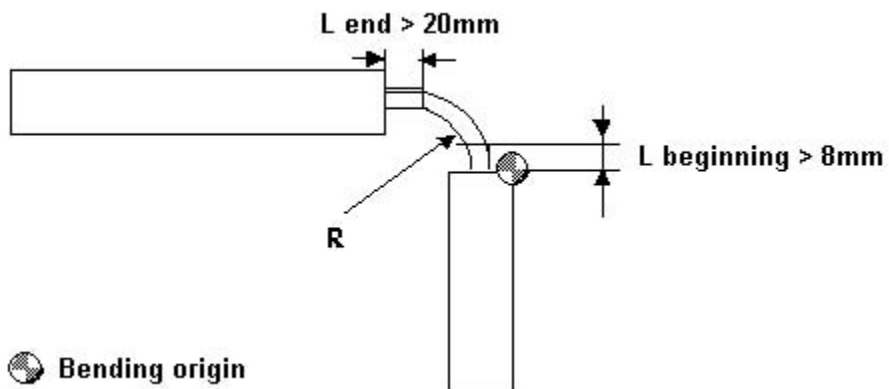


Figure 9-40: Minimal dimensions of straight parts for $\varnothing 12.2$ bent heat pipe

Note: the bending origin is located on the shortest straight side of heat pipe.

10

Cryogenic heat pipes

10.1 General

Cryogenic Heat Pipes operate in the temperature range from 2 K to 200 K.

After Haskin (1967) [33] reported the work on a Nitrogen heat pipe to control the temperature of an infrared detector, the investigations on the performance and use of cryogenic heat pipes have steadily increased.

Cryogenic heat pipes can be applied in space mainly for thermal control of optical surfaces or of infrared detector systems. That application can be achieved in several ways, namely:

1. Coupling of optical packages or of one or several detectors to passive or active coolers.
2. Isothermalization of radiant coolers.
3. Cryodiode application for connection to a radiator which periodically gets warm.
4. Hybrid cooler (solid-liquid coolers - radiant coolers) system.

10.2 Working fluids

The use of cryogenic fluids in heat pipes presents several features that do not appear in ambient or high temperature heat pipes. These features and possible consequences are summarized in Table 10-1.

Table 10-1: Main Features of Cryogenic Fluids in Heat Pipes, Consequences

Features	Consequences	Comments
Low operating temperature.	Cooling the condenser could be problematic. Difficult testing. Start-up from the supercritical state presents unique problems.	
Narrow operating temperature range.		Operating temperature range lies between the triple point and the critical temperature. See ECSS-E-HB-31-01 Part 14, Table 8-1, clause 8.1.1 .
Highly temperature-dependent fluid	Large variations of the Figure of Merit, N .	For the definition of N , ECSS-E-HB-31-01 Part 11, see Clause 5-1 .

Features	Consequences	Comments
properties.		
Temperature gaps where no suitable working fluid exist.		See Figure 10-1. Alternative working fluids are being investigated. Nitrogen used in most cryogenic heat pipes.
Very low values of the Figure of Merit, N .	Very limited heat transfer capability. Extreme sensitivity to gravity. Difficult ground testing of devices optimized for 0-g operation.	N for typical cryogenic working fluids is given in Figure 10-2. $(Q_{leff})_{max}$ for cryogenic heat pipes is given in Figure 10-16, clause 10.9.
Very low thermal conductivity.	Limited radial evaporator heat flux. Less than 10^4 W.m^{-2} .	
Boiling may occur with superheats up to 10 K.		
Increased compatibility problems.		See Table 6-2, ECSS-E-HB-31-01 Part 14, clause 6.4.6.4 ; Tables 9-1 through 9-4, ECSS-E-HB-31-01 Part 14, clause 9.2 ; and clause 9.3.2.
High vapour pressures during storage.	Structural problems. Increased wall thickness results in increased wall and wick thermal conductance and in a reduction of the overall performance.	See ECSS-E-HB-31-01 Part 14, Table 8-1 and associated figures in clause 8.1.1. Expansion reservoirs could be used (Mathieu (1982) [54]).

NOTE Prepared by the compiler after Peterson & Compagna (1986) [66].

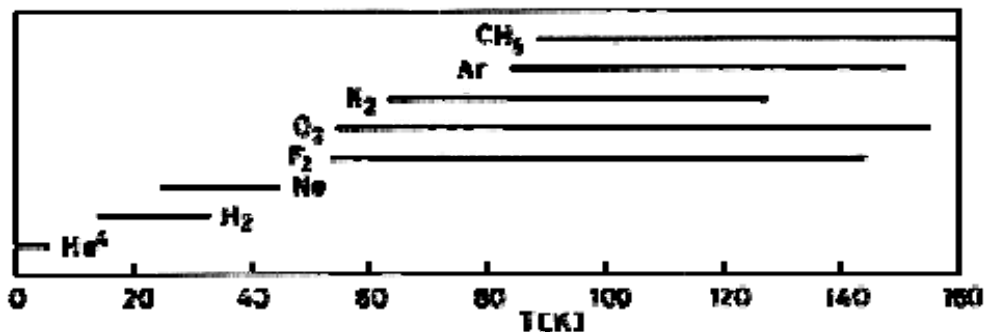


Figure 10-1: Operating temperature range for cryogenic working fluids. Data from [ECSS-E-HB-31-01 Part 14, Table 8-1, clause 8.1.1](#). For fluorine: melting point, $T = 53,5 \text{ K}$, critical point, $T = 144 \text{ K}$.

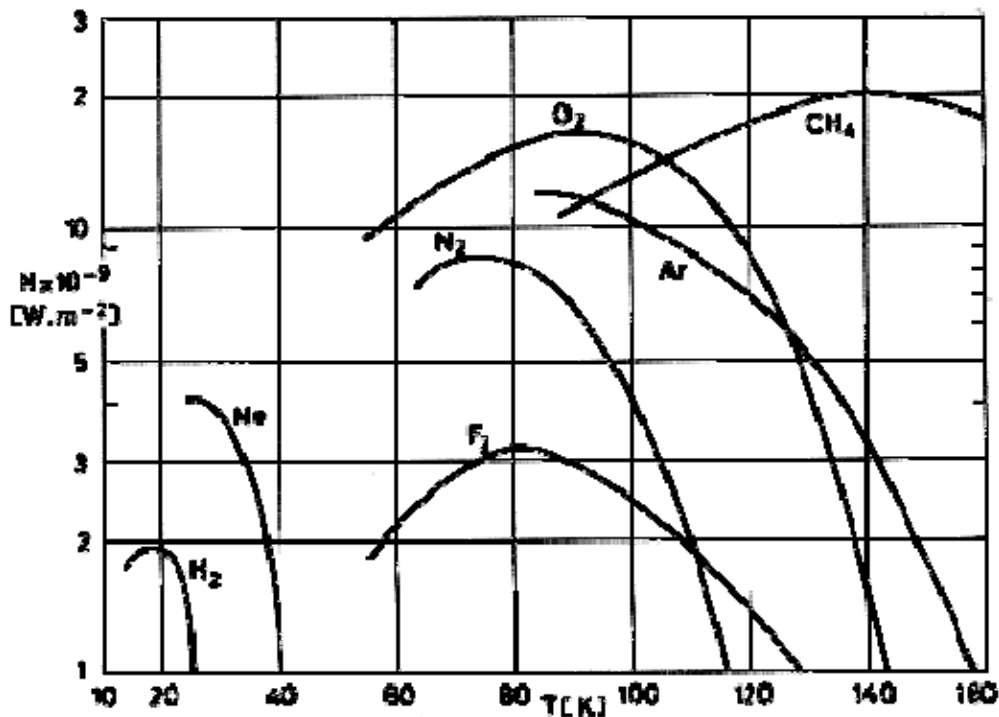


Figure 10-2: Figure of Merit, N , as a function of temperature, T , for several cryogenic working fluids. Compare with Figure 6-8, clause 6.3. Replotted after Chi & Cygnarowicz (1970) [15].

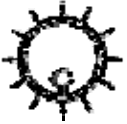
10.3 Wicks

Working fluids for cryogenic heat pipes exhibit low values of surface tension and latent heat of vaporization and large values of the fluid dynamic viscosity, this results in heat pipes of very limited heat transfer capability and high sensitivity to acceleration fields. It is important to optimize the wick geometry in order to achieve maximum heat transfer rate, Q , for given effective length, l_{eff} , and inner diameter, D_i , of the pipe in a given acceleration field.

Traditional wick structures were already introduced in Clause 5. Table 5-2, shows a number of room temperature heat pipe wick structures many of which are being considered for use in the cryogenic range. The table is divided into two parts, one enclosing current technology structures and the other enclosing advanced concepts.

Table 10-2: Wicking Structures. Current Technology

WICK DESIGN	Heat Transport Factor ($Q \cdot l_{eff}$) [W.m] Water, $D_v = 0,0127$ m	HISTORY/STATUS
	404	Developed by TRW. Version with side arteries used in CTS (Launched in 1976).

WICK DESIGN	Heat Transport Factor (Q_{eff}) [W.m] Water, $D_v = 0,0127$ m	HISTORY/STATUS
PERFORATED ARRESTOR 	711	Early development by McDonnell Douglas and Dynatherm. 8 years completed in orbit in 1980 (OAO-C).
SPRAL ARRESTOR 	762	Developed by Grumman. 8 years completed in orbit in 1980 (OAO-C).
TOOTHED ARRESTOR 	1524	Developed by Grumman. Used on NASA-JSC's Modular Radiator.
AXIAL GROOVE 	2150 (NH_3 , $D_v = 0,009$ m, $(Q_{eff}) = 270$ W.m, $l_{eff} = 0,85$ m)	Developed by ERNO GmbH, Germany, for use in Spacelab Missions.
COILED WALL ARRESTOR 	2000-10000	Being developed by AFWAL. Demonstrated 1600 W.m, $D_v = 0,0134$ m $l_{eff} = 1$ m
ZERODURING TUBE 	12000-100000	Developed by Grumman. Demonstrated 12880 W.m (NH_3 , $D_v = 0,0134$ m, $(Q_{eff}) = 3220$ W.m, $q = 134 \times 10^3$ W.m ⁻² , $l_{eff} = 4,6$ m)
CHAMFERED U-TUBE 		Being developed by Rockwell.

NOTE From Peterson & Compagna (1986) [66].

Results of tests on many heat pipes, with different wick structures, designed to operate in the cryogenic temperature range are summarized in Table 10-4, clause 10.9. New types of wicks are discussed in the following clauses.

10.3.1 Lab wicks

A type of wick specifically designed for use in cryogenic heat pipes is the slab wick (Sherman & Brennan (1974) [86]).

The slab wick, through which the fluid transport is achieved, is placed near a diametral plane of the tube. A peripheral secondary distribution wick is used to wet the tube wall but does not affect the transport capability of the system. Both wicks are linked in the evaporator and condenser sections.

The slab wick is optimized on the basis of projected requirements (Q_{max}) and should provide meaningful and reliable 1-g test results.

10.3.2 Tunnel artery

A tunnel artery has been also used in cryogenic heat pipes (Dominguez & Kossen (1973) [20]).

In this concept a tunnel or hollow core is completely enclosed by a composite wick structure.

The composite wick (excluding the tunnel) has fine capillary passages to provide self-filling by surface tension forces under 1-g conditions and transport some minimum required heat flow even if the tunnel is completely filled with liquid.

When the tunnel is empty it contains saturated vapor at a pressure corresponding to the temperature of the enclosing liquid surface.

When a heat load is applied, the temperature in the main vapor space exceeds that of the liquid surrounding the tunnel and, then, the main vapor pressure exceeds the pressure in the tunnel. The difference in pressures causes the liquid to flow into the tunnel filling it (pressure or Clapeyron priming).

By use of this powerful filling mechanism it is possible in a 1-g field to fill a tunnel having much larger cross sectional dimensions than could be filled by surface tension alone and, on the other hand, the single, large cross section provides much higher heat transfer capability than could be obtained from a multiplicity of passages having the same total cross-sectional area.

The tunnel wick is connected to the tube wall by means of webs which position the artery and provide a liquid flow path between the artery and the wall grooves. The internal wall surfaces in the evaporator and condenser positions of the heat pipe are provided with fine circumferential grooves designed to minimize temperature drops at the highest required heat transfer conditions.

10.3.3 Graded-porosity wicks

Homogeneous wicks exhibit poor performances. In a composite slab, the outer layer, a fine mesh screen, provides the capillary pumping, while the pore size of the more permeable inner core is determined by the less stringent self priming requirement. This is the so-called radial porosity grading which was already discussed in clause 5.3.

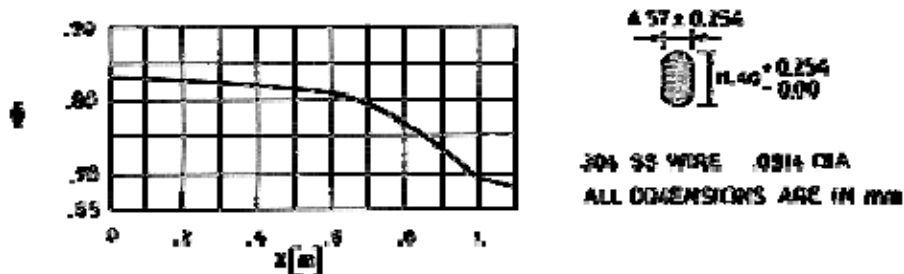
When the porosity of a wick is uniform along the heat pipe length and is determined by the high capillary pressure requirements at the evaporator end under maximum heat load (see Clause 7.2.1.1),

the pore radius of the wick and, thus, the wick permeability results to be unnecessarily low (and the wick porosity unnecessarily high) everywhere except at the evaporator end.

By "grading" the porosity along the wick length (axial porosity grading), the capillary pressure is only as high as required to sustain the local vapor-liquid pressure difference and, thus, the permeability is as high as possible everywhere along the length of the wick.

Increases in performance with graded-porosity wicks larger than 100 % as compared with uniform porosity wicks have been predicted, although the experiments do not fulfill these expectations.

Graded-porosity slab wicks heat pipes for use with cryogenic fluids have been manufactured and tested (Groll, Pittman & Eninger (1976) [30]). The main features and performance of these heat pipes are summarized in Table 10-4, clause 10.9. The axial distribution of porosity of a graded-porosity wick is shown in Figure 10-3.



Note: non-si units are used in this figure

Figure 10-3: Axial distribution of porosity, Φ , and cross section of a graded-porosity slab wick. From Groll, Pittman & Eninger (1976) [30].

10.4 Operating limits

Capillary and boiling are the only of those operating limits quoted in clause 7.2, which are relevant to cryogenic heat pipes. This is so because these heat pipes exhibit both insufficient capillary pumping ability and boiling in the capillary structure of the evaporator.

10.4.1 Capillary heat transfer limit

The capillary heat transfer limit of cryogenic heat pipes using mesh screen wicks presents several particular features which will be discussed in this clause.

For a mesh-screen-wicked heat pipe under steady state conditions in a gravitational field, the equation giving the heat transfer rate has been written down in clause 7.2.1.1, as follows:

$$1 - \frac{l \sin \varphi}{H} = \frac{Q}{Q_{\max}} \left[1 + 32K \frac{D_i^2 - D_v^2}{D_v^4} \frac{\nu_v}{\nu_l} \right] \quad [10-1]$$

Note: non-si units are used in this figure

where the maximum heat transfer rate, Q_{\max} , is given by the following expression:

$$Q_{\max} = N \frac{\pi}{2} \frac{K(D_i^2 - D_v^2)}{r_c l_{eff}} \quad [10-2]$$

Note: non-si units are used in this figure

In the case of heat pipes operating at room or high temperatures and when the vapor flow passage is much larger than the wick thickness, vapor and hydrostatic pressure drops are negligible and the liquid pressure drop alone balances the capillary pumping pressure. In that case:

$$Q = Q_{\max}$$

This is the case considered in clause 7.2.1.1.

Neglecting vapor and hydrostatic pressure drop can no longer be justified for cryogenic heat pipes because of the following two reasons:

1. Surface tension of cryogenic fluids is normally low, and consequently so is the equilibrium capillary height, H . Thus $(l/H)\sin\varphi$ in Eq. [10-1] is no longer negligible compared to unity. This results in the extreme sensitivity of cryogenic heat pipe performance to gravity level, which was already mentioned in Table 10-1, Clause 10.2.
2. The vapor to liquid kinematic viscosity ratio, ν_v/ν_l , increases when the temperature decreases. This can be seen in Table 10-3, where ν_v/ν_l at critical conditions has been compared with that at the triple point. One to three orders of magnitude increase results for typical working fluids of cryogenic heat pipes.

Table 10-3: Evolution of Vapor to Liquid Kinematic Viscosity Ratio over Working Temperature Range ^a

Fluid	Temperature ^b [K]	$\mu_v \times 10^6$ [Pa.s]	ρ_v [kg.m ⁻³]	$\mu_l \times 10^6$ [Pa.s]	ρ_l [kg.m ⁻³]	ν_v / ν_l
NH ₃	Triangle 95,48	7,64 (200 K)	0,0637	407,0 (200K)	733,86	216,25
	Circle 405,45	24,8 (406,15 K)	235	24,8 (406,15 K)	235	1,00
CO ₂	Triangle 216,58	12 (230 K)	13,77	165,0 (230 K)	1178,6	6,26
	Circle 304,21	31,4 (304,16 K)	465	31,4 (304,16 K)	466	1,00
H ₂	Triangle 13,95	0,85 (16 K)	0,1243	20,0 (16 K)	76,91	26,29
	Circle 33,19	3,64 (33,18 K)	30,1	3,64 (33,18 K)	30,1	1,00
He ⁴	Triangle 2,177	1,95 (2,174 K) ^c	1,18	2,78 (2,186 K) ^d	146,22	87,06
	Circle 5,201	1,04 (5,5 K) ^d	69,64 ^d		69,64	
CH ₄	Triangle 90,68	4,09 (100 K)	0,2514	156,3 (100 K)	451,23	47,20
	Circle 190,56	16,5 (190,65 K)	162,2	16,5	162,2	1,00
C ₂ H ₆	Triangle 90,35		45,5x10 ⁻⁶	878,0 (101,2 K) ^e	651,92	
	Circle 305,33	15,60 (312,65 K) ^e	204,5	15,60 (312,65 K) ^e	204,0	1,00
Ne	Triangle 24,56	3,32 (20 K) ^e	4,412	160,0 (25,09 K) ^e	1249,3	6,36
	Circle 44,35		483	27,0 (44,13 K) ^e	483,1	
N ₂	Triangle 63,15	4,40 (65 K)	0,7057	274,0 (65 K)	867,78	20,64
	Circle 126,20	19,1	314,1	19,1	314,0	1,00
O ₂	Triangle 54,36	3,914 ^f	0,0104	619,4 ^f	1306,8	767,87
	Circle 154,58	41,78 (155 K) ^e	436,1	41,78 (155 K) ^e	436,1	1,00
Ar	Triangle 83,80	7,45 (90 K) ^e	4,041	279,8 (85 K) ^e	1415,0	9,32
	Circle 150,73	43,45 (150 K) ^e	535	43,45 (150 K) ^e	535,0	1,00

^a All the data in this table, unless otherwise stated, are from ASHRAE (1985).

^b Triangle: Triple point. Circle: Critical point.

^c From Kutateladze & Borishanskii (1966) [47].

^d From Johnson (1961) [37].

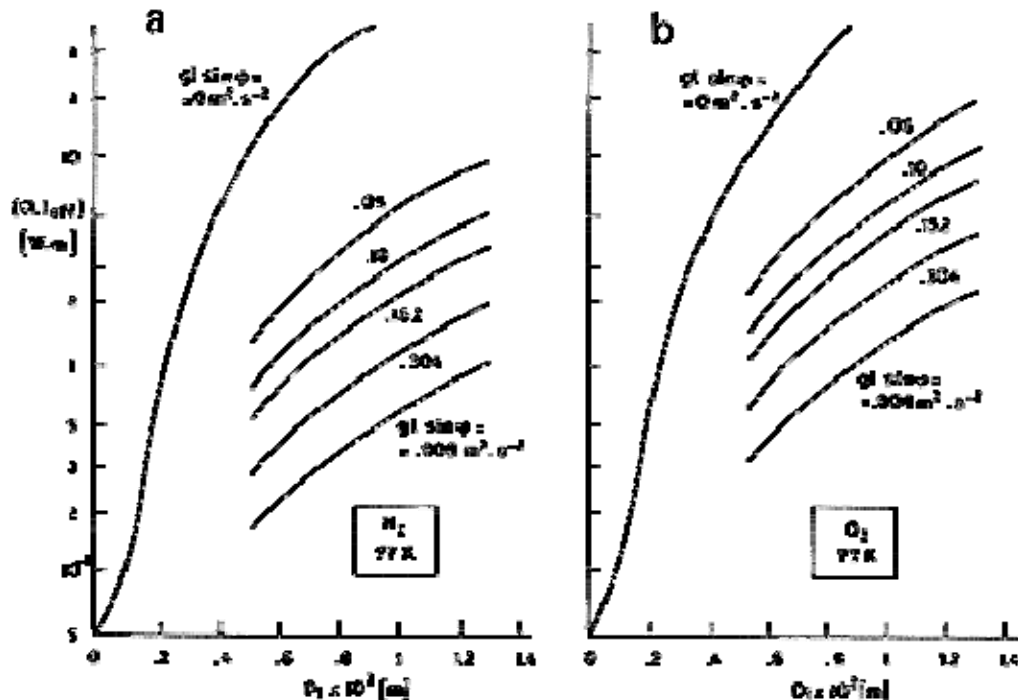
^e From Vargaftik (1975) [94].

^f From Weast (1976) [95].

Gravity level could influence the factor in brackets in the right hand side of Eq. [10-1] in not a straightforward way. For example, it has been shown (Joy (1970) [38]) that optimum pore radii for reduced gravity operation are too large for on-earth operation where increased capillary pumping is required to cope with hydrostatic pressure.

In order to illustrate the influence of gravity level on cryogenic heat pipe performance, Figure 10-4a shows the heat transport factor, ($Q.l_{eff}$), for a Nitrogen heat pipe, which operates at 77 K (the homogeneous wick of which has been optimized in terms of r_c and D_v) as a function of the inner

diameter of the pipe, D_i , and for different gravity levels. Similar results, for oxygen, are shown in Figure 10-4b



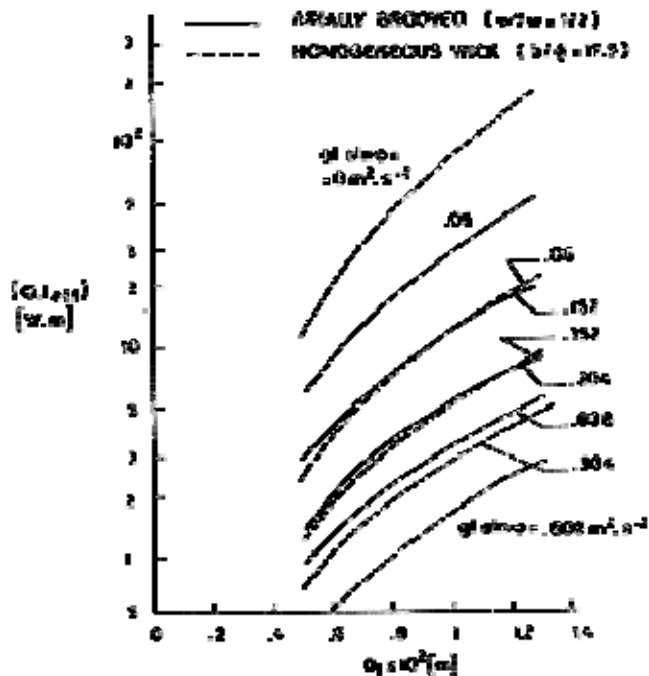
Note: non-si units are used in this figure

Figure 10-4: Maximum heat transport factor, $(Q.l_{eff})$, for a homogeneous wick heat pipe as a function of inner diameter, D_i , for different gravity levels. a) Working fluid is Nitrogen at 77 K. b) Oxygen at 77 K. From Joy (1970) [38].

From these figures one can deduce that the performance degradation of a cryogenic heat pipe which has been optimized for reduced gravity operation would be so drastic at normal gravity that it might not be possible even to test such a design on earth in a horizontal position.

A close comparison between Figure 10-4a and b indicates that Nitrogen slightly excels Oxygen at reduced gravity but not under normal gravity conditions.

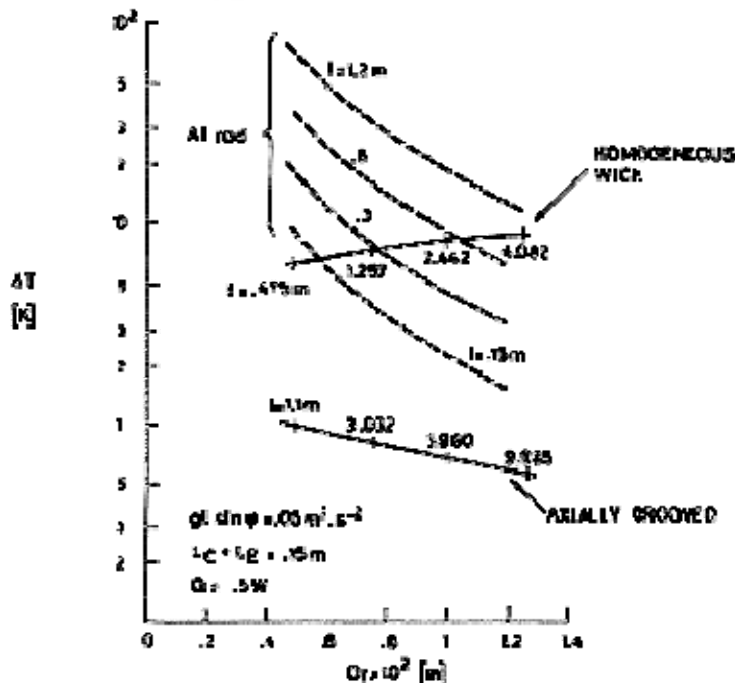
According to calculations, axially grooved heat pipes exhibit better performance than homogeneous wick heat pipes in terms of the heat transport factor, $(Q.l_{eff})$, in proportion of 2,3 to 1, which is nearly independent of the gravity level, g , as shown in Figure 10-5.



Note: non-si units are used in this figure

Figure 10-5: Maximum heat transport factor, ($Q \cdot L_{eff}$), for an axially grooved heat pipe and for a homogeneous wick heat pipe vs. inner diameter of the pipe, D_i , for different gravity levels. Working fluid is Oxygen at 77 K. From Joy (1970) [38].

Radial heat transfer at condenser and evaporator and heat pipe temperature drop are of concern in cryogenic heat pipes because of the very low fluid thermal conductivity which was mentioned in Table 10-1, Clause 10.2. These variables could place constraints on the heat pipe which are in opposition to those used to maximize ($Q \cdot L_{eff}$). This is analyzed in Figure 10-6.



Note: non-si units are used in this figure

Figure 10-6: Axial temperature drop, ΔT , for Oxygen heat pipes at 77 K vs. inner diameter of the pipe, D_i . Also shown are data for an axially grooved heat pipe and for aluminium rods of the same diameter. From Joy (1970) [38]. Calculation procedure is outlined in the text.

The axial temperature drop, ΔT , for a homogeneous wick, which is given in Figure 10-6, has been calculated as follows:

1. The heat entering the heat pipe evaporator is radially conducted across the entire thickness of the wick with evaporation taking place at the liquid-vapor interface. The effective thermal conductivity of wick and liquid is assumed to be equal to the thermal conductivity of the liquid alone. Estimations based on in series liquid and wick thermal conduction (see Table 5-1, Clause 5.2.3 and Clause 7.3) are about 20 % higher than the thermal conductivity of liquid oxygen.
2. The temperature drop through the vapor is assumed to be nil.
3. In the condenser, film condensation takes place at the liquid-vapor interface and heat is radially transferred through the liquid.
4. Given the heat load Q ($Q = 0.5$ W in Figure 10-6), evaporator and condenser lengths ($L_E = L_C = 0.075$ m), and the optimal diameter of the vapor space, D_v , for a given inner wall diameter of the pipe, D_i , the total temperature drop along the heat pipe, ΔT , can be estimated.

Also shown in Figure 10-6 are data for axially grooved heat pipes, the fins of which have a thickness, w' , equal to the channel width, w . Q , L_E and L_C are the same as above. Now the temperature drop has been calculated as follows:

1. The temperature drop in the evaporator has been calculated assuming one-dimensional heat conduction along the fin. The heat path becomes distorted near the fin tip toward

the liquid-vapor interface where evaporation occurs. Since $w' = w$ this distortion does not imply any change in the cross section area of the path.

2. In the condenser, one third of the condensing heat flux is assumed to be conducted directly by the fin, whereas the remaining heat flux is conducted through the liquid in the channel toward the fin surface and along the fin to its root in the pipe wall.

These heat pipe temperature drops can be compared to that of a high purity aluminium rod transferring the same Q , see Figure 10-6. Aluminium rods 0,30 m long and under are better than the optimal homogeneous wick cryogenic heat pipe. But axially grooved heat pipes are far superior in any case because of the more effective radial heat conduction through the fins.

10.5 Transient operating characteristics

Transient operation of a cryogenic heat pipe may occur in two different modes.

The first mode, which is common to heat pipes for any temperature range, appears when the heat transfer rate is far below the capillary operating limit. Under these conditions the heat pipe smoothly accommodates external changes in either heated or cooled end, the capillary structure is fully wetted, and temperature and pressure are almost uniform. The internal operation of the heat pipe is a purely static phenomenon controlled by the heat capacity and thermal conductivity of the container walls, wick and liquid working fluid. These transient operation will be called here "static transient".

A second transient operating mode which may appear in cryogenic heat pipes is the start-up from the thermodynamic supercritical state. Now the transient implies wick rewetting which takes place simultaneously with the heat conduction through the walls and through the wetted part of the wick. This transient operating mode (similar to that appearing in normal heat pipes after failure) will be identified here as "dynamical transient" because now the fluid dynamic evolution associated to fluid phase change in the wick should be taken into account.

10.5.1 Mathematical modelling of static transient

Smirnov, Barsookov & Mishchenko (1976) [89] developed a simple lumped mass model for the static transient operating regime. The model consists of several nodal points which, in the case of Figure 10-7, are distributed as follows: one nodal point corresponds to the heat source or sink (1); three to the pipe wall in the evaporator (2), adiabatic section (7) and condenser (9); three to the liquid-filled wick in the evaporator (4), adiabatic section (6) and condenser (8); one apparently corresponds to a fluid gap of the capillary structure in the evaporator (3); and the last one to the vapor region (5).

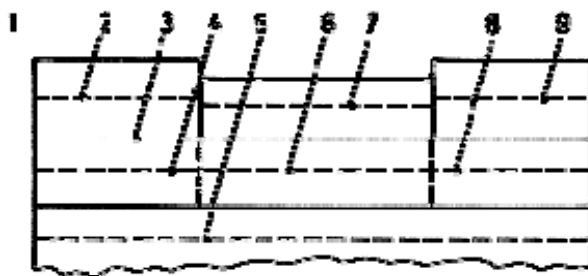


Figure 10-7: Nodal points in the static transient model of a heat pipe. From Smirnov, Barsookov & Mishchenko (1976) [89].

Axial heat transfer through pipe wall and through wick, interface thermal resistance and the influence of vapor flow between evaporator and condenser are neglected.

The energy balance for the i node may be written as follows:

$$C_i \frac{dT_i}{dt} + \sum_{j=1}^n H_{ij} (T_i - T_j) = Q_i \quad [10-3]$$

Note: non-si units are used in this figure

where $C_i = \rho c p_i \Delta V_i [\text{J.K}^{-1}]$ is the heat capacity associated to the mass lumped in node i , $H_{ij} = H_{ji} = h_{ij} S_{ij}$ [W.K^{-1}] is a heat transfer coefficient between nodes i and j . Finally, Q_i [W] is the external heat load in node i . Several of the constants C_i , H_{ij} and Q_i could be zero.

The linear system of differential equations [10-2] with the initial conditions $T_i = T_i(0)$ can be solved easily. In some cases it can be simplified reducing the number of nodes.

Although the crucial difficulty of this simple method is the correct estimate of the heat transfer coefficients H_{ij} , Smirnov et al. (1976) [89] report that the obtained results compare fairly well with the experimental ones for the starting up characteristics of the heat pipes that they tested (with water or Freon 113 as working fluids).

10.5.2 Mathematical modelling of fluid dynamic transient

A more elaborated numerical model has been developed by Chang & Colwell (1985) [13]. They take into account the rewetting of the capillary structure.

A cylindrical heat pipe with circumferential evaporator and condenser wicks, and a central slab wick is considered. The central slab (which runs through the total length of the pipe) is linked to the circumferential wicks in the evaporator and condenser sections, see Figure 10-8. This central slab is composed of layers of coarse mesh covered by layers of fine mesh screen. The circumferential wicks are formed with fine mesh screens at the liquid-vapor interface and coarse mesh screens near the inner wall.

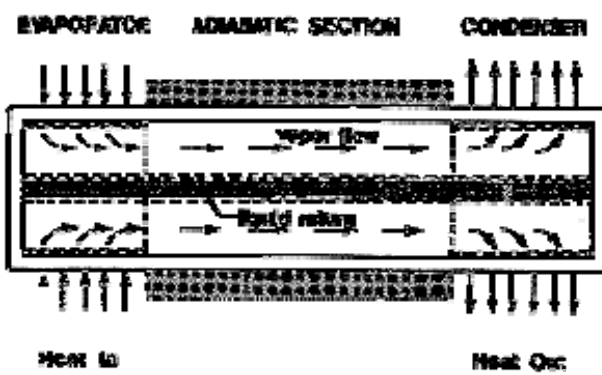


Figure 10-8: Schematic of the heat pipe considered by Chang & Colwell (1985) [13].

Different boundary conditions have been incorporated into the model, namely those simulating: constant surface temperature, uniform heat flux; a saddle for the evaporator surface and constant surface temperature, a cooling jacket; a radiator for the condenser surface.

Neither the thermal connection between the adiabatic section and the vapor space nor the boundary conditions at the wall inner surface of that section are discussed by the authors.

Temperature-dependent properties are considered. They are calculated using cubic spline interpolation, and reevaluated during the numerical computation when a temperature difference of more than a prescribed small value occurs between two consecutive steps.

The pipe wall and the liquid-saturated circumferential wicks are represented by means of finite-difference expressions of the non-steady conductive heat transfer equations in cylindrical coordinates. Nodal temperatures are calculated by an alternating-direction implicit (ADI) method. When the wick is partially dry only the liquid saturated nodes are taken into account.

The vapor space and the central slab wick are simulated by a lumped mass model at uniform temperature and thermally connected to the saturated wick at evaporator and condenser.

To predict dynamic transient operation a fine network of grid points are defined particularly when the modified rewetting model (see below) is used.

When the device is cooled from above the critical temperature, rewetting occurs. The different nodes of the condenser wick are assumed to be wet as soon as the node temperature drops below critical.

Rewetting of the central slab is analyzed by an independent one-dimensional flow model with phase change at the liquid front. To this aim a liquid volume of unit cross section, the length of which is at each moment equal to the distance between condenser section and liquid front, is considered.

In the simplified rewetting model the velocity of the liquid front is deduced from the momentum equation applied to the mentioned liquid volume. The pressure acting on the front is the difference between capillary pressure and liquid bulk pressure. The latter drops along the liquid volume from the condenser section according to Darcy's law ([ECSS-E-HB-31-01 Part 14, clause 7.4.2.4](#)). Once the liquid front reaches the evaporator section, the evaporator wick starts being wetted. This model is still compatible with a simplified single node representation of the central slab.

In the modified rewetting model evaporation at the liquid front is taken into account and then the front velocity is smaller. The evaporation mass rate depends on the heat transferred to the liquid from the wick. In most rewetting cases the capillary structure ahead of the liquid front may be at a higher temperature than the liquid moving through it. A more elaborate nodal representation of the central slab than that used up to the moment is required. No details are given.

The computation proceeds as follows: for each time step, the heat source and/or sink temperatures are evaluated first. These values and the vapor temperature are used to calculate the nodal temperatures using the ADI method. The new vapor temperature is then deduced from the new nodal temperatures and the location of the liquid front in the slab wick is evaluated if the slab is partially dry.

Computed values have been compared with those obtained experimentally by Colwell & Chang (1984) [17] on a Freon 11 heat pipe. Agreement is good for normal operation. For cool-down from the supercritical state the present model correctly predicts operating trends and the final steady state performance.

10.6 Reduced gravity testing of cryogenic heat pipes

Reliable performance prediction of cryogenic heat pipes under reduced gravity by use of measurements performed on Earth is very difficult as has been already indicated. That is why several flight experiments were planned to verify the performance of these heat pipes onboard several space platforms.

A preliminary review of experimental concepts for reduced gravity testing of cryogenic heat pipes has been reported by Kroliczek (1976) [45]. This author quotes four platforms: ATS-F, Landsat III, TIROS-N, LDEF. Nevertheless, a close attention to the follow-up literature seems to indicate that because of different circumstances only one of these attempts has been accomplished; no results have been reported up to now and reliable information on the behavior of cryogenic heat pipes under reduced gravity conditions is really scarce.

ATS-F. A fairly extensive heat pipe testing was attempted within this program. According to Berger & Kelly (1973) [4], all the heat pipes operated in the 278 K to 313 K temperature range. Working fluid was Ammonia. Later on cryogenic heat pipes were designed to replace several normal temperature heat pipes (Kroliczek (1976) [45]). Plans for the ATS-F were cancelled and further development of cryogenic heat pipe experiments designed for synchronous orbit conditions terminated.

Landsat III. A flight experiment designed to demonstrate cryogenic heat pipe technology has been defined, evaluated and thoroughly reported by Brennan & Kroliczek (1975) [12]. Two transporter (simple) heat pipes (the second as a design option, basically similar to the first one except for the attachment integral saddle) furnished by NASA-Goddard and a diode heat pipe, furnished by NASA-Ames, were considered. The heat pipes were mounted to the sensory ring of the spacecraft in the earth pointing direction and in thermal contact with a passive radiator. The working fluid was ethane and the temperature ranged from 150 K to 250 K in all cases. The configuration of the transporter was consistent with the geometrical restrictions imposed by the spacecraft, Figure 10-9.

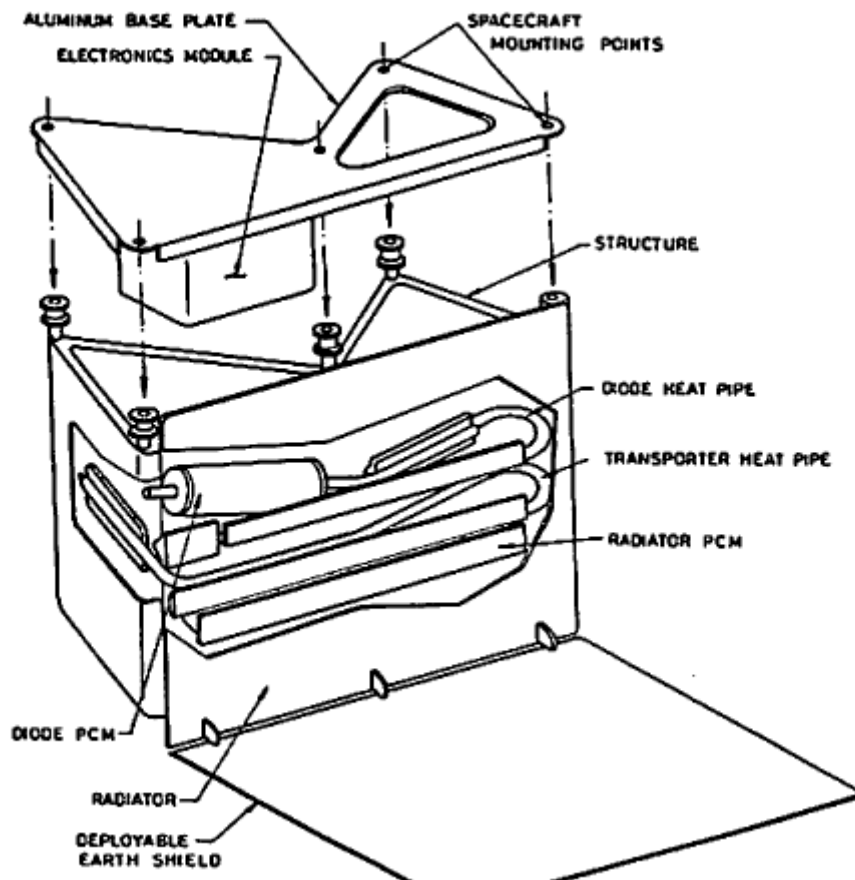


Figure 10-9: ERTS-C (Landsat III) cryogenic heat pipe experiment configuration.
From Brennan & Kroliczek (1975) [45].

The characteristics of the transporter heat pipe are given in Table 10-4, Clause 10.9. The diode heat pipe is not completely characterized by the authors, only the design specifications are reported and, thus, it has not been included in Table 10-4.

Later on the experiment was determined to be incompatible with operating procedures of the spacecraft.

TIROS-N was the next opportunity for obtaining extensive long-duration flight data on cryogenic heat pipes. A simple heat pipe and a diode were coupled with a passive radiant cooler (Ollendorf (1976) [65]) see also [ECSS-E-HB-31-01 Part 10, clause 8.4](#)). No results have been reported.

LDEF. McIntosh, Ollendorf & McCreight (in Clark (1981) [16]) describe an experiment, to be performed onboard this facility, which apparently is the same as that intended onboard TIROS-N. Later on Brennan & McIntosh (1985) [11] summarized the characteristics of this package but complete results from the flight test are not yet available.

Reduced gravity heat pipe data were obtained in the International Heat Pipe Experiment (Oct. 1974, Black Brant Sounding Rocket). Although results from several experiments within this Program have been reported (McIntosh, Ollendorf & Harwell (1975) [57]), the cryogenic heat pipe (axially grooved-methane) remained practically unnoticed.

10.7 Thermal diode cryogenic heat pipes

Thermal diode heat pipes operate as conventional heat pipes, but with high thermal conductance in one direction and very low thermal conductance in the reverse direction. They find application in spacecraft for the coupling of equipment to radiators, the surface of which becomes temporarily hotter than the equipment.

The normal fluid flow in a thermal diode is interfered somehow when the evaporator side becomes cooler than the condenser. In the excess liquid blockage techniques, the excess liquid accumulates, during reverse-mode (shut-off) operation, as a slug in the coldest portion of the heat pipe (unless it is displaced by surface tension or by gravity). Thus heat pipe operation ceases and heat is then transferred by conduction only.

An ammonia thermal diode was introduced in Clause 9.2. This particular model used the so-called "liquid trap technique" to accumulate the liquid in the evaporator when cold.

The thermal diode under consideration here uses the "blocking orifice technique", Figure 10-10.

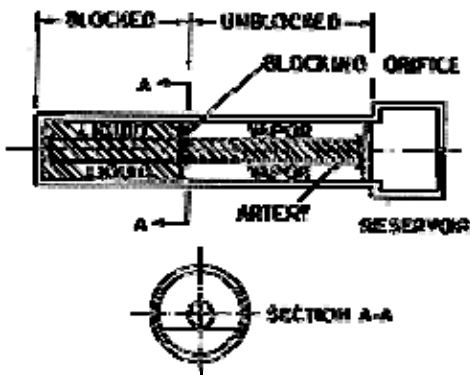


Figure 10-10: Schematic of a blocking orifice thermal diode heat pipe. From Kosson, Quadrini & Kirckpatrick (1974) [44]

Under the reverse mode of operation (cold evaporator end) the excess liquid is retained by an orifice plate which blocks, by capillary forces acting at the edge of the orifice, the vapor space of the cold end and a large part of the transport section. A reservoir would be provided at the other end to contain the excess liquid under normal-mode operation. To size the reservoir, changes in liquid density with temperature should be taken into account.

The blocking orifice technique to shut the pipe off during reverse mode operation is well suited to cryogenic diode applications for several reasons (Quadrini & McCreight (1977) [68]).

1. The liquid reservoir can be easily heated by the hot environment, to prevent liquid retention in the shut-off mode, and cooled by heat transfer to the radiator in the normal mode.
2. The evaporator is normally short compared with the condenser and total pipe length, minimizing blocking fluid requirements.
3. The liquid reservoir volume may be substantially reduced or even eliminated when blockage requirements can be met by the expansion of the normal fluid inventory during the hotter reverse mode operation.
4. Liquid reservoir volumes are less sensitive to reservoir temperatures when compared with reservoir volumes for other blockage techniques, as f.i., the non-condensable gas blockage technique.
5. Smaller liquid reservoir volumes and shutdown energies (see below) are required compared with other techniques.

In addition to the usual parameters for the normal mode of operation, namely: the maximum heat transfer rate vs. tilt and the temperature difference along the pipe associated to Q_{max} , important performance parameters of the heat pipe diode are the amount of energy absorbed and transmitted by the diode during transition from the forward to the reverse mode and during the reverse mode.

Shutdown energy is the energy required for transition from the forward to the reverse mode plus the reverse-mode heat loss during one hour. It does not account for the transmittal of energy due to partial heat pipe operation during the transition period.

10.7.2 Reversal requirements

To initiate the transition from the forward to the reverse mode of operation of liquid blockage diodes, two conditions must be simultaneously met. The liquid must be evaporated at the reservoir and condensed at the evaporator, thus:

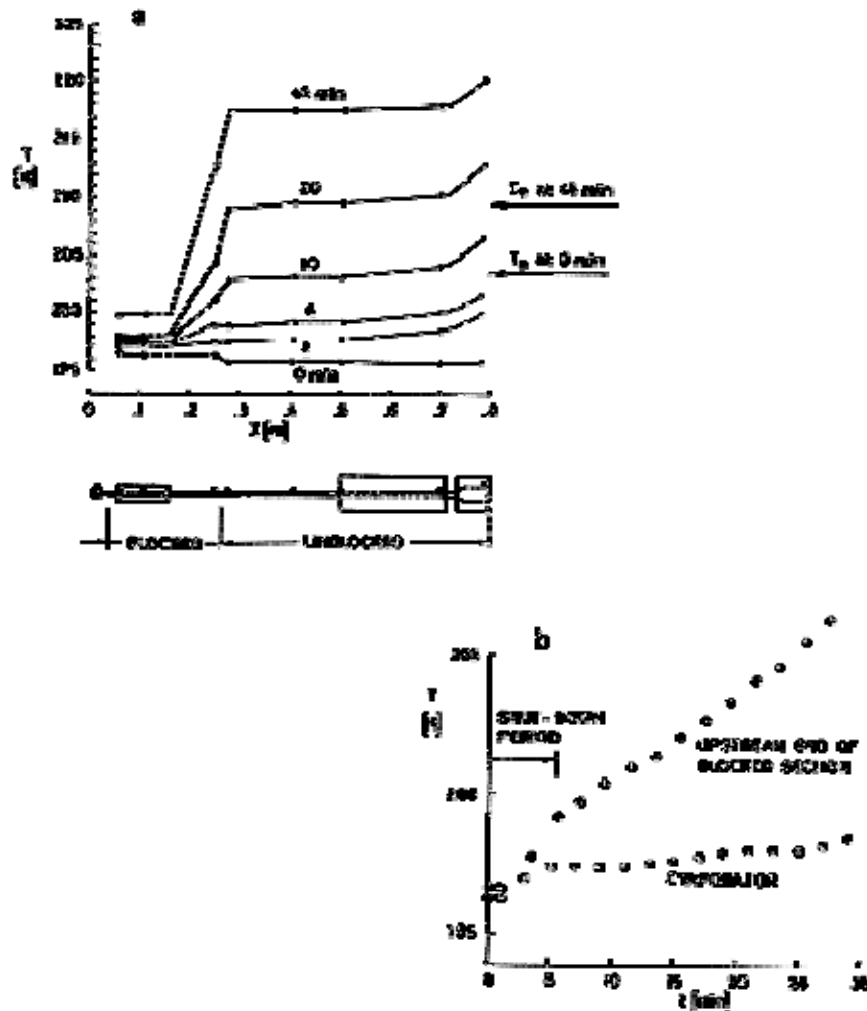
1. The internal surface temperature of the liquid reservoir must exceed the evaporation temperature.
2. The internal surface temperature of the evaporator must be lower than the evaporation temperature.

When only condition 1) is met, liquid will evaporate from the reservoir and condense in the condenser, where it will accumulate. The diode will operate in the normal mode, with below-nominal performances due to the excess liquid partially blocking the condenser. If condition 2) starts to be met after the beginning of condition 1), the liquid in the condenser will flow toward the evaporator by capillary action, and liquid blockage of the evaporator will begin. Additional blockage would occur as the remaining liquid evaporates from the reservoir.

When only condition 2) is met, vapor will condense in the reservoir filling it. After the reservoir is full the diode will operate in the reverse mode as a normal heat pipe with no shut-off. If condition 1) is

then met, liquid will begin to evaporate from the reservoir and condense in the evaporator region of the diode. Shut-off occurs at a rate which depends on the rate of evaporation from the reservoir.

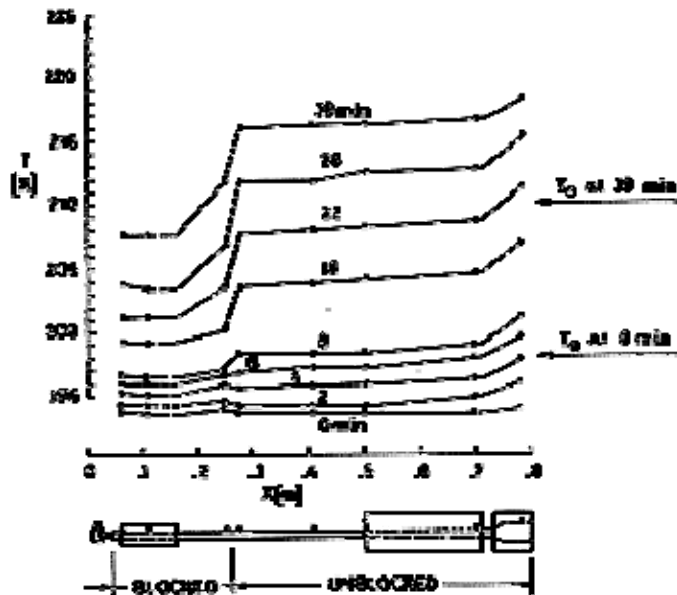
An ethane thermal diode cryogenic heat pipe has been developed (Quadrini & McCreight (1977) [66]); its main characteristics and performance in the normal mode are summarized in Table 10-4, Clause 10.9. Characteristic features of the diode (transition to and reverse mode) are given in Figure 10-11 and Figure 10-12.



Note: non-si units are used in this figure

Figure 10-11: a) Axial temperature profiles during reverse mode tests of a cryogenic heat pipe diode. No tilt. Tests performed in an insulated LN₂ cooled enclosure. At time 0 power (3 W) is removed from the evaporator, and the reservoir heater is on. T_0 is the ambient temperature within the enclosure.

b) Shut-down temperature response of evaporator and upstream end of blocked transport section. From Quadrini & McCreight (1977) [66].



Note: non-si units are used in this figure

Figure 10-12: Axial temperature profiles during reverse mode tests. Tests performed as in Figure 10-11a except 1 W heat load on the evaporator continuously fed during the run. T_0 is the ambient temperature within the enclosure. From Quadrini & McCreight (1977) [66].

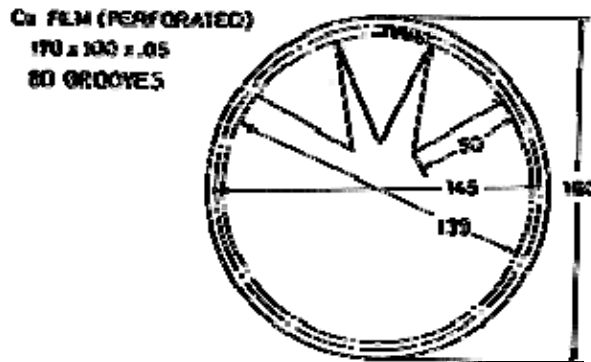
10.8 Superfluid heat pipes

When superfluid helium (He II below 2,17 K, [ECSS-E-HB-31-01 Part 14, clause 7.1](#)) is used as the working fluid, a natural heat pipe results in the sense that no wick is required to conduct the liquid back to the evaporator. Rather, the superfluid component returns by the "thermo-mechanical effect" ([ECSS-E-HB-31-01 Part 14, clause 7.1.2](#)), generated by the temperature differences between evaporator and condenser, along the superfluid helium film (Clause 7.1.5). Since the required amount of working fluid is small, the superfluid heat pipe is free from the high vapor pressure under storage which is characteristic of other cryogenic heat pipes (Table 10-1, Clause 10.2).

Three superfluid heat pipes have been fabricated and tested by Murakami and coworkers (Murakami & Kaido (1980) [61], Murakami (1982) [60]). Their characteristics are:

Heat Pipe 1. Closed copper tube 10^{-2} m inner diameter, 10^{-3} m wall thickness, 0,16 m long.

Heat Pipe 2. Closed copper tube $14,5 \times 10^{-3}$ m inner diameter, 16×10^{-3} m outer diameter, 0,17 m long with 80 axial grooves and a very thin perforated copper film of 0,17 m by 0,10 m, 5×10^{-5} m thick, wetted perimeter $\Pi = 0,286$ m, Figure 10-13.



Note: non-si units are used in this figure

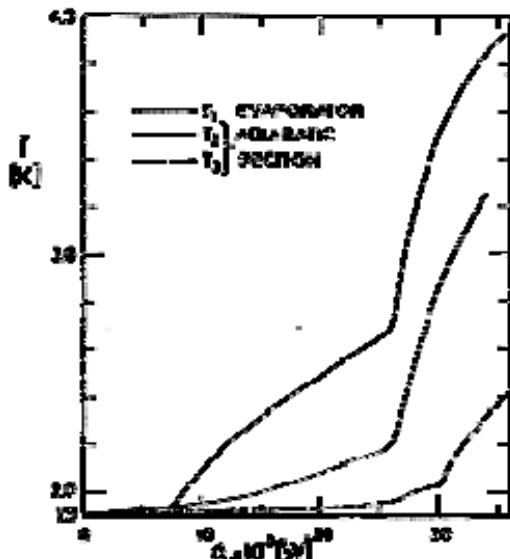
Figure 10-13: Cross section of Heat Pipe 2. From Murakami & Kaido (1980) [61]. All the dimensions are in mm.

Heat Pipe 3. Closed copper tube $14,5 \times 10^{-3}$ m inner diameter, 16×10^{-3} m outer diameter, 0,177 m long with 80 axial grooves and a very thin perforated copper film of 0,197 m by 0,165 m, wetted perimeter, $\Pi = 0,48$ m. Evaporator length 25×10^{-3} m, condenser length 27×10^{-3} m.

All three pipes were loaded with helium gas to about 6×10^5 Pa at room temperature. This amount of helium is sufficient to form a superfluid helium layer over the wetted surface when $T < T_\lambda$.

The aim of the grooves and copper film is to increase the wetted perimeter to enhance film flow and Kapitza conductance ([ECSS-E-HB-31-01 Part 14, clause 7.2](#)). The latter objective has not been clearly achieved.

For testing, the pipes were installed vertically with the evaporator upward within a vacuum adiabatic jacket except for the condenser which was exposed to the outer He II as a constant temperature heat sink. The tests were performed continuously increasing the heater power from 0 W to 60×10^{-3} W at a slow rate, spending about one hour in order to achieve a quasi-steady heating condition. Curves of temperature, T , vs. heat transfer rate, Q , for Heat Pipe 3 are given in Figure 10-14.



Note: non-si units are used in this figure

Figure 10-14: Temperature, T , vs. heat transfer rate, Q , in Heat Pipe 3. T_1 is the evaporator temperature, T_2 and T_3 are in the adiabatic clause $88 \times 10^{-3} \text{ m}$ and $78 \times 10^{-3} \text{ m}$ from the evaporator end. The sink temperature is $T_s = 1,9 \text{ K}$. From Murakami (1982) [60].

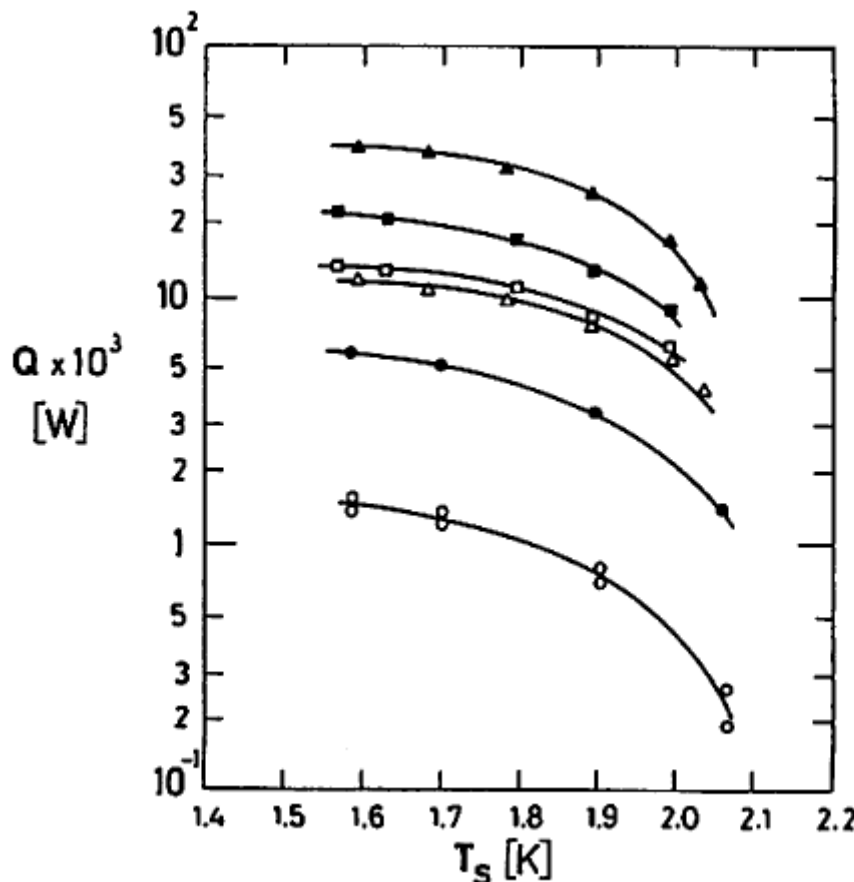
Three modes of heat pipe action according to the heat transfer rate can be distinguished in the figure, namely:

1. Superfluid-subcritical mode. The temperature in the evaporator, T_1 , rises proportionally to the heat transfer rate for small values of Q .
2. Superfluid-supercritical mode. At about $Q = 8 \times 10^{-3} \text{ W}$ a jump in the temperature is recorded, which is akin to others which appear in tubes under similar conditions (see, f.i., [ECSS-E-HB-31-01 Part 14, Fig. 7-8 in clause 7.1.3](#)). The jump apparently results from transition to supercritical conditions. This transition occurs, for different heat transfer rates, in different locations along the tube, presumably because the superfluid velocity increases along the tube since the thickness of the stationary film decreases with height along the duct due to gravity action ([ECSS-E-HB-31-01 Part 14, clause 7.1.6](#)). Then the critical superfluid velocity ([ECSS-E-HB-31-01 Part 14, clause 7.1.3](#)) is reached first at the entrance of the evaporator.
3. Conductive heat transfer mode. At $Q = 26 \times 10^{-3} \text{ W}$ ($Q = Q_\lambda$) the temperature in the evaporator experiments a second jump. This is related to the λ -transition (from He II to He I, [ECSS-E-HB-31-01 Part 14, Fig. 7-1, Clause 7.1](#)) of the liquid in the film. Beyond Q_λ only heat conduction through the pipe wall (including Kapitza conductance effects) participates in the heat transfer.

The temperature variation when Q decreases are basically the same, but weak hysteresis (not shown in Figure 10-14) are observed at $Q = Q_c$ and Q_λ , see Fig. 3 in Murakami & Kaido (1980) [61].

The heat transfer coefficient of the heat pipe, $h [\text{W} \cdot \text{m}^{-2} \cdot \text{K}^{-1}]$, is deduced from $Q/(T_1 - T_s)$ and the cross-sectional area of the vapor core. It is maximum under subcritical conditions and diminishes to a value given by pure thermal conduction through the pipe wall (including Kapitza conductance effects) beyond Q_λ .

The three heat pipes are compared in Figure 10-15 in terms of the critical heat transfer rates, Q_c and Q_λ vs. sink temperature, T_s . The largest heat transfer rate corresponds to Q_λ . It is also shown in the figure that larger wetted perimeters, Π , result in increased Q_λ (Π was the largest in Heat Pipe 3 and the smallest in Heat Pipe 1, clause 10.8). This can be attributed to increased cross-sectional area of the film which has a given thickness at saturation and, thus, increased mass flow rate.



Note: non-si units are used in this figure

Figure 10-15: Critical heat transfer rate, Q_c , and λ-transition heat transfer rate, Q_λ , for the three heat pipes as a function of sink temperature, T_s . From Murakami (1982) [60]. Key is given below.

Explanation

Heat Pipe	Q_c	Q_λ
1	○	●
2	□	■
3	△	▲

10.9 Existing systems

Data regarding cryogenic heat pipes, which have been tested, are collected in Table 10-4, at the end of this clause.

To summarize in a unified fashion the information from different sources on the performances of these heat pipes is not an easy task. This is so because the data given are really varied even for different heat pipes within the same source.

As a solution, a Table enclosing data which are given in common by all sources is presented. The compiler is aware that many useful data could be lost. The user should be then addressed to the references which are also enclosed in the Table.

The nominal Integral Heat Transfer Factor ($Q.l_{eff}$) of the cryogenic heat pipes introduced in Table 10-4 are summarized in Figure 10-16. The same key symbols have been used in Table 10-4 and Figure 10-16 to identify a given heat pipe.

Table 10-4: Characteristics of Tested Cryogenic Heat Pipes

Key Type	l [m]	l_c [m]	l_E [m]	$D_{ox} \times 10^3$ [m]	$D_{ix} \times 10^3$ [m]	Materials	Operating Conditions	Manufacturer Reference			
OX 32,00	1	0,1 to 0,8	0,3 to 0,2	3,2	2,4	Table 10-5	Table 10-6	SABC, Mathieu (1981,1982) [55], [54]			
01											
02											
OX 64,00	1	0,1 to 0,8	0,3 to 0,2	6,4	5,4						
01											
02											
N 32,02	1	0,1 to 0,8	0,3 to 0,2	3,2	2,4						
03											
04											
N 64,01	1	0,1 to 0,8	0,3 to 0,2	6,4	5,4						
02											
03											
ME 32,03	1	0,1 to 0,8	0,3 to 0,2	3,2	2,4						
04											
05											
ME 64,02	1	0,1 to 0,8	0,3 to 0,2	6,4	5,4						
03											
04											
E 32,02	1	0,1 to 0,8	0,3 to 0,2	3,2	2,4						

Key Type	l [m]	l_c [m]	l_E [m]	$D_o \times 10^3$ [m]	$D_i \times 10^3$ [m]	Materials	Operating Conditions	Manufacturer Reference
03								
04	0,35	0,2	0,2					
E 64,01	1	0,1 to 0,8	0,3 to 0,2	6,4	5,4			
02								
03	0,35	0,2	0,2					
1	0,5	0,1	0,1	8	6			IKE, Molt (1976) [59]
2								
3					7			
4	0,45	0,15	0,15	19,5	13,1			
5				15,5	10,9			
6					8,7			
7					8,6			
1	0,22	0,06	0,06	8	6			Kiev Politech., Semena & Levterov (1978) [84]
2	0,5	0,12	0,08	10	8			
3	0,1	0,04	0,05	38	33			
H Homogeneous	0,98	0,15	0,15	12,7	11,3			TRW-NASA Groll, Pittman & Eninger (1976) [30]
G Graded								
3 ft	0,91	0,29	0,30	15,2	11,9			Grumman, Dominguez & Kosson (1973) [20]
8 ft	2,4	1,4	0,13	15,9	12,7			
Diode	0,758	0,213 ^f	0,102	6,35 ^f	4,93			Grumman, Quadrini & McCreight (1977) [68]
GSFC	1,27	0,483	0,127	14,2	11			NASA-GSFC Brennan & Kroliczek (1975) [12]

^f Excess liquid reservoir, $l_R = 0,06$ m. $OD_R = 15,9 \times 10^{-3}$ m.

Table 10-5: Characteristics of Tested Cryogenic Heat Pipes, Materials

Key Type	Wick	Wall Material	Working Fluid	Fill Charge $\rho \times 10^{-3} [\text{kg.m}^{-3}]$
OX 32,00	Circumferential wire mesh	SS	O_2	0,210 ^b 0,450 ^c at 73 K
01				
02				
OX 64,00				0,210 ^b 0,250 ^c at 73 K
01				
02				
N 32,02			N_2	0,180 ^b 0,275 ^c at 100 K
03				
04				
N 64,01				0,180 ^b 0,165 ^c at 110 K
02			CH_4	
03				
ME 32,03				0,125 ^b 0,157 ^c at 123 K
04				
05				
ME 64,02				0,125 ^b 0,085 ^c at 123 K
03			C_2H_6	
04				
E 32,02				0,400 ^b 0,193 ^c at 223 K
03			CH_4	
04				
E 64,01				0,400 ^b 0,107 ^c at 223 K
02				
03				
1	1 layer screen 160 mesh.	Al	CH_4	0,5x10 ⁻³ kg 0,35 g
2	IKE "eight" artery			0,9x10 ⁻³ kg 0,64 g

Key Type	Wick	Wall Material	Working Fluid	Fill Charge $\rho \times 10^{-3}$ [kg.m $^{-3}$]
3	Modular heat pipe.	SS		$1,4 \times 10^{-3}$ kg 0,072 g
4	36 rectangular grooves.	Al	CF ₄	$19,7 \times 10^{-3}$ kg 0,325 g
5	27 trapez. Grooves. Width increases with radial distance.		CH ₄	$14,8 \times 10^{-3}$ kg 0,352 g
6	20 trapez. Grooves. Width decreases with radial distance.	Cu grooves involved with SS tube		$17,2 \times 10^{-3}$ kg 0,642 g
7	Grooves as above. 1 layer screen 160 mesh.			
1	Metal-fiber welded. $\delta = 0,45 \times 10^{-3}$ m, $\Phi = 0,82$.	Cu same as wick	N ₂	$1,3 \times 10^{-3}$ kg 0,237 k
2	Metal-fiber welded. $\delta = 10^{-3}$ m, $\Phi = 0,75$.	1 Kh 18 N 10 T e. Same as wick.		
3	Metal-fiber welded. $\delta = 1,35 \times 10^{-3}$ m, $\Phi = 0,70$.			
H Homogeneous	4000 circumferential grooves/m. Homogeneous horizontal slab. $\Phi = 0,863$ $7,37 \times 10^{-3}$ m x $11,4 \times 10^{-3}$ m.	PH 15-7 Mo SS	CH ₄	$17,56 \times 10^{-3}$ kg 95% fill at 110 K
	As above, vertical slab.		C ₂ H ₆	$22,80 \times 10^{-3}$ kg 95% fill at 180 K
G Graded	4000 circumferential grooves/m. Graded horizontal slab. Φ and dimensions as in Figure 10-3		CH ₄	$17,56 \times 10^{-3}$ kg 95% fill at 110 K
	As above, vertical slab.		C ₂ H ₆	$22,80 \times 10^{-3}$ kg 95% fill at 180 K
3 ft	4000 circumferential grooves/m. Tunnel arteries 250 mesh SS, $4,3 \times 10^{-3}$ m OD, $3,2 \times 10^{-3}$ m ID. Retaining webs.	Al alloy 6061-T6	Freon 14	0,445 at 133 K
8 ft				0,517 at 133 K

Key Type	Wick	Wall Material	Working Fluid	Fill Charge $\rho \times 10^{-3}$ [kg.m $^{-3}$]
Diode	6300 circumferential grooves/m. Spiral arteries 250 mesh. Webs	304-1/8 HD SS Reservoir Al alloy 6061	C ₂ H ₆	4,48x10 $^{-3}$ kg 100% fill at 200 K 0,310 g
GSFC	27 axial grooves. $w=0,6 \times 10^{-3}$ m, $w = 0,43 \times 10^{-3}$ m, $\delta=1,02 \times 10^{-3}$ m. Integral saddle.	Al alloy 6063 6061 optional		13x10 $^{-3}$ kg at 180 K 0,108 g

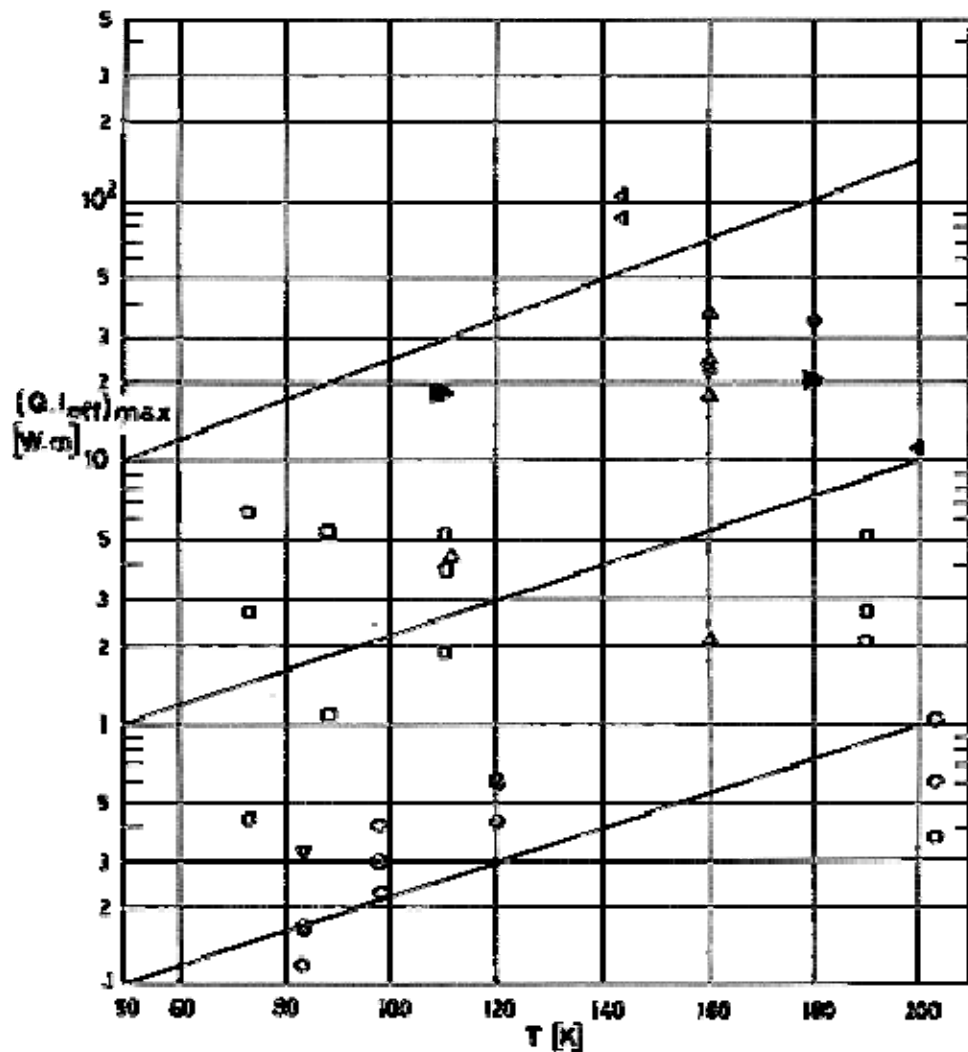
^b Based on burst limit at 313 K.^c Required at optimum working temperature. Data given at filling temperature.^e Stainless steel. Russian designation. C-0,08/0,12, Si-<0,8, Mn-<1., P.<0,015, S-<0,015, Cr-17./19., Ni-9./11., Ti-5xC/0,70.^g Estimated from l and D_i .^k Estimated from l , D_i , δ and Φ .**Table 10-6: Characteristics of Tested Cryogenic Heat Pipes, Operating Conditions**

Key Type	Working Fluid	Operat. T [K]	$(Q_{leff})_{max}$ [W.m]	ΔT [K]	Max ^a $l \sin \phi \times 10^3$ [m]	Comments
OX 32,00	O ₂	98 (opt.)	0,3		8,22	Reinforced to avoid bursting.
01			0,236		12,3	Degraded performance after sealing.
02			0,41		5	With expansion reservoir (upside when tilted)
OX 64,00		88 (opt.)	5,45		7,72	Higher than predicted performance.
01			5,5		6,1	
02			1,07		11	With expansion reservoir (upside when tilted).
N 32,02	N ₂	83 (opt.)	0,169		6,4	Performance degraded after sealing.
03			0,163		4,57	Same performance before and after sealing.
04			0,120		4,65	Length effect as predicted. Vibration tested. ^d
N 64,01		73 (opt.)	6,5		8,1	Exceptionally high performance unexplained.

Key Type	Working Fluid	Operat. T [K]	$(Q_{left})_{max}$ [W.m]	ΔT [K]	Max ^a $l \sin \varphi \times 10^3$ [m]	Comments	
02			2,65		8,32	Slightly exceeded the predictions.	
03			0,44		12,77	Grater than expected length effect. Vibration tested. ^d	
ME 32,03	CH ₄	120 (opt.)	0,61		17,2	As predicted.	
04			0,424		23,7	Q_{max} below predictions. φ_{max} larger than predicted.	
05			0,604		23,9	With expansion reservoir elevated above pipe axis.	
ME 64,02		110 (opt.)	3,86		26,7	As predicted.	
03			5,44		18,45	Q_{max} above predictions.	
04			1,81		21	With expansion reservoir.	
E 32,02	C ₂ H ₆	203 (opt.)	0,608		16,6	Low power vs. tilt.	
03			1,03		14,2	Q_{max} above predictions.	
04			0,362		18	Length effect as predicted. Vibration tested. ^d	
E 64,01		190 (opt.)	2,7		27,7	Roughly as predicted.	
02			5,26		17,2	Large experimental scatter.	
03			2,04		28,6	Length effect as predicted. Vibration tested. ^d	
1	CH ₄	110	0 ^h	0	< 0	Not operable in horizontal position unless overfilled.	
2		160	2,08 ^h	5	6,2 ⁱ	Aims at reducing the pressure drop.	
3		111	4,20 ^h	4		Further reduced pressure drop.	
4	CF ₄	CH ₄	25,8 ^h	20	6,2 ⁱ		
5			18 ^h	25	5,6 ⁱ	Q_{max} below prediction at high temperature.	
6			26,1 ^h	30	5,5 ⁱ	Large Q_{max} attributed to trapezoidal grooves.	
7			37,5 ⁱ	35	4,8 ⁱ	Screen controls capillary pressure. At large φ behaves as 6.	
1	N ₂	83	0,32 ^h	2,4		Q_{max} as predicted.	

Key Type	Working Fluid	Operat. T [K]	$(Q_{eff})_{max}$ [W.m]	ΔT [K]	Max ^a $l \sin \varphi \times 10^3$ [m]	Comments
2			2 ^h			Q_{max} slightly above predictions.
3			1,98 ^h			Q_{max} 50% below predictions. Incomplete saturation.
H Homogeneous	CH ₄		24,9 ^h 105% 150 K		25 105% 150 K	Large Q_{max} than in G.
	C ₂ H ₆					
	CH ₄		17,8 ^h 100% 150 K		28,8 100% 150 K	
	C ₂ H ₆					
G Graded	CH ₄	110 (opt.)	18,3 ^h 0,0025 m tilt		47,5 150 K	Q_{max} below predictions. Grooves dried out.
	C ₂ H ₆	180 (opt.)	20,3 ^h		41,5 236 K	Wick deformed during insertion. Wick porosity optimization should be reconsidered.
	CH ₄	110 (opt.)	18,3 ^h 0,0025 m tilt		47,5 150 K	
	C ₂ H ₆	180 (opt.)	20,3 ^h			
3 ft	Freon 14	144	106 ^l	8,3 ^m	44,4	Very high capacity.
8 ft			87 ⁿ	1,7 ^m	15,2 ⁱ	Low ΔT .
Diode	C ₂ H ₆	200	12,5 ^o		110 ⁱ	For reverse performance see Figure 10-11 and Figure 10-12. TIROS-N HP experiment, see p. M 4-29 ??.
GSFC		180 (opt.)	35,7 ^p		10,5 180 K	In plane bent. ERTS-C (Landsat III) experiment. See clause 10.6.

^a Tilt limit. Evaporator up.^d All heat pipes were leakage and burst tested. Vibration tests only performed when indicated (0,35 m long heat pipes).^h From $l_{eff} = l - (l_c + l_E)/2$ and given Q_{max} .ⁱ Extrapolated.^j Q_{max} at zero tilt exceeds the experimental capability. Quoted value corresponds to 10^{-3} m adverse tilt.^l $l_{eff} = 0,603$.^m For $Q = 60$ W, $3,2 \times 10^{-3}$ m tilt. Not very sensitive to Q .ⁿ $l_{eff} = 1,70$ m.^o $l_{eff} = 0,501$ m.^p $l_{eff} = 0,965$ m.^q From heat transfer rate ($Q = 37$ W) and heat pipe conductance ($C = 4,65$ W/K).



Note: non-si units are used in this figure

Figure 10-16: Integral heat transport factor, $(Q.l_{eff})_{max}$, vs. operating temperature, T , of the cryogenic heat pipes tabulated in Table 10-4.

Trends given in Figure 10-16 seem to indicate that three power levels exist. The upper level corresponds to grooved heat pipes developed in USA in the early seventies. Since these cryogenic heat pipes are very oversized with respect to the low power levels usually required for applications, smaller diameter heat pipes (typically $D_o = 3,2 \times 10^{-3}$ m) began to be developed in Europe. Later on, in order to increase the power level to about 2 W.m, larger diameter heat pipes ($D_o = 6,4 \times 10^{-3}$ m) were developed.

Bibliography

- [1] AIAA Paper 86-1254. AIAA/ASME 4th Joint Thermophysics and Heat Transfer Conference, Boston, Mass., June 2-4, 1986.
- [2] ASHRAE, "Ashrae Handbook. 1985 Fundamentals", Ashrae Inc., 1791 Tullie Circle, N.E. Atlanta, GA 30329, 1985.
- [3] Basiulis, A., Filler, M., "Operating Characteristics and Long Capabilities of Organic Fluid Heat Pipes", in "Progress in Astronautics and Aero-nautics", Vol. 29, J.W. Lucas, Ed., MIT Press, Cambridge, Mass., 1972, pp. 431-444.
- [4] Berger, M.E., Kelly, W.H., "Application of Heat Pipes to the ATS F Spacecraft", ASME Paper 73-ENAs-46, SAE-ASME-AIAA-AIChE Intersociety Conference on Environmental Systems, San Diego, Calif., July 16-19, 1973.
- [5] Bhatti, R.S., "Heat Pipe", 1986.
- [6] Bhatti, R.S., Van Oost, S., "Qualification Programme on Stainless Steel - 195 - Heat Pipe for Space Application", 1988.
- [7] Bhatti, R.S., Van Oost, S., Savage, C.J., "Feasibility Demonstration Model of a Capillary Pumping Loop", 1988.
- [8] Bhatti, R.S., Van Oost, S., Super, W., Wulz, H., "Two-Phase Capillary-Pumped Loop: A Potential Heat Transport System", 1989.
- [9] Bienert, W.B., Brennan, P.J., Kirckpatrick, J.P., "Feedback Controlled Variable Conductance Heat Pipes", AIAA Paper 71-421, April 1971.
- [10] Bird, R.B., Stewart, W.F., Lighfoot, F.M., "Transport Phenomena", John Wiley & Sons, Inc., New York, 1960.
- [11] Brennan, P., McIntosh, R., "Flight Data Evaluation for a Low Temperature Heat Pipe Experiment Package", AIAA Paper 85-1010. AIAA 20th Thermophysics Conference, Williamsburg, Virginia, June 19-21, 1985.
- [12] Brennan, P.J., Krolczek, E.J., "ERTS-C (Landsat III) Cryogenic Heat Pipe Experiment Definition",
- [13] Chang, W.S., Colwell, G.T., "Mathematical Modeling of the Transient Operating Characteristics of a Low-Temperature Heat Pipe", Numerical Heat Transfer, Vol. 8, 1985, pp. 169-186.
- [14] Chemical Engineering Symposium Series, Vol. 66, No. 102, 1970.
- [15] Chi, S.W., Cygnarowicz, T.A., "Theoretical Analyses of Cryogenic Heat Pipes", ASME Paper 70-HT/SpT-6, in "Space Systems and Thermal Technology for the 70's", Part II, ASME, 1970.
- [16] Clark, L.G., "LDEF First Mission Experiments", Preliminary Copy, NASA Langley Research Center, Sept. 1981.

- [17] Colwell, G.T., Chang, W.S., "Measurements of the Transient Behavior of a Capillary Structure under Heavy Thermal Loading", *Int. J. Heat Mass Transfer*, Vol. 27, No. 4, April 1984, pp. 541-551.
- [18] Cotter, T.P., "Theory of Heat Pipes", Report LA-3246-MS, Los Alamos Scientific Laboratory, March 1965. Also published in "Heat Pipes", AIAA Selected Reprint Series, Vol. XVI, C.L. Tien, Ed., AIAA, New York, Sept. 1973, pp. 11-41.
- [19] Das, T.R., Eubank, P.T., "Thermodynamic Properties of Propane: Vapor-Liquid Coexistence Curve", in "Advances in Cryogenic Engineering" Vol. 18, K.D. Timmerhaus, Ed., Plenum Press, New York, 1973, pp. 208-219.
- [20] Dominguez, P., Kosson, R., "Development of a High Capacity Cryogenic Heat Pipe", AIAA Paper 73-729. AIAA 8th Thermophysics Conference, Palm Springs, Calif., July 16-18, 1973.
- [21] Dunn, P., Reay, D.A., "Heat Pipes", 1st ed., Pergamon Press, Oxford, 1976.
- [22] Dzakowic, G.S., Tang, Y.S., Arcella, F.G., "Experimental Study of Vapor Velocity Limit in a Sodium Heat Pipe", ASME Paper 69-HT-21, Aug. 1969.
- [23] Edelstein, F., Hembach, R.J., "Design, Fabrication, and Testing of a Variable Conductance Heat Pipe for Equipment Thermal Control", in "Progress in Astronautics and Aero-nautics", Vol. 29, J.W. Lucas, Ed., MIT Press, Cambridge, Mass., 1972, pp. 487-504.
- [24] Ferrel, J.K., Alexander, E.G., Piver, W.T., "Vaporization Heat Transfer in Heat Pipe Wick Materials", in "Progress in Astronautics and Aero- nautics", Vol. 31, C.L. Tien, Ed., MIT Press, Cambridge, Mass., 1973, pp. 3-18. Also published in "Heat Pipes", AIAA Selected Reprint Series, Vol. XVI, C.L. Tien, Ed., AIAA, New York, Sept. 1973, pp. 117-124.
- [25] Ferrel, J.K., Alleavitch, J., "Vaporization Heat Transfer in Capillary Wick Structures",
- [26] Ferrel, J.K., Johnson, H.R., "The Mechanism of Heat Transfer in the Evaporator Zone of a Heat Pipe", ASME Paper 70-HT/SpT-12, in "Space Systems and Thermal Technology for the 70's", Part II, ASME, 1970.
- [27] Frank, S., Smith, J.T., Taylor, K.M., "Heat Pipe Design Manual", Report MND-3288, Martin Marietta Corp., Baltimore, Maryland, Feb. 1967.
- [28] Grant, I.D.R., "Boiling and Condensation in Heat Pipes", in "Analysis, Design and Manufacture of Heat Pipes", Course Papers, Birnie- hill Institute, National Engineering Laboratory, East Kilbride, Glasgow, June 1973.
- [29] Groll, M., Munzel, W.D., "Design and Development of a Heat Pipe Diode, Phase I: Design", prepared under ESA Contract No. 2993/76/NL by Institut fur Kernenergetik (IKE), University of Stuttgart, Final Report, July 1977.
- [30] Groll, M., Pittman, R.B., Eninger, J.E., "Parametric Performance of Circumferentially Grooved Heat Pipes with Homogeneous and Graded-Porosity Slab Wicks at Cryogenic Temperatures", in "2nd International Heat Pipe Conference 1976", Bologna, Italy, 31st March-2nd April, ESA SP-112 (preprint), Vol. 1, ESTEC, Noordwijk, The Netherlands, pp. 63-76.
- [31] Groll, M., Zimmermann, P., "Heat Pipe for Temperature Control of a Meteorological Satellite", ESRO CR-59, Sept. 1972.
- [32] Grover, G.M., Cotter, T.P., Erickson, G.F., "Structures of Very High Thermal Conductance", *Journal of Applied Physics*, Vol. 35, No. 6, June 1964, pp. 1990-1991. Also published in "Heat Pipes", AIAA Selected Reprint Series, Vol. XVI, C.L. Tien, Ed., AIAA, New York, Sept. 1973, pp. 9-10.

- [33] Haskin, W.L., "Cryogenic Heat Pipe", Air Force Flight Dynamics Laboratory, Technical Report AFFDL-TR-66-228, June 1967.
- [34] HAWKER SIDDELEY, "Private Communication by P.P. Hanks", Hawker Siddeley Dynamics Limited. Gunnels Wood Road, Stevenage, Hertfordshire SG1 2AS, England, Aug. 1974.
- [35] Hinderman, J.D., Waters, E.D., Kaser, R.V., "Design and Performance of Noncondensable Gas Controlled Heat Pipes", in "Progress in Astronautics and Aero-nautics", Vol. 29, J.W. Lucas, Ed., MIT Press, Cambridge, Mass., 1972, pp. 445-461.
- [36] JERMYN, "Heat Pipes (Caloducs)", in "Catalogue Jermyn", pp. 64-67. Jermyn, 2 rue de Londres, 75009 Paris, France, Jan. 1974.
- [37] Johnson, V.J., "Properties of Materials at Low Temperatures (Phase 1)", 1st ed., Pergamon Press, New York, 1961, 10,001.
- [38] Joy, P., "Optimum Cryogenic Heat Pipe Design", ASME Paper 70-HT/SpT-7, in "Space Systems and Thermal Technology for the 70's", Part II, ASME, 1970.
- [39] Katzoff, S., "Heat Pipes and Vapor Chambers for Thermal Control of Spacecraft", in "Progress in Astronautics and Aeronautics", Vol. 20, G.B. Heller, Ed., Academic Press, New York, 1967, pp. 761-818.
- [40] Kemme, J.E., "Heat Pipe Design Considerations", Report LA-4221-MS, Los Alamos Scientific Laboratory, Aug. 1969. Also published in "Heat Pipes", AIAA Selected Reprint Series, Vol. XVI, C.L. Tien, Ed., AIAA, New York, Sept. 1973, pp. 52-57.
- [41] Kemme, J.E., "Ultimate Heat Pipe Performance", IEEE Thermionic Conversion Specialist Conference, 1968, pp. 266-271.
- [42] Kirckpatrick, J.P., Marcus, B.D., "A Variable Conductance Heat Pipe Flight Experiment", in "Progress in Astronautics and Aeronautics", Vol. 29, J.W. Lucas, Ed., MIT Press, Cambridge, Mass., 1972, pp. 505-527.
- [43] Kirckpatrick, J.P., Marcus, B.D., "A Variable Conductance Heat Pipe/Radiator for the Lunar Surface Magnetometer", in "Progress in Astronautics and Aero-nautics", Vol. 31, C.L. Tien, Ed., MIT Press, Cambridge, Mass., 1973, pp. 83-102.
- [44] Kosson, R.L., Quadrini, J.A., Kirckpatrick, J.P., "Development of a Blocking Orifice Thermal Diode Heat Pipe", AIAA Paper 74-754. AIAA/ASME 1974 Thermophysics and Heat Transfer Conference, Boston, Mass., July 15-17, 1974. Also published in "Heat Transfer with Thermal Control Applications", Progress in Astronautics and Aeronautics, Vol. 39, M. Yovanovich, Ed., American Institute of Aeronautics and Astronautics, New York, 1975, pp. 245-258.
- [45] Krolczek, E.J., "Definition of a Cryogenic Heat Pipe Experiment", in "2nd International Heat Pipe Conference 1976", Bologna, Italy, 31st March-2nd April, ESA SP-112 (preprint), Vol. 1, ESTEC, Noordwijk, The Netherlands, pp. 673-682.
- [46] Kunz, H.R., Wyde, S.S., Nashick, G.H., Barnes, J.F., "Vapor Chamber Fin Studies; Operating Characteristics of Fin Models", NASA CR-1139, Aug. 1968.
- [47] Kutateladze, S.S., Borishanskii, V.M., "A Concise Encyclopedia of Heat Transfer", 1st ed., Translated by J.B. Arthur, Pergamon Press, Oxford, 1966, p. 446.
- [48] Langston, L.S., Kunz, H.R., "Liquid Transport Properties of Some Heat Pipe Wicking Materials", ASME Paper 69-HT-17, ASME/ASChE Heat Transfer Conference, Minneapolis, Minn., Aug. 3-6, 1969. Also published in "Heat Pipes", AIAA Selected Reprint Series, Vol. XVI, C.L. Tien, Ed., AIAA, New York, Sept. 1973, pp. 58-67.

- [49] Levy, E.K., "Effects of Friction on the Sonic Velo- city Limits in Sodium Heat Pipes", in "Progress in Astronautics and Aero- nautics", Vol. 29, J.W. Lucas, Ed., MIT Press, Cambridge, Mass., 1972, pp. 383-400.
- [50] Levy, E.K., "Theoretical Investigation of Heat Pipes Operating at Low Vapor Pressures", Journal of Engineering for Industry, Vol. 90, Serie B, No. 4, Nov. 1968, pp. 547-552. Also published in "Heat Pipes", AIAA Selected Reprint Series, Vol. XVI, C.L. Tien, Ed., AIAA, New York, Sept. 1973, pp. 46-51.
- [51] Mathieu, J.P., "Aluminium Extruded Heat Pipe", SABCA Document No. 33. SABCA, Chaussée de Haecht 1470, B-1130, Brussels, Belgium, 15 March 1977.
- [52] Mathieu, J.P., "Caloducs SABCA pour Applications Aero- spatiales", SABCA Document No. 163. SABCA, Chaussée de Haecht 1470, B-1130, Brussels, Belgium, Feb. 1978.
- [53] Mathieu, J.P., "Description of Some European Heat Pipe Developments and Applications", SABCA Document No. 203. SABCA, Chaussée de Haecht 1470, B-1130, Brussels, Belgium, 2 May 1978.
- [54] Mathieu, J.P., "Development of Small Cryogenic Heat Pipes, Phase 3 Report", ESA CR(P)1700. SABCA, Chaussée de Haecht 1470, B-1130, Brussels, Belgium, Sept. 1982.
- [55] Mathieu, J.P., "Follow-on Developments of Small Cryogenic Heat Pipes, Phase 2 Report", ESA CR(P)149702. SABCA, Chaussée de Haecht 1470, B-1130, Brussels, Belgium, Feb. 1981.
- [56] Mathieu, J.P., "Stainless Steel - Ammonia Heat Pipes", SABCA Document No. 39. SABCA, Chaussée de Haecht 1470, B-1130, Brussels, Belgium, 30 March 1977.
- [57] McIntosh, R., Ollendorf, S., Harwell, W., "The International Heat Pipe Experiment", AIAA Paper 75-726. AIAA 10th Thermophysics Conference, Denver, Colorado, May 27-29, 1975.
- [58] McKinney, B.G., "An Experimental and Analytical Study of Water Heat Pipes for Moderate Temperature Ranges", NASA TM X-53849, June 1969.
- [59] Molt, W., "Performance Investigation of Cryogenic Heat Pipes", in "2nd International Heat Pipe Conference 1976", Bologna, Italy, 31st March-2nd April, ESA SP-112 (preprint), Vol. 1, ESTEC, Noordwijk, The Netherlands, pp. 49-62.
- [60] Murakami, M., "Performance Investigation of Superfluid Heat Pipes", AIAA Journal, Vol. 20, No. 4, April 1982, pp. 570-573.
- [61] Murakami, M., Kaido, N., "Study of Superfluid Heat Pipe", AIAA Paper 80-1480. AIAA 15th Thermophysics Conference, Snowmass, Colorado, July 14-16, 1980.
- [62] NASA CR-143797, March 1975.
- [63] Neal, L.G., "Analytical and Experimental Study of Heat Pipes ", Report 99900-6114 ROOO, TRW-Systems Group, Jan. 1967.
- [64] Norris, R.H., Buckland, F.F., Fitzroy, N.D., "Properties of Liquids", in "Heat Transfer Data Book", General Electric Company, Section G514, 1970.
- [65] Ollendorf, S., "Heat Pipes in Space", Astronautics & Aeronautics, Vol. 14, No. 12, Dec. 1976, pp. 64-65.
- [66] Peterson, G.P., Compagna, G.L., "Cryogenic Heat Pipes in Spacecraft Applications",
- [67] Phillips, E.C., Hinderman, J.D., "Determination of Properties of Capillary Media Useful in Heat Pipe Design", ASME Paper 69-HT-18, Aug. 1969.

- [68] Quadrini, J.A., McCreight, C.R., "Development of a Thermal Diode Heat Pipe for Cryogenic Applications", AIAA Paper 77-192. AIAA 15th Aerospace Sciences Meeting, Los Angeles, Calif., Jan. 26-27, 1977.
- [69] Raznjevic, K., "Tables et Diagrammes Thermodynamiques", Editions Eyrolles, Paris, 1970.
- [70] Reid, R.C., Sherwood, T.C., "The Properties of Gases and Liquids. Their Estimation and Correlation", 2nd ed., McGraw-Hill Book Company, Inc., New York, 1966.
- [71] Rotty, R.M., "Introduction to Gas Dynamics", John Wiley & Sons, Inc., New York, 1962, pp. 116-145.
- [72] SABCA, "A95 Qualification Status - Final Presentation", 1987.
- [73] SABCA, "Developmenet of Small Cryogenic Heat Pipes, Phase 3 Report", 1982.
- [74] SABCA, "Follow-on Developments of Small Cryogenic Heat Pipes, Phase 2 Report", 1981.
- [75] SABCA, "High-Performance VCHP Follow-on Development, Final Report", 1981.
- [76] SABCA, "Prequalification of A64 Heat Pipes", 1982.
- [77] SABCA, "Prequalification of A64 Heat Pipes, Final Summary Report", 1982.
- [78] SABCA, "SABCA Grooved CCHP AG135 Standard Qualification - Summary Report", 1983.
- [79] SABCA, "SABCA Heat Pipe Type A 32-24", SABCA, Chaussée de Haecht 1470, B-1130, Brussels, Belgium.
- [80] SABCA, "Transport de Chaleur pour Application Spatiale", 1988.
- [81] Savage, C.J., Wilson, R.J., Aalders, B.G.M., "Development and Test of the ESTEC VCHP Experiment Flown on SPAS-01", 1987.
- [82] Schmidt, E., "Properties of Water and Steam in SI- Units", Springer-Verlag, Berlin, 1969.
- [83] Scollon, T.R., Carpitella, M.J., "Long Life High Reliability Thermal Control Systems Study Data Handbook", NAS 8-26252, General Electric Company, 1970.
- [84] Semena, M.G., Levterov, A.I., "Investigation of the Thermophysical Characteristics of Cryogenic Heat Pipes with a Metal-Fiber Wick", Journal Engineering Physics. Translated from Inzhenerno-Fizicheskii Zhurnal, Vol. 25, No. 1, July 1978, pp. 48-53.
- [85] Shapiro, A.H., "The Dynamics and Thermodynamics of Compressible Fluid Flow", Vol. 2, The Ronald Press Company, New York, 1954, pp. 992-1030.
- [86] Sherman, A., Brennan, P., "Cryogenic and Low Temperature Heat Pipe/Cooler Studies for Spacecraft Application", AIAA Paper 74-753. AIAA/ASME 1974 Thermophysics and Heat Transfer Conference, Boston, Mass., July 15-17, 1974.
- [87] Shlosinger, A.P., Woo, W., Cafaro, C., Bentilla, E.W., "Technology Study of Passive Control of Humidity in Space Suits", NASA CR-690898, 1966.
- [88] Skrabek, E.A., "Heat Pipe Design Handbook", Dynatherm Corporation, Contract No. NAS 9-11927, Aug. 1972.
- [89] Smirnov, G.F., Barsookov, V.V., Mishchenko, L.N., "Engineering Methods of Low-Temperature Heat Pipe Designing Calculations", in "2nd International Heat Pipe Conference 1976", Bologna, Italy, 31st March-2nd April, ESA SP-112 (preprint), Vol. 1, ESTEC, Noordwijk, The Netherlands, pp. 141-151.

- [90] SOLEK, "Solek - The Heat Pipe People", Solek Ltd., 16 Hollybush Lane, Sevenoaks, Kent Sevenoaks (0732) 59957, England.
- [91] Soliman, M.M., Graumann, D.W., Berenson, P.J., "Effective Thermal Conductivity of Dry and Liquid-Saturated Sintered Fiber Metal Wicks", ASME Paper 70-HT/SpT-40, in "Space Systems and Thermal Technology for the 70's", Part II, ASME, 1970.
- [92] Van Oost, S., "Cryogenic Heat Pipe Ageing Phase IV - Final Report", 1990.
- [93] Van Oost, S., "Qualification of A95 Heat Pipe - Final Report", 1988
- [94] Vargaftik, N.B., "Tables on the Thermophysical Proper- ties of Liquids and Gases", 2nd ed., Hemisphere Publishing Corporation, Washington, 1975.
- [95] Weast, R.C., "Handbook of Chemistry and Physics", 57th ed., CRC Press. Inc., Cleveland, 1976, Section E, pp. E-27 to E-46 and Section F, p. F-81.
- [96] Winter, E.R.F., Barsch, W.O., "The Heat Pipe", in "Advances in Heat Transfer", Vol. 7, T.F. Irvine & J.P. Hartnett, Eds., Academic Press, New York, 1971, pp. 219- 320.
- [97] Woo, W., "Study of Passive Temperature and Humidity Control Systems for Advanced Space Suits", NASA CR-73271, Nov. 1968.